

Spring 2018

NOVEL HYBRID PEROVSKITE COMPOSITES AND MICROSTRUCTURES: SYNTHESIS AND CHARACTERIZATION

John P. Murphy
Montana Tech

Follow this and additional works at: https://digitalcommons.mtech.edu/grad_rsch

 Part of the [Materials Science and Engineering Commons](#)

Recommended Citation

Murphy, John P., "NOVEL HYBRID PEROVSKITE COMPOSITES AND MICROSTRUCTURES: SYNTHESIS AND CHARACTERIZATION" (2018). *Graduate Theses & Non-Theses*. 171.
https://digitalcommons.mtech.edu/grad_rsch/171

This Thesis is brought to you for free and open access by the Student Scholarship at Digital Commons @ Montana Tech. It has been accepted for inclusion in Graduate Theses & Non-Theses by an authorized administrator of Digital Commons @ Montana Tech. For more information, please contact sjuskiewicz@mtech.edu.

NOVEL HYBRID PEROVSKITE COMPOSITES AND
MICROSTRUCTURES: SYNTHESIS AND CHARACTERIZATION

by
John Patrick Murphy

A dissertation submitted in partial fulfillment of the
requirements for the degree of

Doctor of Philosophy:
Materials Science

Montana Tech
2018



Novel Hybrid Perovskite Composites and Microstructures: Synthesis and Characterization

By

John Patrick Murphy

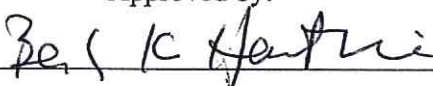
B.S. Applied Physics, Lock Haven University, Lock Haven, Pennsylvania, 2014
A.A.S. Nanotechnology, Lock Haven University, Lock Haven, Pennsylvania, 2014

Dissertation
presented in partial fulfillment of the requirements for the degree of:

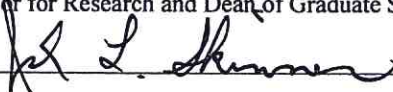
Doctor of Philosophy
in Materials Science

Montana Tech
Butte, MT
May 2018

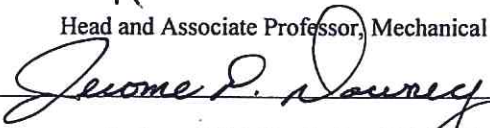
Approved by:



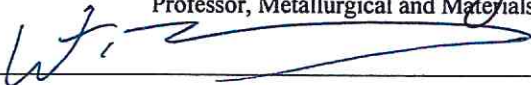
Beverly K. Hartline, Dean
Vice Chancellor for Research and Dean of Graduate Studies, Montana Tech Graduate School



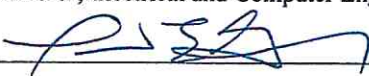
Jack L. Skinner, Chair
Head and Associate Professor, Mechanical Engineering Department, Montana Tech



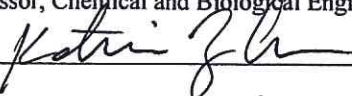
Jerome P. Downey, Co-Chair
Professor, Metallurgical and Materials Engineering Department, Montana Tech



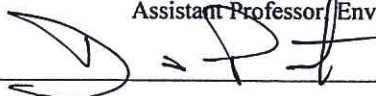
Wataru Nakagawa
Associate Professor, Electrical and Computer Engineering Department, Montana State University



Paul Gannon
Associate Professor, Chemical and Biological Engineering Department, Montana State University



Katherine R. Zodrow
Assistant Professor, Environmental Engineering Department, Montana Tech



Dario Preito
Assistant Professor, Mechanical Engineering Department, Montana Tech

© COPYRIGHT

by

John Patrick Murphy

2018

All Rights Reserved

Murphy, John, PhD Materials Science, May 5, 2018

Novel Hybrid Perovskite Composites and Microstructures: Synthesis and Characterization

Chairperson: Jack L. Skinner

The water-energy nexus has been described as one of the great problems of our time. In an ever-growing society the demand for resources such as water and electricity often dictate the magnitude and direction of growth of society. Efficient generation of electricity, with minimal socioeconomic pushback, is paramount in the stable growth of our society. Solar energy harvesting is a strong candidate for the efficient generation of electrical energy with increasingly minimal resource use in fabrication. As manufacturing processes improve and novel materials are discovered/optimized, solar energy harvesting becomes a more economically viable means of energy generation. Hybrid perovskites (HPs) represent the next-generation of solar energy harvesting materials due to favorable optoelectronic properties. Since first used as an absorber layer in a solar cell in 2012, HPs have experienced a ~10% increase in efficiency to 22.7%, and continue to climb. Despite the rapid climb in efficiencies, HPs solar cells have not been utilized the solar energy market due to intrinsic instabilities of the HP material itself. In order to implement the potentially disruptive HP technology, degradation triggered via environmental factors must be addressed.

In an effort to mitigate the degradation initiated by environmental factors, in particular moisture, novel HP composites and microstructures were created. HP composites were created both through melt and solution compounding methods. Melt compounding methods demonstrated the feasibility of the synthesis of the HP materials *in situ* in the polymer melt. Additionally, the moisture resilience of the material was demonstrated through an accelerated ageing study. The polymer melt compounding method was then utilized to produce a polymer melt feedstock for melt electrospinning and ultimate creation of HP composite microfibers. Solution compounding methods were then implemented to generate HP/polymer composites with regular dispersion and isotropic optoelectronic behavior.

Keywords: Hybrid perovskites, Microcomposites, Electrospinning, Percolation

Dedication

For my Family

Preface

Hybrid perovskites (HPs) are a new and exciting opto-electronic material with a great deal of promise for use in light collection/generation applications, if the moisture-driven degradation of the HP material can be addressed. The work outlined herein is the culmination of four years of research directed at the creation of HP composites and microstructures that are functional and moisture stable. Initial work was directed at the creation of a HP/polystyrene composite from polymer melt compounding. The result of the work was a composite that demonstrated optical absorption properties of HPs with improved moisture stability affected by the polystyrene and resulted in a publication and conference presentation, Organometallic Halide Perovskite Synthesis in Polymer Melt for Improved Stability in High Humidity. *MRS Advances*, 1(47), 3207-3213. Research into the creation of HP composites using melt compounding to simultaneously synthesize and mix the HP into a polymer matrix had not yet been attempted. A fabrication technique utilizing the polymer melt was then demonstrated in the form of a melt electrospinning process to create HP composite microfibers. Due to the novelty of the fabrication process a patent was submitted, (US Pending Patent 15/610,014), “*Method for the Synthesis of Hybrid Organic-Inorganic Perovskites via Melt Electrospinning*,” prior to the presentation and publication of work on the composite fibers, Hybrid Organic-Inorganic Perovskite Composite Fibers Produced via Melt Electrospinning. *J. Vac. Sci. Tech. B*, 34, 06KM01. After the demonstration of success of the melt compounding method in the creation of moisture resistant composites, the electrical behavior of the composite material was investigated to determine the necessary amount of HP material needed in the composite to elicit electrical conduction via percolation through the composite material. The results of the assessment of the percolation threshold were presented and published, Loading Dependent Electrical Properties of Hybrid Perovskite Composite Media. *MRS Advances*, 2(53),

3069-3076. Work is continuing along the direction of reducing the necessary amount of HP material needed to elicit an electrical response from the composite by incorporation of secondary dopants into the composite media, such as graphene. A lateral attempt was also made to fabricate a functional HP fiber through coaxial electrospinning. As opposed to randomly dispersed HP microcrystals in a composite material, a coaxial fiber would have a continuous HP core through a polymer shell. Electrospun fibers produced in the coaxial research demonstrated remarkable moisture resilience and could tolerate complete immersion in water. The coaxial fiber work was also resulted in a presentation and a publication, Coaxial Hybrid Perovskite Fibers: Synthesis and Encapsulation in Situ via Electrospinning. *J. Vac. Sci. Tech. B*, 35, 06G402 The results of the aforementioned work represent some of the earliest work done in the creation of HP/polymer composites and their optical and electrical characterization. Work on the creation of functional HP composites is fundamental in the production of next-generation, low-cost opto-electronic devices.

Acknowledgements

First, I would like to thank my family for their support through the course of my education, which has been quite a long journey. I would like to thank my advisor, mentor, and friend, Dr. Jack L. Skinner whose tutelage has helped to inform the research herein and guide my development as a researcher over the last four years. His guidance both in and out of the laboratory has been invaluable and greatly appreciated. I would also like to thank Professor Jerome Downey, Professor Wataru Nakagawa, Professor Paul Gannon, Professor Katherine Zodrow, and Professor Dario Prieto for serving on my dissertation committee and reviewing the dissertation presented herein.

I would also like to thank the members of the Montana Tech Nanotechnology Laboratory. I've had the distinct pleasure of working with some remarkable people over the last four years, and it's been my privilege to also call them friends. I would like to especially thank: Brandon Ross for his help in melt electrospinning the composite fibers; Dr. Jessica Andriolo for her help in planning a great deal of the HP work during an extensive grant writing process; Nathan Sutton for his help in coaxial electrospinning and discussing the nature of coaxial fiber systems; Molly Brockway for her ongoing help in transitioning some of the work outlined herein into a functional device.

Thanks are also due to Gary Wyss and Ronda Coguill of the Center for Advanced Mineral, Metallurgical, and Materials Processing for their help in the characterization of the materials synthesized throughout the course of this research.

Lastly, I would like to again thank my family and friends for whom I cannot express my gratitude enough for their support and guidance.

Table of Contents

DEDICATION	V
ACKNOWLEDGEMENTS	VIII
LIST OF TABLES	XI
LIST OF FIGURES.....	XII
LIST OF EQUATIONS	XXII
GLOSSARY OF TERMS.....	XXIII
1. INTRODUCTION	1
1.1. <i>Motivation</i>	1
1.2. <i>Research Objectives</i>	2
2. BACKGROUND.....	3
2.1. <i>Photoactive Materials</i>	3
2.1.1. Band Structure and Charge Carrier Generation	3
2.2. <i>HPs</i>	5
2.2.1. Structure.....	5
2.2.2. Utilization in Photovoltaics.....	6
2.2.3. Optoelectronic Properties	6
2.2.3.1. Optical Absorbance	6
2.2.3.2. Charge Carrier Dynamics.....	8
2.2.3.3. Tuning the Band Gap.....	9
2.2.3.4. Issues with HP Materials	11
2.3. <i>Electrospinning</i>	14
2.4. <i>Polymer Composites</i>	15
2.4.1.1. Percolation Theory.....	16
3. CREATION AND CHARACTERIZATION OF HP-POLYMER COMPOSITES.....	22

3.1.	<i>Polymer Melt Compounding</i>	22
3.1.1.	Accelerated Ageing Study	35
3.2.	<i>Solution Compounding</i>	48
3.2.1.	HP Filler Phase Generation	49
3.2.1.1.	Sonochemical Synthesis	49
3.2.1.2.	Inverse Temperature Crystallization	56
3.2.1.3.	Sonochemical vs. ITC for Filler Phase Generation	59
3.2.1.4.	Solvent/Anti-Solvent Reprecipitation of PbI_2	61
3.2.1.5.	Ligand-assisted Solvent/Anti-solvent Reprecipitation of PbI_2	63
3.2.2.	Composite Generation	65
3.2.3.	Composite Characterization	67
3.2.3.1.	Determining the Percolation Threshold for Electrical Conduction	71
4.	ELECTROSPINNING HP-POLYMER MICRO/NANO FIBERS	76
4.1.	<i>Melt Electrospinning Composite Fibers</i>	76
4.2.	<i>Coaxial Electrospinning Encapsulated HP</i>	87
5.	CONCLUSIONS	96
5.1.	<i>Melt Compounding</i>	96
5.2.	<i>Solution Compounding</i>	97
5.3.	<i>Melt Electrospinning</i>	97
5.4.	<i>Coaxial Solution Electrospinning</i>	97
5.5.	<i>Recommendations for Future Work</i>	98
6.	REFERENCES	101

List of Tables

Table I. Electron and hole mobility for photoactive semiconductors9

Table II. Intrinsic band gap values for commonly used semiconductors and HPs10

List of Figures

- Figure 1. Wannier-Mott and Frenkel excitons overlaid on lattice structures typical of the materials in which they are commonly found. Adapted from [5].....4
- Figure 2. General perovskite crystal structure of chemical make-up ABX_3 where the red circles are the A-sites, the green circle is the B-site, and the blue circles are the X-sites. In HPs the lead halide octahedra are stabilized by the organic cation at the A-site.5
- Figure 3 Optical absorbance as a function of wavelength for methylammonium lead iodide perovskite and other commonly used photovoltaic semiconductor materials, adapted from [15].....8
- Figure 4. Band gap of $CH_3NH_3Pb(I_{1-x}Br_x)_3$ HP as a function of the ratio of halides. Adapted from [23].....11
- Figure 5. Disorder in the HP crystalline lattice increases as the material is increasingly hydrated. Adapted from [40].....12
- Figure 6. Typical electrospinning apparatus [48].14
- Figure 7. Diagram of a typical composite with a continuous matrix phase and a dispersed filler phase.15
- Figure 8. A schematic of a composite material below and above the critical loading to achieve percolation. A continuous network across the composite allows electrical flow. Adapted from [52]17
- Figure 9. A percolation threshold plot. The characteristic S-curve of the percolation threshold follows a power law expression. [53].18

- Figure 10. A schematic of the setup used for producing HP-polystyrene composites through melt compounding.....23
- Figure 11. A polypropylene melt with HP precursor mixed in simultaneously. The simultaneous mixing resulted in the agglomeration of HP crystallites through the polymer melt.24
- Figure 12. Electron micrograph of HP crystallites embedded in a polypropylene matrix. The bright grey spot on the upper right has a Pb:I ratio of (1:2.25) and the crystallite on the bottom left has a ratio of (1: 4.79).25
- Figure 13. Molding apparatus used to create circular disk of composite media. Polypropylene base material can be seen melting in the mold.26
- Figure 14. Polystyrene melt blended with PbI_2 . The mixture pictured has not yet reached a state of homogeneity desired prior to mixed in the $\text{CH}_3\text{NH}_3\text{I}$ precursor to initiate the HP reaction.....27
- Figure 15. HP/polystyrene composite sample after molding and release. Unreacted PbI_2 throughout the sample was a consistent issue in the initial studies.28
- Figure 16. Cross-sectional electron micrograph of the HP composite circular sample taken shortly after casting.....29
- Figure 17. Energy-dispersive spectroscopy of crystallites present in the HP-polystyrene composite seen in Figure 14. The $\text{CH}_3\text{NH}_3\text{PbI}_3$ perovskite can be seen on the left as evidenced by the ratio of the atomic percent of Pb:I. However, crystallites of unreacted PbI_2 remain in the composite as well seen on the right, and also evidenced by the ratio of the atomic percent of Pb:I.30
- Figure 18. UV-Vis absorption spectrum for PbI_2 in polystyrene. (Inset) Optical micrograph of PbI_2 crystallites embedded in a polystyrene matrix.....32

- Figure 19. UV-Vis absorption spectrum for $\text{CH}_3\text{NH}_3\text{PbI}_3$ HP thin film dropcast onto a glass slide. (Inset) Optical micrograph of $\text{CH}_3\text{NH}_3\text{PbI}_3$ crystallites embedded in a polystyrene matrix.33
- Figure 20. The effect of methylamine gas on the physical state of $\text{CH}_3\text{NH}_3\text{PbI}_3$ HP. Adapted from [58].34
- Figure 21. Electron micrographs of crystallites present in the composite media. EDS analysis determined the bright material in both micrographs was HP material. The amorphous-like morphology of the material appears to have formed as a result of the HP material being in a liquid state.34
- Figure 22. Custom humidity ageing chamber which enabled the rapid ageing of HP composites in high humidity conditions. Humidity and temperature monitored continuously using an Omega RH-USB sensor. (RH 90.3% + 4.9% at 20.24 °C + 1.26 °C)37
- Figure 23. Humidity and temperature conditions in the humidity chamber over the course of the study. The large and rapid drops in the humidity correspond with the chamber being opened to extract samples for characterization, subsequent increases and decreases in temperature are likely the result of added heat by the experimenter and evaporative cooling to reconstitute the humidity.38
- Figure 24. Schematic of the far-field probing station configuration used in the investigation of the composite samples during the accelerated ageing.39
- Figure 25. Theoretical absorbance values for polystyrene and $\text{CH}_3\text{NH}_3\text{PbI}_3$ HP. The data shows that while polystyrene is highly transparent through the visible spectrum the case is not the same for the HP which begins to absorb strongly near 760 nm and increases logarithmically into the UV.40

- Figure 26. Light rays incident on the composite from various trajectories, the simplified drawing does not show the effect of the higher refractive index of the composite media...41
- Figure 27. Samples used in the accelerated ageing study. Datum marks can be seen on both samples and were used as locations to collect consistent UV-Vis spectra.43
- Figure 28. UV-Vis spectra of HP-polystyrene composite material compared to a neat HP film on glass. The optical absorption onset can be seen at 760 nm for both the composite and the glass slide. Additionally, the PbI_2 can be seen at 530 nm in the composite spectra.44
- Figure 29. Optical micrographs the same field of view of a HP film deposited on a glass slide. Immediately after deposition (left) and after 24 hours in the humidity chamber (right). The change in the film morphology is apparent from a polycrystalline HP film to a needle-like PbI_2 film.45
- Figure 30. Optical micrograph of HP composite, after molding (left) and on the last day of the study (right). White crystalline material has infiltrated the scores in the sample surface used as datum to track location.46
- Figure 31. Optical micrograph of the surface of the composite after the completion of the accelerated ageing study. The white $\text{CH}_3\text{NH}_3\text{I}$ spots are located over degrading HP crystallites, additionally a large unreacted PbI_2 crystallite can be seen in the bulk of the composite. A large amount of small black crystallites seen above the PbI_2 crystallite strongly indicated that most degradation occurred at the surface of the samples..47
- Figure 32. Optical micrograph of HP microcrystallites synthesized via sonochemical methods.50

- Figure 33. UV-Vis spectrum of the powder seen in Figure 30. The sharp absorption onset near 760 nm strongly indicates that $\text{CH}_3\text{NH}_3\text{PbI}_3$ is present. The increase in absorption near 530 nm also indicates the presence of some PbI_251
- Figure 34. Electron micrograph of the HP powder seen in Figure 30. The tetragonal shape of the crystallites throughout the micrograph are indicative of the tetragonal phase of $\text{CH}_3\text{NH}_3\text{PbI}_3$52
- Figure 35. Schematic showing the growth of the HP phase on the surface of the PbI_2 crystallites while the core of the crystallites remains unchanged.53
- Figure 36. Electron micrograph of a cross section of the HP composite made using sonochemically synthesized HP crystallites. The red crosses indicate areas where EDS analysis was performed. Inset EDS data from the higher red cross.54
- Figure 37. Electron micrographs of sonochemically synthesized HP crystallites. The effect of increased sonication time can be seen in the difference in morphologies from the 5 min sonication time (left) to the 20 min sonication time (right). The larger needle-like crystals are PbI_2 which takes on needle-like habits in IPA due to slow Ostwald ripening effect.55
- Figure 38. Solubility vs. Temperature plot for the $\text{CH}_3\text{NH}_3\text{PbI}_3$ HP (denoted here as MAPbI_3). It can be seen that the 1M solution has a maximum solubility at 60 °C with steep decreases in solubility on either side of the maxima.56
- Figure 39. Inverse temperature crystallization process, from filtering (A) to the mineral oil bath at 110 °C57

- Figure 40. Average quantity of $\text{CH}_3\text{NH}_3\text{PbI}_3$ single crystals produced from a 10 mL batch of solvent (A). The mechanical milling via mortar and pestle of the single crystals into a powder for further processing (B & C).....58
- Figure 41. Electron micrographs of ITC HP after pulverization and sonication for 20 minutes. The smaller particulates are likely the result of cavitation-driven small mass liberation from the ITC microcrystallites.....59
- Figure 42. Electron micrographs of ITC grown (left) and sonochemically synthesized (right) HP crystallites. The ITC crystallites, while chemically pure, demonstrate a great deal of variation in morphology, whereas the sonochemical crystallites demonstrate fairly uniform size distribution but lack chemical purity.60
- Figure 43. Electron micrograph of PbI_2 crystals produced from the initial solvent/anti-solvent reprecipitation technique. Needle-like crystal habits are observed in the PbI_2 crystals grown here.62
- Figure 44. Electropotential maps of DMF (left) and PbI_6^{4-} produced in Spartan Chemistry [82].62
- Figure 45. Electron micrographs of the terminal end of the PbI_2 crystal growth in solvent/anti-solvent reprecipitation. The exterior of the PbI_2 acicular crystals grow first, followed by the center. Crystal growth occurs rapidly, but was not completed in these micrographs.63
- Figure 46. Electron micrograph of PbI_2 precipitants formed after the addition of octylamine to the DMF/ PbI_2 solution prior to reprecipitation.64
- Figure 47. Electron micrographs of the HP crystalline filler phase material synthesized using the ligand-assisted solvent/anti-solvent reprecipitation method. Particle size has been

- considerably reduced and the size and shape of particles are fairly uniform throughout the large batch synthesis66
- Figure 48. Typical dropcast HP/polystyrene composite samples of various loadings (60-67
- Figure 49. UV-Vis spectra of the initial sonochemically synthesized HP filler phase (Untreated HP), HP filler sonochemically synthesized from octylamine treated PbI_2 precursor (Pretreated HP) and a composite created from the pretreated HP filler phase material (75 wt% Composite). The spectrum of the composite matches the characteristic shape of the pretreated material and lacks the increase in the 530 nm range indicating very little PbI_2 is present.68
- Figure 50. X-Ray diffractogram of a HP composite sample (Bulk_synth_comp) as compared to that of a chemically pure ITC grown single crystal. The broadening and magnitude reduction are a consequence of the small particle size and dispersion [88] and right-shifted peaks are typical of composite materials.69
- Figure 51. Electron micrograph cross-section of a 75 wt% HP composite sample. Cubic HP crystallites are visible throughout the composite sample, demonstrating a high degree of dispersion in the dropcast composite sample.....70
- Figure 52. Optical micrographs of the interaction between a droplet of 30 wt% polystyrene in toluene and a film of HP powder (left) and a HP single crystal (right). The average contact angle of droplets with the powder film was 60° indicating a relatively low interfacial energy between the HP and the polymeric solution.71
- Figure 53. Schematic of the testing configuration for the composite disks. A two-wire configuration was used as the contact resistance was negligible given the high resistance of the composite.....72

- Figure 54. Averaged IV sweeps for weight loadings up to 75wt% HP in polystyrene. Weight loadings lower than 75wt% demonstrated a capacitive behavior, ohmic behavior was not observed until the loading of the composites had reached 75wt%.74
- Figure 55. Plot of conductivity vs. weight % loading to illustrate the percolation threshold was reached at 75 wt% the rapid increase in the conduction of the composite is typical of reaching the percolation threshold in composite materials.75
- Figure 56. Schematic of the custom melt electrospinner used for the creation of HP/PS composite microfibers.77
- Figure 57. HP precursors (top), polystyrene feedstock (bottom left) and the simple mixture of all three into the melt electrospinning feedstock material.78
- Figure 58. Thermogravimetric analysis of the components of the melt electrospinning feedstock. The methylammonium iodide components begins to undergo mass loss at the lowest temperature of the three components at approximately 230 °C.....79
- Figure 59. Optical micrograph of microfibers produced during the melt electrospinning process. Fibers are uniform in diameter with minimal breaks or beading.....80
- Figure 60. Electron micrographs of melt electrospun fibers with accompanying elemental analysis data. The methylammonium iodide (left) fibers demonstrated irregular morphologies and the precursor phase separated from the polystyrene. The PbI_2 embedded in the fibers (center), and typically produced larger fibers with somewhat regular morphology. The HP material found in the fibers (right) demonstrated circular/spherical morphologies and were typically found in smaller diameter fibers.81

- Figure 61. X-ray diffractograms of the three components of the melt electrospinning feedstock (PS, MAI, PbI_2) and the melt electrospun fiber sample (PS-OHP). Peaks in the composite fibers demonstrate that HP material was successfully synthesized.82
- Figure 62. PbI_2 embedded in a melt electrospun polystyrene fiber. The crystallite has a localized effect on the fiber diameter, but was not large enough to interrupt the melt electrospinning process.83
- Figure 63. Spherical HP particles observed throughout electrospun fibers. The spherical shape is explained by the liquid HP material being emitted from the spinneret and solidifying in situ.84
- Figure 64. Electron micrograph of the solids from melt electrospun HP/polystyrene composite fibers. Arrows indicate locations of spherical HP particles.85
- Figure 65. Electron micrographs (secondary electron on left, backscatter electron on right) show the spherical particles are composed of the same material as the other solids as verified by the elemental contrast which shows the spheres and other solids are higher Z-value elements than the aluminum substrate in the background.86
- Figure 66. An electrospun fiber mat immediately after electrospinning (left) and after 5 min in ambient condition (right). The color change of the fiber mat is indicative of the HP reaction occurring as residual solvent evaporates in the fibers.88
- Figure 67. UV-Vis spectrum of the electrospun fiber mat seen in Figure 66. The optical absorption onset of the $\text{CH}_3\text{NH}_3\text{PbI}_3$ is visible at 760 nm as expected, with very little inflection at 530 nm indicating little to no PbI_2 is present.89
- Figure 68. X-Ray diffractograms of the coaxial electrospun fibers compared to an ITC grown single crystal and the HP precursors.90

- Figure 69. Optical micrograph (left) and fluorescent optical micrograph (right) of coaxial electrospun fibers with $\text{CH}_3\text{NH}_3\text{PbBr}_3$ HP material in the core of PS sheaths. The fluorescent image shows that there are some fibers with continuous cores, but most fibers demonstrate a discontinuous core as seen in most of the fibers in the fluorescent micrograph.91
- Figure 70. Electron micrographs of fiber cross-sections. Coaxial fibers demonstrated a cardioid morphology, likely the result of the shell solution evaporating at a slightly higher rate resulting in semi-solidification and collapse of the shell structure into the still liquid core.....92
- Figure 71. Optical and fluorescence micrographs of the coaxial fibers, immediately after electrospinning (top), after a 30 minute anneal at $80\text{ }^\circ\text{C}$ (middle), and after 30 minutes of complete immersion in water (bottom). Visually no decrease in the photoluminescence was observed in any of the fiber mats.....93
- Figure 72. Optical micrographs of water droplets resting on the surface of fiber mats of neat polystyrene (top) and the coaxial fiber mats (bottom). Electron micrographs of the fiber mats show very little difference in the morphology other than fiber diameter.....94

List of Equations

Equation 1. Absorbance of a material [11]	6
Equation 2 Complete degradation of methylammonium lead iodide perovskite dihydrate via exposure to liquid water [40].	12
Equation 3. Degradation of methylammonium iodide into methylamine gas and hydrogen iodide gas	13
Equation 5. Thermal decomposition reaction for methylammonium iodide into methylamine gas and hydrogen iodide gas.	35
Equation 6. Lambertian scattering equation, describing the light scattered off an ideal, flat surface.	41
Equation 7. Resistivity is calculated from the area (A) and thickness (t) measured from the composite samples and the resistance (R) determined from the IV sweeps.	73

Glossary of Terms

Term	Definition
PCE	Power Conversion Efficiency
HP	HP
EHP	Electron Hole Pair
DSSC	Dye-Sensitized Solar Cell
LED	Light Emitting Diode
UV	Ultra-Violet
HTL	Hole Transport Layer
ETL	Electron Transport Layer
SEM	Scanning Electron Microscopy
EDS	Energy Dispersive Spectroscopy
ITC	Inverse Temperature Crystallization
GBL	γ -Butyrolactone
DMF	N,N-Dimethylformamide
IPA	Isopropyl Alcohol
IV	Current-Voltage
ES	Electrospinning
TGA	Thermogravimetric Analysis
XRD	X-Ray Diffractography

1. Introduction

1.1. Motivation

The ability of our society to progress is predicated by our ability to innovate technologically. A fundamental pillar of progress is the need to generate energy on larger scales, lower costs, and with a minimized environmental impact. One potential solution to meet the growing energy demand of the future is photovoltaics, which utilize abundant solar radiation to convert light energy to electrical energy, with minimal environmental impact. In order to make photovoltaics a compelling solution to the energy demands of the future the power-conversion efficiency (PCE) of solar cells must continue to improve [1], and the cost of production must continue to decrease across all areas [2]. The trend in higher PCE and lower costs is seen in the, “third generation”, of solar cells which utilize new materials, novel fabrication techniques, and unique nanostructures to achieve greater efficiencies and economies. A new class of materials at the forefront of the third generation of solar cell technology are hybrid perovskites (HPs). A rapid ascent in PCEs from 3.8% when first implemented in 2009 [3] to 22.7% in 2017 [1] has garnered a great deal of interest in the increasingly more versatile HP solar cell.

One of the inherent problems of HP solar cells is in the HP material itself, which is chemically unstable and easily-susceptible to degradation on-set by environmental factors such as humidity, ultra-violet light, and excess heat. The unstable nature of the HP material has led to investigations into methods to mitigate or halt degradation of the HP material all-together. Approaches at staving off degradation often involve either the tailoring of HP chemistry or through modification of the physical environment of the HP itself. Both approaches seek to prevent degradation while also maintaining the unique optoelectronic properties of HPs and the relatively low cost of production involved in fabrication of HP-based devices.

The creation of micro/nanostructured HP/polymer media provides protection to the sensitive HP material by lending the robust mechanical and hydrophobic properties of polymeric materials to the low-cost and optoelectronically advantageous HP material. Creation of HP-based composites and encapsulated micro/nanostructures is a relatively unexplored area of research owing to the relatively short-time that HP materials have been studied for photovoltaic applications. The favorable combination of HPs and polymers will not only enable the use of the new materials in solar cells but will also enable the creation of novel sensors and smart materials.

1.2. Research Objectives

The goal of this research was to develop new synthesis protocols for HPs that effectively protect the sensitive material from environmental factors. These new protocols involved the creation of a HP/polystyrene (HP/PS) composite media using solution/melt-compounding techniques and the fabrication of optically active microfibers utilizing melt and solution electrospinning (ES) techniques. Resultant composite media and microfibers were then characterized to elucidate morphological and optoelectronic properties. Finally, the optimized material was integrated into a device and characterized.

2. Background

2.1. Photoactive Materials

2.1.1. Band Structure and Charge Carrier Generation

Photoactive materials are capable of transduction of light into electrical energy through use of their electron energy levels. In crystalline materials, electron energy levels combined over a long-range of repeating crystalline unit cells build up discrete energy bands. The filling and overlap of the electron energy states determines whether a crystalline material is an insulator, semiconductor, semimetal or metal [4]. Semiconductor materials are of particular interest in optoelectronics due to the ability to modulate optical and electrical properties through material processing techniques. Semiconductor crystalline materials are capable of absorbing light due to separations in their respective discrete electron energy states known as “band-gaps”. An incoming photon can be absorbed to promote electrons from the lower discrete electron band or valence band to a higher energy state in the conduction band. The promotion of an electron also leaves a vacancy in the valence band known as a hole, this combination of two bound-particles is known as an electron-hole pairs (EHPs) or excitons. The energy binding the EHP dictates the behavior of charge carriers in a crystalline material and are often grouped into two categories, Frenkel excitons and Wannier-Mott excitons, seen in Figure 1.

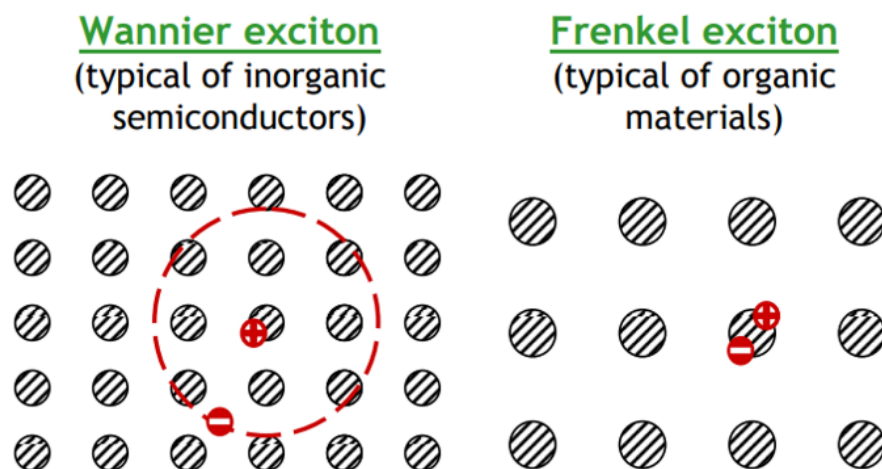


Figure 1. Wannier-Mott and Frenkel excitons overlaid on lattice structures typical of the materials in which they are commonly found. Wannier excitons typically demonstrate a much larger distance between the positively and negatively charged particle, whereas Frenkel excitons demonstrate a higher energy and small radius exciton. Adapted from [5].

Frenkel excitons are observed in organic semiconductor materials and are known as small-radius exciton, whereas Wannier-Mott excitons are known as large-radius excitons and are typically observed in inorganic semiconductors. The radius of these excitons can be seen in Figure 1, the large radius excitons.

The exciton binding energy, or the energy that binds an electron to its hole counterpart, dictates the nature of charge generation in photoactive materials and devices. In the case where the exciton binding energy is high, seen in organic semiconductors and quantum dots, the exciton must diffuse through the photoactive material [6] to an interface where excitons can dissociate and electrons can be successfully extracted from the material. The diffusion length before exciton recombination becomes an issue when considering the design of opto-electronic devices, particularly in the maximum thickness of the photon-absorbing layer. In the case where the exciton binding energy is low, seen in most inorganics semiconductors, the exciton can

dissociate spontaneously given that the available free energy is greater than the exciton binding energy; at room temperature the free energy term is near 25 meV.

2.2. Hybrid Perovskites

2.2.1. Structure

Before it was used to describe a typical crystal structure the word perovskite was specific to a mineral, calcium titanate (CaTiO_3), first discovered in the Ural mountains of Russia in 1839. Currently, the term perovskite describes a crystal structure with the form ABX_3 , seen in Figure 2 below. Typical A and B sites in the crystal structure are smaller metal cations that are charge balanced with the X site anions. It was not until 1892 that cesium lead halide perovskites (CsPbX_3) were discovered [7] and not until 1978 that hybrid organic-inorganic methylammonium lead halide perovskites ($\text{CH}_3\text{NH}_3\text{PbX}_3$) were first synthesized [8].

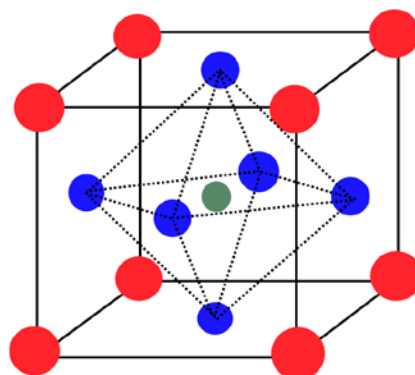


Figure 2. General perovskite crystal structure of chemical make-up ABX_3 where the red circles are the A-sites, the green circle is the B-site, and the blue circles are the X-sites. In HPs the lead halide octahedra are stabilized by the organic cation at the A-site.

2.2.2. Utilization in Photovoltaics

HPs first saw utilization in photovoltaics as a sensitizer in dye-sensitized solar cells (DSSC) in 2009 [3] by Miyaska *et al.* In the DSSC the HPs were present in the form of nanoparticles. These initial DSSC designs yielded PCEs of 3.1% for the bromide HP and 3.8% for the iodide HP; however, the device lifetime was an issue as the electrolyte solution in the DSSC degraded the HP materials.

Three years after the initial use as a sensitizing material in DSSC designs a solid-state solar cell utilizing HP as the photon absorbing material was investigated and demonstrated a PCE of 9% [9]. At nearly the same time Snaith *et al.* were building a similar solid-state cell [10] with one principal difference: they didn't utilize a nanoporous n-type conducting oxide (TiO₂) for photoelectron injection. Instead, a mesoporous non-conducting oxide (Al₂O₃) was used as a scaffolding, and EHPs are conducted to an interface for extraction and demonstrated PCEs of 10.9%. Since 2012 the PCEs of HP based solar cells has been steadily climbing to the current value of 22.7% [1].

2.2.3. Optoelectronic Properties

2.2.3.1. Optical Absorbance

The optical absorbance of the photoactive layer along with the charge carrier diffusion length dictate the boundary conditions for the thickness of the layer in a device stack.

Absorbance of a material is a function of the imaginary component of its dielectric constant described by equation 1.

$$\alpha = \frac{4\pi k}{\lambda} = \frac{2\pi \epsilon_2}{\lambda n}$$

Equation 1. Absorbance of a material [11].

where α is the absorbance of the material, k is the extinction coefficient, λ is the wavelength of light passing through the material, and ϵ_2 is the imaginary component of the dielectric constant. Absorbance values are typically reported for the characteristic penetration depth; the depth into the material at which point 37% of the total incident light has been absorbed. Higher values of absorbance allow much thinner layers to be utilized for photon capture and conversion.

The optical absorbance in HPs is comparable to that of the widely used III-V semiconductors [12], [13]. A direct comparison was done by Ziang *et al.* seen in Figure 3. Currently, the record efficiency of a single junction solar cell is held by a GaAs cell with a PCE of 28.8% [1]. GaAs cells are able to utilize a greater deal of the NIR spectrum, as seen in Figure 3; however, the characteristic shape of the absorbance spectra clearly matches that of $\text{CH}_3\text{NH}_3\text{PbI}_3$ HP material, albeit slightly red-shifted. The decreased performance of the HP in this case is more than made for in the cost of producing GaAs solar cells, as compared to cost associated with manufacturing HP cells [14].

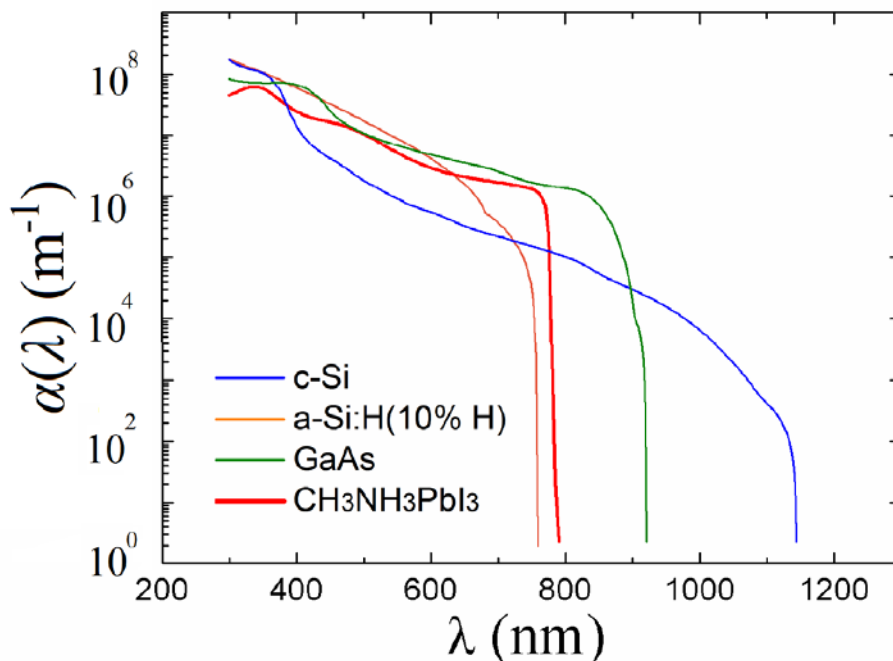


Figure 3 Optical absorbance as a function of wavelength for methylammonium lead iodide perovskite and other commonly used photovoltaic semiconductor materials. The optical absorbance of HPs is on par with the absorbance of Si and GaAs semiconductors typically used in solar cells. Adapted from [15].

When comparing HP solar cells to the silicon based cells (c-Si, crystalline silicon and a-Si, amorphous silicon), it can be seen that the HP material already outperforms both the c-Si and a-Si in terms of its absorbance. The improved performance is also reflected in the PCEs of the cells with a-Si, c-Si, and HP having values of 14.0%, 25.8%, 22.7%, respectively [1].

2.2.3.2. Charge Carrier Dynamics

HPs have unique charge carrier dynamics due to their hybrid nature. In typical inorganic semiconductors charge carriers behave as free, weakly bound, charges moving through the crystalline lattice of the material [16]. Both holes and electrons have independent values describing their ability to move through the crystalline lattice known as mobility. See Table 1 for examples of electron/hole mobility. In photoactive devices the mobilities of holes and electrons

are related to the thickness of respectively charge transport layers, which typically share an interface with the photoactive layer in device stacks.

Table I. Electron and hole mobility for photoactive semiconductors

Material	Electron Mobility (cm²/V-s)	Hole Mobility (cm²/V-s)
Si [4]	1350	480
Ge [4]	3600	1800
GaAs [4]	8000	300
CH ₃ NH ₃ PbI ₃ [17]	24.8	164

The electron and hole mobility of HP as seen in Table II are relatively low when compared to the mobilities of other common photoactive semiconductors. However, again as in the case with the optical absorbance, the low cost associated with the fabrication of HP materials [14] allows the diminished performance to be made up in cost of production.

A fundamental issue in the consideration for the design of any photoactive device is the length over which a charge carrier can diffuse prior to recombination and the relative density of trap-states in the materials that capture charge carriers and prohibit extraction. HPs have charge carrier diffusion lengths on the order of 1-10 μm under normal solar irradiation [18], and combined with high absorbance in the visible spectrum, allow for optically thick ($\sim 100\text{ nm}$) films of HP materials to be utilized in solar cells enabling the rapid climb in PCEs seen in HP based solar cells.

2.2.3.3. Tuning the Band Gap

The band gap of a photoactive material dictates the operational wavelength range of devices fabricated from aforementioned materials; band gaps of common semiconductors can be seen in Table II. In the case of photovoltaics, the band gap is directly related to the theoretical

Table II. Intrinsic band gap values for commonly used semiconductors and HPs

Material	Band Gap at 300 K (eV)
Si [4]	1.11
Ge [4]	0.66
GaAs [4]	1.43
InP [4]	1.27
CH ₃ NH ₃ PbI ₃ [19]	1.55
CH ₃ NH ₃ PbBr ₃ [19]	2.3
CH ₃ NH ₃ SnI ₃ [19]	1.1

maximum efficiency of the cell through the ‘Shockley-Queisser limit’ [20], which predicts that the maximum efficiency for a single p-n junction to be ~30% at 1.34 eV [21]. In order to achieve this value the semiconductors, seen in Table 2, are often doped to create donor and acceptor states in the forbidden region of the electronic band structure [4] reducing the band gap value in the semiconductor. Doping can be done in several ways but always involves extra pretreatment steps of the semiconductor material [22], often after extensive purification processes, incurring additional costs to any material/device fabricated from these semiconductor materials.

Modification of the HP band gap is a much more facile process, involving simply altering the ratio of the halides [23], [24], or metal [25] in the precursor solution prior to crystallization of the HP material. Altering the ratio of halides effectively allows the HP material to have a band gap at any point between the two pure halide HPs, as seen in Figure 4. The degree to which the band gap of HPs can be tuned makes them ideal candidates the photoactive component in solar cells [26]–[29], photodetectors [30]–[32], and light-emitting diodes [33]–[35].

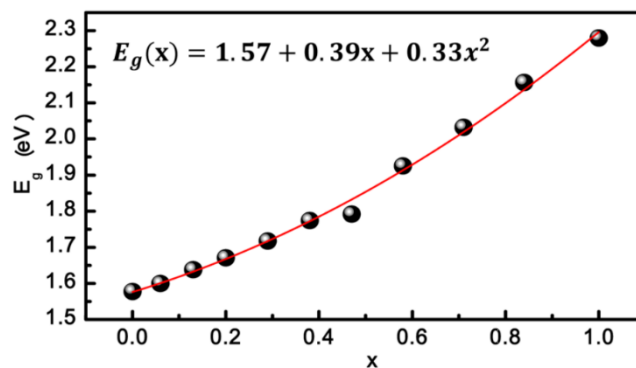


Figure 4. Band gap of $\text{CH}_3\text{NH}_3\text{Pb}(\text{I}_{1-x}\text{Br}_x)_3$ HP as a function of the ratio of halides. The gambit of band gaps available depend on the halide concentrations and can vary from 1.5 eV to 2.3 eV. Adapted from [23].

Band gap tuning through altering the ratios of metal (Pb and Sn) in the HP material allows similar access to band gap values in between the unaltered HPs. It can be seen in Table 2 that the band gaps of the lead iodide HP and the tin iodide HP span the ‘ideal’ band gap as predicted by the Shockley-Queisser limit, and as such current research is focused on the creation of stable mixed metal/mixed halide HPs in order to achieve an ideal value of 1.34 eV [36].

2.2.3.4. Issues with HP Materials

Given the aforementioned desirable material properties that make HPs so seemingly attractive to the creation of opto-electronic devices it’s somewhat surprising that they have not yet been deployed on any scale in the photovoltaic industry since 2012. The reason limiting the wide-scale use of HPs in opto-electronic applications stems from the intrinsic chemical instability of the HP material itself [37]. In particular, the lead iodide species of the HP, which is the most desirable opto-electronically, is particularly unstable. Several environmental factors play a role in the rapid degradation of HP materials, the most notable of which is moisture; however, ultra-violet (UV) radiation[38] and heat [39] also play a role in the degradation of HPs.

The degradation due to the presence of moisture is a multi-step process: first two hydration steps occur forming first a monohydrate and dihydrate species [40], as seen in Figure 5.

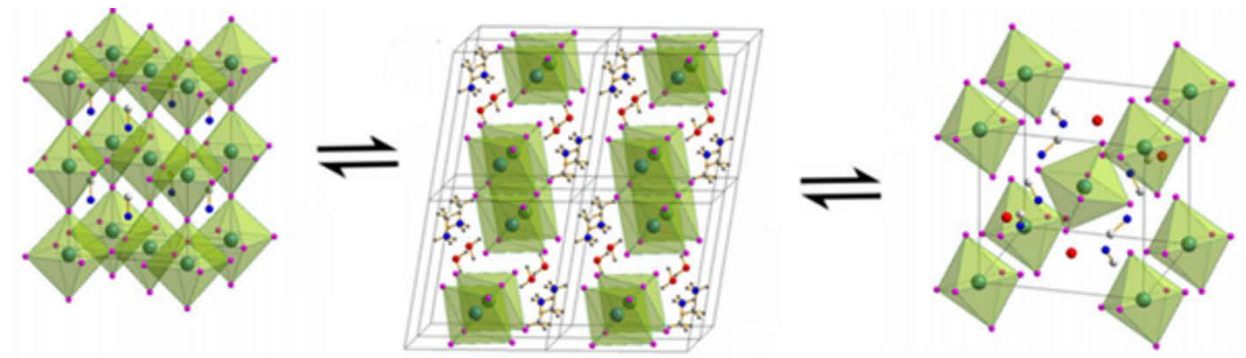
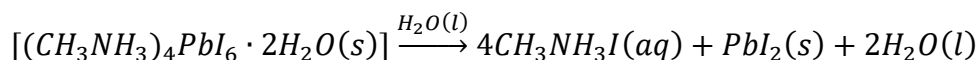


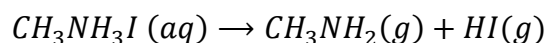
Figure 5. Disorder in the HP crystalline lattice increases as the material is increasingly hydrated. The increase in disorder results in a decrease in symmetry and thereby conduction along the Pb-I-Pb chains in the crystal structure. Adapted from [40].

The water molecules are attracted strongly to the methylammonium and result in an increased level of disorder in the HP crystal structure. Opto-electronic properties of the HP material are strongly tied to the order in the halide-metal-halide network across the crystal; therefore, as the disorder increases, the ability of the material to act as an absorber is diminished [41]. While diminishing performance the hydration reactions are reversible, and the HP layer is recoverable until liquid water condenses on the HP crystal itself at which point the HP degrades irreversibly as described by equation 2.



Equation 2. Complete degradation of methylammonium lead iodide perovskite dihydrate via exposure to liquid water [40].

As the reaction in equation 2 proceeds to the right, the aqueous methylammonium iodide undergoes further degradation into its consistent chemical components, methylamine and hydroiodic acid, seen in equation 3.



Equation 3. Degradation of methylammonium iodide into methylamine gas and hydrogen iodide gas.

Both methylamine and hydroiodic acid are highly volatile species that evaporate and continue to drive the degradation reactions toward the degradation products resulting in the complete degradation of the HP material. Given that the degradation of the HPs in all cases is a mass transport phenomenon, attempts at mitigation often involve tailoring the chemistry of the HP by altering the halides [23], the metal cation [42], or through encapsulation by hydrophobic hole transport layers (HTL) [43].

The sensitivity to UV radiation is brought about by the TiO₂ present in most solar cells which act as electron transport layers (ETLs). Photoelectrons at the TiO₂/HP interface oxidize and degrade the HP material. Efforts to mitigate the sensitivity to UV radiation involve the replacing the TiO₂ with Al₂O₃ as the mesoporous scaffolding structure [38]. Encapsulation with an optical polymer such as polystyrene (PS) or polymethylmethacrylate (PMMA) would also aid in the filtering of the UV radiation before reaching the TiO₂/HP interface.

Thermal stability of the HP material is only an issue at high temperatures (> 230 °C) during fabrication/processing steps, at which point the organic component of the HP sublimates [39]. In the scope of this research project, the high temperatures during processing only became an issue during melt ES which will be addressed in the melt ES HP composites chapter.

2.3. Electrospinning

The process of ES is achieved through the electrostatic draw down of a polymer solution or melt resulting in the creation of micro/nano sized polymer fibers. A large range of process parameters can effect ES [44]; voltage, separation distance, humidity, solution concentration, temperature, and temperature difference, among a whole host of intrinsic chemical/physical properties of the polymer solution/melt [45]–[47], have significant effects on the morphology of fibers produced during the ES process.

Solution ES is the most commonly utilized form of ES. A diagram of the solution ES process can be seen below in Figure 6. Typically, a polymeric solution is extruded into a high-strength electric field ($\sim 1\text{kV/cm}$), where it polarizes and is drawn towards a counter electrode. Solution ES typically allows for the creation smaller diameter fibers ($\sim 10\text{ nm}-1\mu\text{m}$).

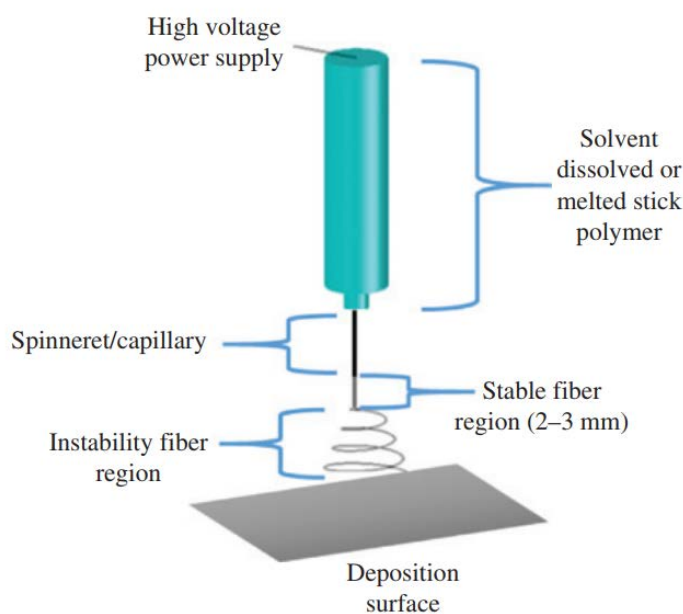


Figure 6. A typical ES apparatus where a polymer melt or solution is extruded into a high strength electric field, upon which it is polarized and due to repulsive coulombic surface charge interactions a polymer jet is emitted from the polymer droplet resulting in the formation of a micro/nanofiber. Adapted from Skinner *et al.* [48].

Melt ES follows the same principals as solution ES; however, a heating element is typically employed to liquefy a solid polymer, in lieu of a polymeric solution. The chief advantage in melt ES is the lack of a need for a solvent, which can be prohibitive to certain sensitive or incompatible materials. Additionally, melt ES can provides thermal energy to drive solid-state reactions in the melt ES apparatus *in situ*.

2.4. Polymer Composites

Composite materials are, at their simplest, a mixture of two disparate materials with the overall goal of adding desirable properties present in one material to another, as seen in Figure 7.



Figure 7. Diagram of a typical composite with a continuous matrix phase and a dispersed filler phase. Agglomerations of the filler phase can occur when the polymer melt/solution does not wet the filler particles, whereas a well-dispersed composite is the result of a high degree of wetting of the filler phase.

Usually, one material is added in a smaller fraction relative to the other. These two materials are often referred to as the filler phase (smaller fraction) and matrix phase (larger fraction).

Polymer composites have gained increasing notoriety since the creation of the first glass fiber reinforced polymers in the 1930s by Owens Corning [49], which rapidly increased in

production during World War II. Eventually in the 1960s, carbon fiber began to replace glass fibers as filler phase material drastically improving material performance resulting in 'space-age' composites used in aerospace and high-end applications. As the ability to produce nanoscale carbon allotrope dopants, along with other micro and nanoscale dopants, has improved over the last 30 years, so too has the ease with which polymer composites can be functionalized. Where it used to take up to 60 vol% loading with polymer microcomposites to coalesce a desired property from the filler to the composite, with polymer nanocomposites that loading fraction has been driven down to an average of 5 vol% [50]. As the ability to produce smaller dopants materials improves, it can be expected that polymer nanocomposite functionality too should improve.

2.4.1.1. Percolation Theory

In order to elicit useful electrical properties out of binary composites where one material is conductive and the other is insulating, it is necessary to reach a critical loading fraction to achieve electrical conduction. At loading values less than the critical value for electrical conduction, the conductivity properties of the composite are close to that of the polymer matrix material [51]. As the fraction of conductive filler increases, networks of continuous filler phase start to exist in the matrix material, see Figure 8.

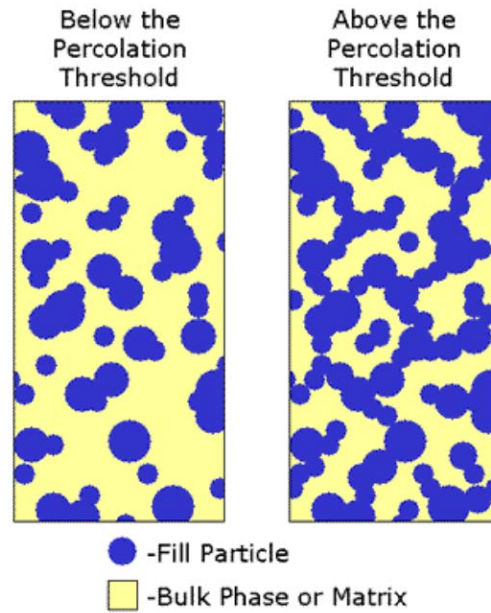


Figure 8. A schematic of a composite material below and above the critical loading to achieve percolation. A continuous network of conductive filler particles form across the composite bulk and allow electrical flow. Adapted from [52].

As the loading approaches the critical value for percolation, the conductivity increases a small amount; and upon reaching the percolation threshold, the conductivity of the composite increases rapidly. After reaching the percolation threshold, the rate of increase in conductivity as more filler is added decreases. A typical percolation plot can be seen in Figure 9.

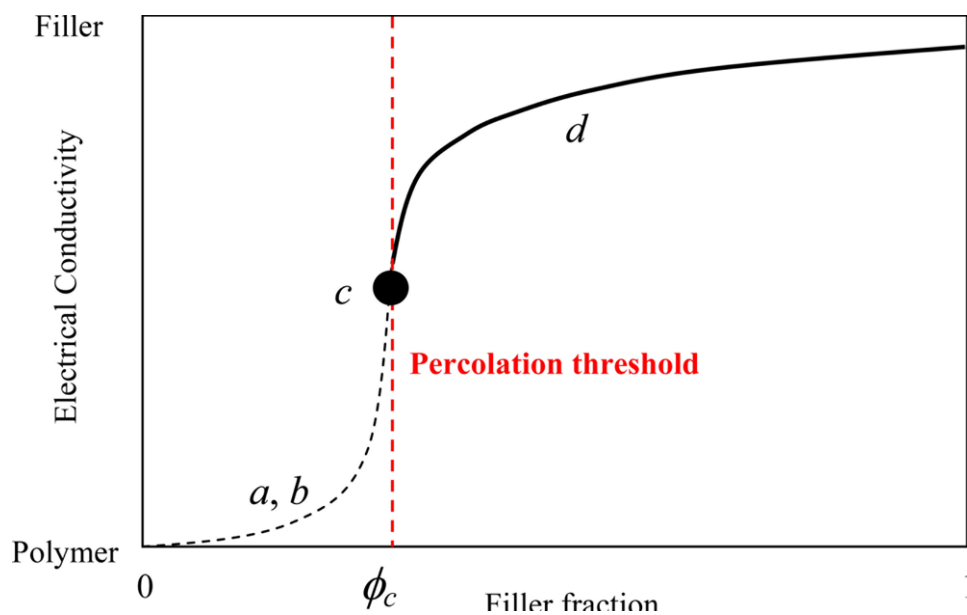


Figure 9. A percolation threshold plot in which the fraction of filler material is plotted against the log of the conductivity. The characteristic S-curve of the percolation threshold follows a power law expression [53].

2.5. Hybrid Perovskite Composites and Microstructures

2.5.1. Hybrid Perovskite Composites

Currently the state of the art in HPs composites is directed mostly at the creation of optically active polymer composites and in the compounding of HPs with conjugated polymers for use in the active layer of solar cells. While both routes produce interesting and functional composite materials, these approaches fail to address the both the moisture stability and cost of production issues that prevent the large scale implementation of HPs in the solar energy market.

Work done on the creation of moisture resistant HP/polymer composites is being done by Wang *et al.* [54] toward the creation of highly luminescent polymer/HP composite films for use in backlit light emitting devices. The polymer film layer itself is not electrically contacted in anyway; instead light is shone through the polymer film where light above the band gap of the HP material is absorbed and re-emitted with energy equal to the band gap energy of the HP material in order to tune the light emitted from the device. The optical properties of the HP material in the composite and the thickness of the layer,

as well as how many layers are present in the device, dictate the color/chromaticity of the light emitted from the device. Wang *et al.* [54] utilized the swelling and de-swelling of polymers to promote the egress of HP precursors into the polymer films, which could then be heated to react and form HP nanoparticles. The polymer films that resulted from the research done by Wang *et al.* [54] demonstrated remarkable moisture resistance and could be completely immersed in water with a minimal change to the luminescent behavior of the film itself. However, while useful in the creation of down-converter films for back-lit light emitting devices, the HP nanoparticles in the composite cannot be effectively contacted electrically and rely solely on optical pumping. Electrically contacting the HP material in the composite is necessary in order to extract photo-generated electrons for light-harvesting and photon detecting applications.

The creation of electrically conducting HP/polymer composites has been achieved through compounding with conducting-conjugated polymers such as PTB7 [55] and PDPP3T [56]. Compounding HP precursor solutions with conjugated polymers prior to use in planar devices allows the passivation of the HP material while also providing a conductive environment around the HP material. Chen *et al.* [56] utilized PDPP3T as the conjugated polymer in a flexible photodetector device. The perovskite material saw an improved moisture resistance when compared to the neat HP film but still experienced a degradation in performance over the course of one week. Wang *et al.* [55] created the composite films through sequential deposition steps and not direct compounding of the polymer and HP precursors. The photo-absorbing HP/polymer films were incorporated into pre-existing planar solid-state solar cell designs and demonstrated a large improvement to the moisture stability of the HP material. As a result the composite photo-absorbing layer solar cell outperformed neat HP films significantly. However, the issue with both the aforementioned HP/polymer composites is in the increase of cost of production of the devices utilizing the conjugated polymer/HP composites. An attractive feature

of HPs is in the low-cost/highly-functional aspect of the material. While the conjugated polymer improves the functionality of the HP layer, the increase in cost associated with the cost of the polymer, which are typically ~\$400/100 mg, increases the cost of production of devices built around the composite material.

2.5.2. Electrospun Hybrid Perovskite Fibers

A relatively small amount of work has been done to electrospin HP/polymer fibers. Current attempts involve the blending of HP precursor materials into a polymeric solution and ES the solution to form micro/nanofibers. Lu *et al.* [57] were able to produce HP nanofibers through blending polyacrylonitrile (PAN) with the PbI_2 HP precursor. The resultant solution was then electrospun and calcined to produce a mesoporous PbI_2 fibers that could be further processed by immersing in a solution of the methylammonium iodide HP precursor. During immersion the PbI_2 was reacted to form a HP nanofiber. However, the issue with the fibers created by Lu *et al.* [57] was similar to an issue presented later in the solution compounding section of this dissertation: the PbI_2 did not completely react. Instead the HP material formed a coating on the exterior of the PbI_2 fiber, leaving unreacted PbI_2 at the center of the fiber. The work done by Chen *et al.* [58] utilized a solution of polyvinylpyrrolidone (PVP) to act as a vehicle during the ES process for both the PbI_2 and methylammonium iodide precursors. After ES the nanofibers were calcined to drive the reaction of the precursors and thermally degrade the polymer in an attempt to leave crystalline HP nanofibers for use in a DSSC device. While the method was more successful at fully utilizing the HP precursor materials due to the good dispersion through the polymer during the ES process, it was not successful in drastically improving the efficiency of the DSSC devices. The lack of improvement in the behavior of the DSSC devices after the addition of the HP nanofibers was a consequence of both the ES fabrication method and the

thermal behavior of the polymer and the HP. In order to fully thermally degrade PVP, temperatures in excess of 400 °C must be utilized. However, HP materials are limited to a maximum temperature of 300 °C before the onset of thermal degradation. Therefore, in the final nanofibers there is still a significant amount of PVP hampering the ability of the HP material to perform electrically.

3. Creation and Characterization of Hybrid Perovskite-Polymer Composites

The creation of HP-polymer composites is attractive for three reasons: (1) encapsulation/passivation is easily achieved while materials are being processed; (2) if compounded with optical polymers, optical functionality is maintained; and (3) fabrication is facile, preserving the low-cost for HP devices and materials. Over the course of this research, several compounding techniques were utilized in the creation of HP/polymer composites; melt compounding and solution compounding both offer unique capabilities in how the filler phase of the composite is compounded into the matrix phase in addition to how the composite can then be deployed after creation. In the following chapter, the creation of composite materials through melt compounding and solution compounding will be discussed in detail, along with the subsequent optical and electronic properties of the composite material generation.

3.1. Polymer Melt Compounding

Polymer melt compounding was first explored as a method for the creation of HP/polymer composites. Polymer melt compounding is the most simple and direct method of producing polymeric composites, as a heat source and mixing container are the only requisite apparatus necessary to create simple composites at low cost. For the melt compounding of HP and polymer materials, the simple system shown in Figure 10 was used.

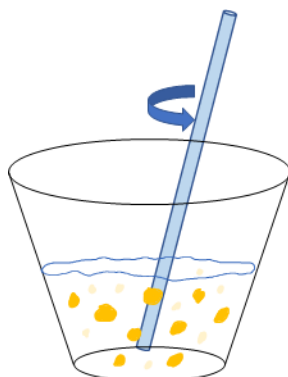


Figure 10. A schematic of the setup used for producing HP-polystyrene composites through melt compounding. A crucible is heated to the melting temperature of the polymer and through stirring with a glass stir rod the HP precursors are spread through the polymer melt.

The neat polymer base material was loaded into the crucible on the hotplate and heated until a liquid polymer melt was created. Filler material was added and mixed with a stir rod until the melt mixture appeared homogenous to the unaided eye at which point it could be cast into a mold.

Initial attempts at the creation of HP-polymer composites were carried out using polypropylene (PP) as the base polymer. The selection of PP for use as the base polymer was justified by its low-cost, high degree of processability and for its relatively low melting point (~ 185 °C) [59]. An early attempt at melt compounding with PP can be seen in Figure 11.

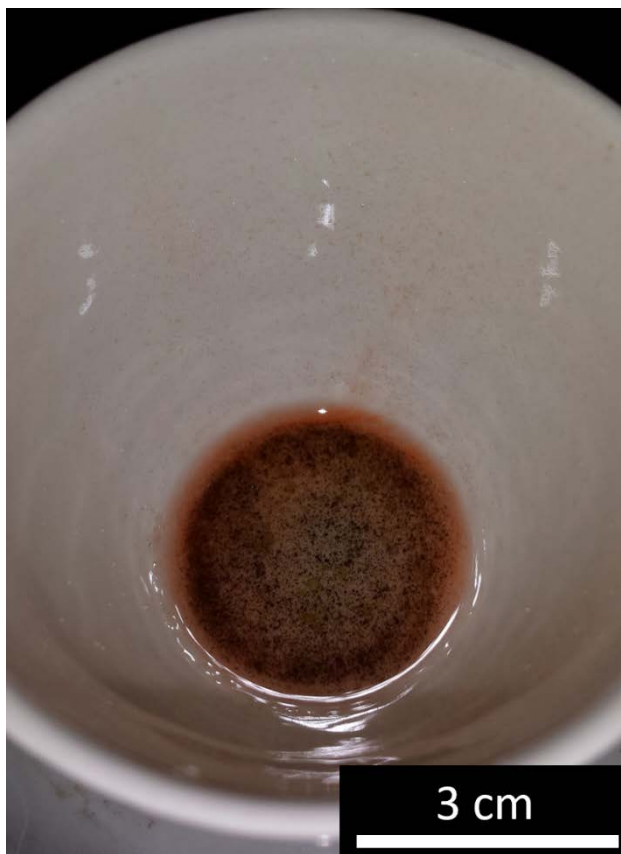


Figure 11. A polypropylene melt with HP precursors mixed in simultaneously. The simultaneous mixing resulted in the agglomeration of HP crystallites through the polymer melt.

The simultaneous addition of the HP precursors resulted in the formation of microcrystallites, which can be seen in Figure 11 as the relatively large black particles in the polymer melt. The black particles in the polymer melt were a strong indicator that the attempt to synthesize HP was successful, as the typical perovskite reaction is observable as a color change from yellow to black. Additionally, the orange hue of the polymer melt is indicative of unreacted lead iodide, which informed the decision to maintain the melt mixture at temperature after initial HP precursor addition and mixing. A sample was drawn from the polymer melt, dropcast, and

imaged using Hitachi S-4500, Tescan Mira3, and Zeiss SUPRA 55VP scanning electron microscopes (SEM) which can be seen in Figure 12.

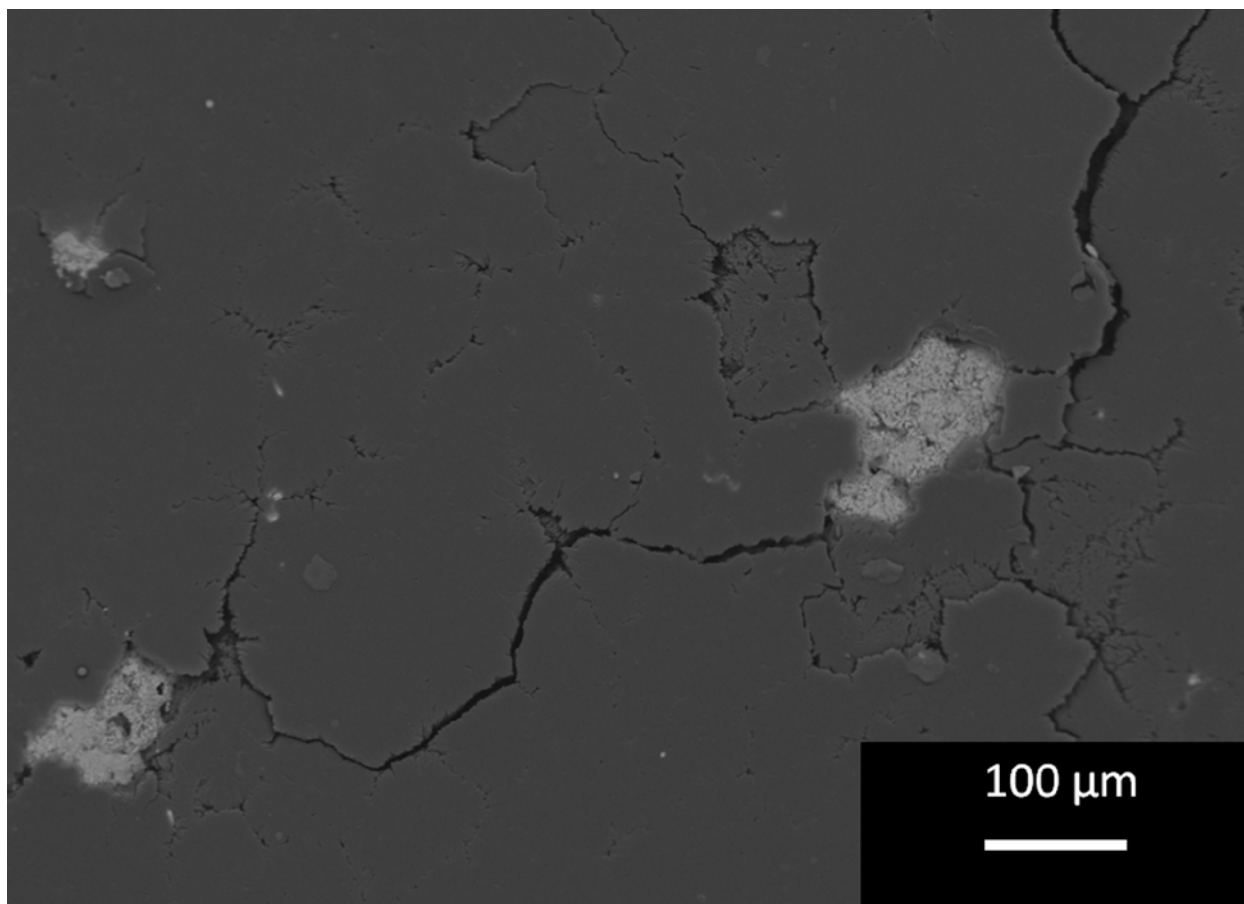


Figure 12. Electron micrograph of HP crystallites embedded in a polypropylene matrix. The bright grey spot on the upper right has a Pb:I ratio of (1:2.25), and the crystallite on the bottom left has a ratio of (1: 4.79), as determined by EDS.

Embedded HP microcrystallites can be seen in the PP matrix in Figure 12. Both HP crystallites are non-stoichiometric in respective lead-to-iodide ratios, which are expected to be 1:3 in the ideal HP crystal. However, while the crystallites are not ideal in chemistry, size, or distribution in the PP matrix, this does represent the first time that HPs were successfully synthesized in a

polymer melt. In order to further study the composite, a molding apparatus was utilized, seen in Figure 13.



Figure 13. Molding apparatus used to create circular disk of composite media. Polypropylene base material can be seen melting in the washer suspended on a glass slide on a heated aluminum block.

During the testing of the molding apparatus seen in Figure 13, PS became the clear polymer of choice for the matrix phase due to optical properties of bulk PP in addition to difficulties in removing the material from molds without breakage.

A PS polymer waste stream produced from recycled petri dishes was sourced from the Army Research Laboratories (ARL) in Aberdeen, MD (MW = 229,700, determined by gel-permeation chromatography at ARL). A similar procedure for the creation of the composite was followed when using the PS material, except for the addition of the HP precursor materials. Previously, the HP precursor material had been added simultaneously to the polymer melt and as a result the HP crystallites formed in the melt had been large and non-ideal in stoichiometry. In an effort to

mitigate this issue, the PbI_2 HP precursor was added to the polymer melt and blended into a homogenous mixture, as observed by the unaided eye, as seen in Figure 14.

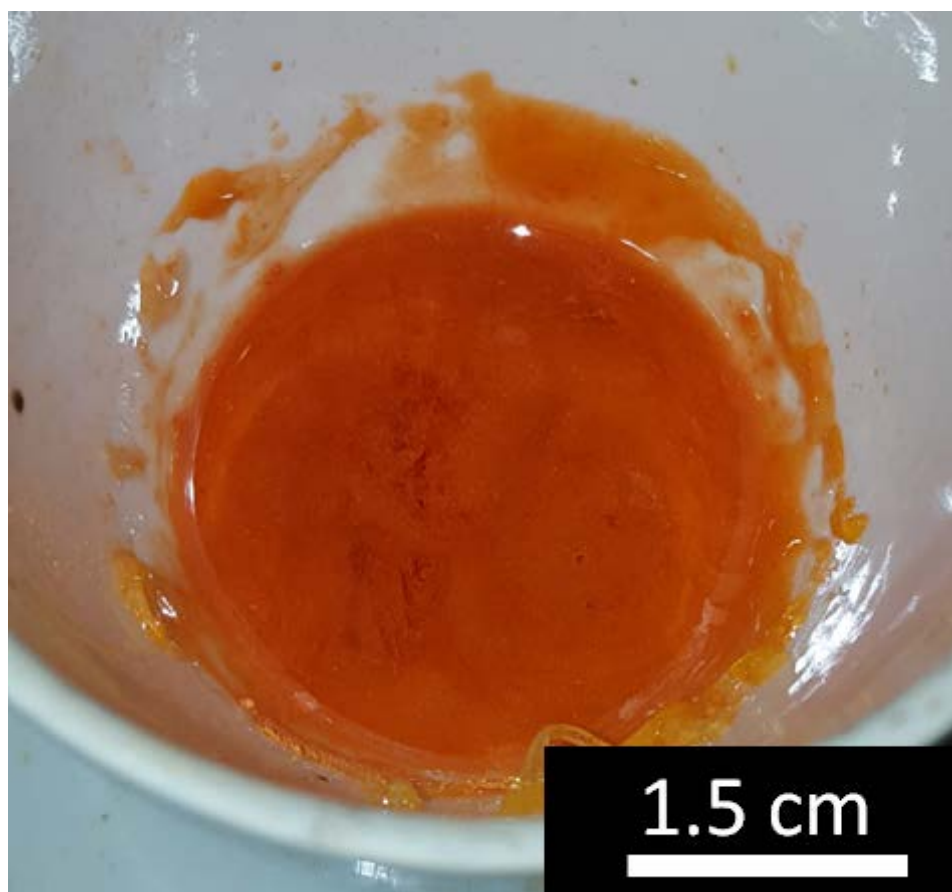


Figure 14. Polystyrene melt blended with PbI_2 . The mixture pictured has not yet reached a state of homogeneity desired prior to mixed with the $\text{CH}_3\text{NH}_3\text{I}$ precursor to initiate the HP reaction.

The quantity of PbI_2 added to the polymer melt was determined by the final weight percent desired in the composite material. For the initial study, the weight loading of HP in the composite was determined empirically with implications in both processability and characterization ease under UV spectroscopy. A weight loading of 40 wt% was eventually determined to produce the composite samples that may be consistently processed or characterized. Upon addition of the $\text{CH}_3\text{NH}_3\text{I}$ precursor to the polymer melt with the PbI_2

precursor already thoroughly blended, the HP reaction was observed to occur nearly immediately turning the composite from an orange-yellow to a solid black. After mixing the melt was allowed sit at temperature for 10 min to allow the precursors to completely react. The polymer melt was then used to fill the molding apparatus pictured in Figure 13 and produce circular disk samples as pictured in Figure 15.

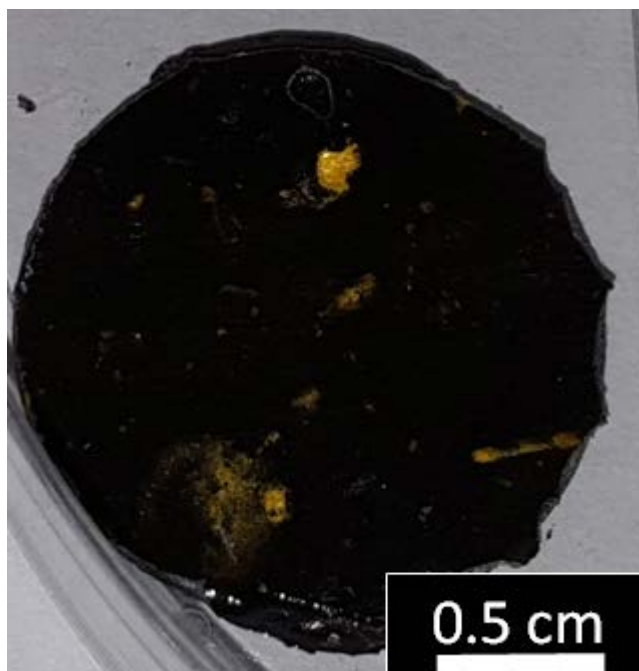


Figure 15. HP/polystyrene composite sample after molding and release. Unreacted PbI₂ throughout the sample was a consistent issue in the initial studies.

Unreacted bright-yellow PbI₂ can be seen in Figure 15. The unreacted precursor was a consequence of both inadequate ability to thoroughly mix the melt itself and the decreased rates of reaction due to the retarding the diffusion of the precursors caused by the polymer melt. The dispersion of the HP filler phase in the composite media was relatively good, with minimal clustering, as seen in Figure 16.

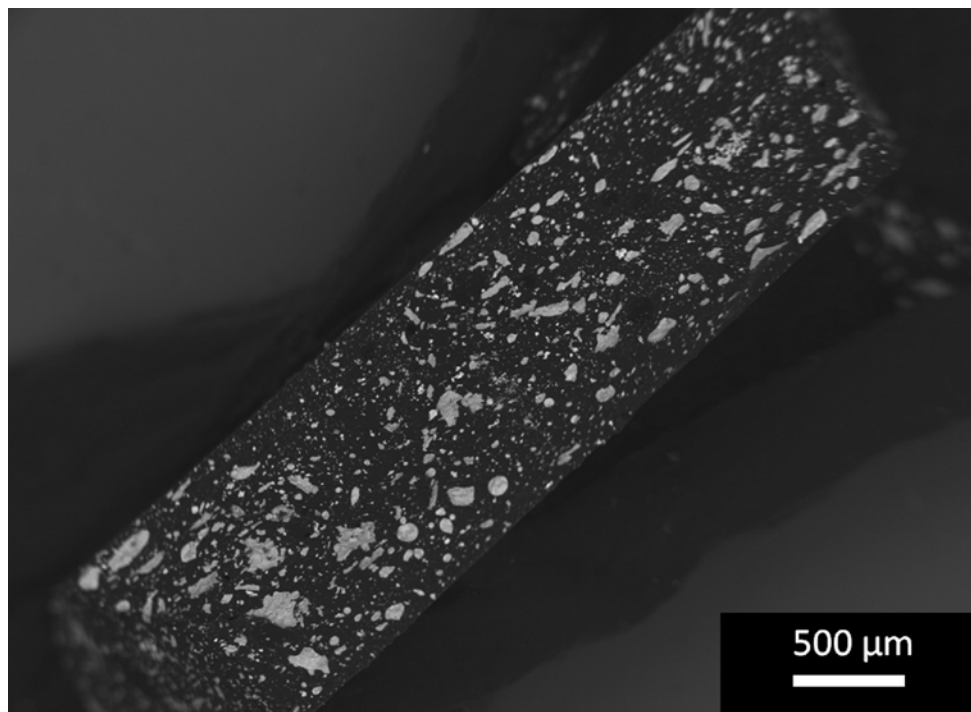


Figure 16. Cross-sectional electron micrograph of the HP composite circular sample taken shortly after casting. Adapted from Murphy *et al.* [60].

The micrograph in Figure 16 shows the breadth and depth of HP crystallites throughout the PS matrix phase, in addition to unreacted precursors present in the final composite. Elemental analysis of the crystallites from Figure 16 can be seen below in Figure 17.

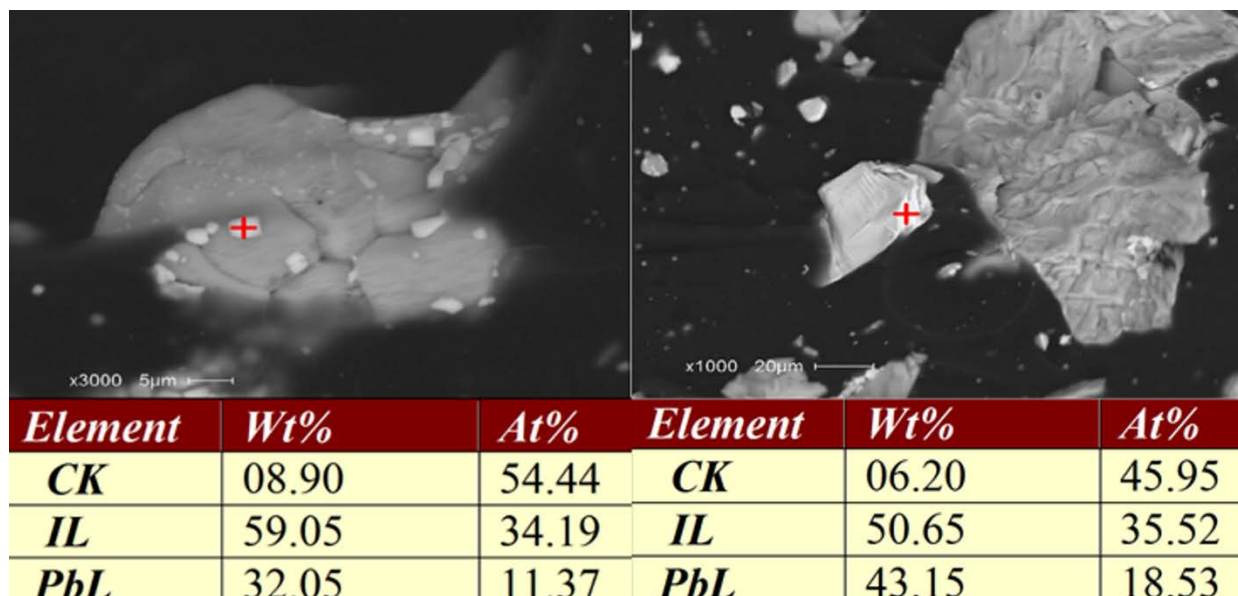


Figure 17. Energy-dispersive spectroscopy of crystallites present in the HP-polystyrene composite seen in Figure 14. The $\text{CH}_3\text{NH}_3\text{PbI}_3$ perovskite can be seen on the left as evidenced by the ratio of the atomic percent of Pb:I. However, crystallites of unreacted PbI_2 remain in the composite, as shown on the right, and also evidenced by the ratio of the atomic percent of Pb:I. Adapted from Murphy *et al.* [60].

Figure 17 shows the synthesis of the HP in the polymer melt was successful on the microscopic level. Additionally, it appears that the HP crystallites may grow from the external surfaces of the PbI_2 crystallites in the polymer melt. The growth from the external surfaces of the PbI_2 crystallites is expected in a solid-state reaction where the mechanism for driving reactions is colloquially termed ‘heat and beat’ [61]. In the case of the HP reaction, the heating is amply supplied in the form of localized heat transfer from the polymer melt environment. However, the beat component responsible for driving the solid-state HP reaction is somewhat lacking in the simple stir mixing. A common solution to driving solid-state reactions when the necessary mechanical mixing is not or cannot reasonably be achieved is to increase the temperature of the local environment to improve diffusion of reactants and drive the reaction to completion. In the case of the HP reaction, the temperature is limited due to the sublimation of the $\text{CH}_3\text{NH}_3\text{I}$

precursor at $247\text{ }^{\circ}\text{C} \pm 26\text{ }^{\circ}\text{C}$ [39]. A similar issue was encountered while utilizing sonochemical synthesis techniques and was addressed through modification of the PbI_2 precursor prior to synthesis and will be discussed in detail in section 4.2.

In addition to the EDS elemental analysis to confirm the presence of HP material in the composite material, UV-Vis spectroscopy was utilized to elucidate the chemical nature of the composite through optical interactions. The HP of interest in the melt compounding study, $\text{CH}_3\text{NH}_3\text{PbI}_3$, has a characteristic optical absorption onset at 760 nm [62], whereas the PbI_2 precursor has an optical absorption onset at 530 nm [63]. UV-Vis absorption spectra for $\text{CH}_3\text{NH}_3\text{PbI}_3$ and PbI_2 can be seen in Figures 18 and 19, respectively. Characteristic and non-overlapping optical absorption onset allows HP material to be identified after synthesis and provides a qualitative metric for the success of the synthesis procedure. Additionally, the shift in absorption intensity from 760 nm to 530 nm in the same sample can provide an understanding as to the relative amount of degradation occurring in the sample. The shift/decrease in the absorption peaks is utilized in the next section to track the degradation of composite samples.

The last detail elucidated from the study of HP synthesis in polymer melts was not immediately apparent during the study itself and was realized in light of new information gleaned after learning of a unique property of HPs. Zhou *et al.* discovered that exposing HPs to methylamine (CH_3NH_2) results in the collapse of crystalline structure creating a liquid HP [64], seen in Figure 20. The nature of the reaction of the methylamine gas with the solid HP is not completely understood.

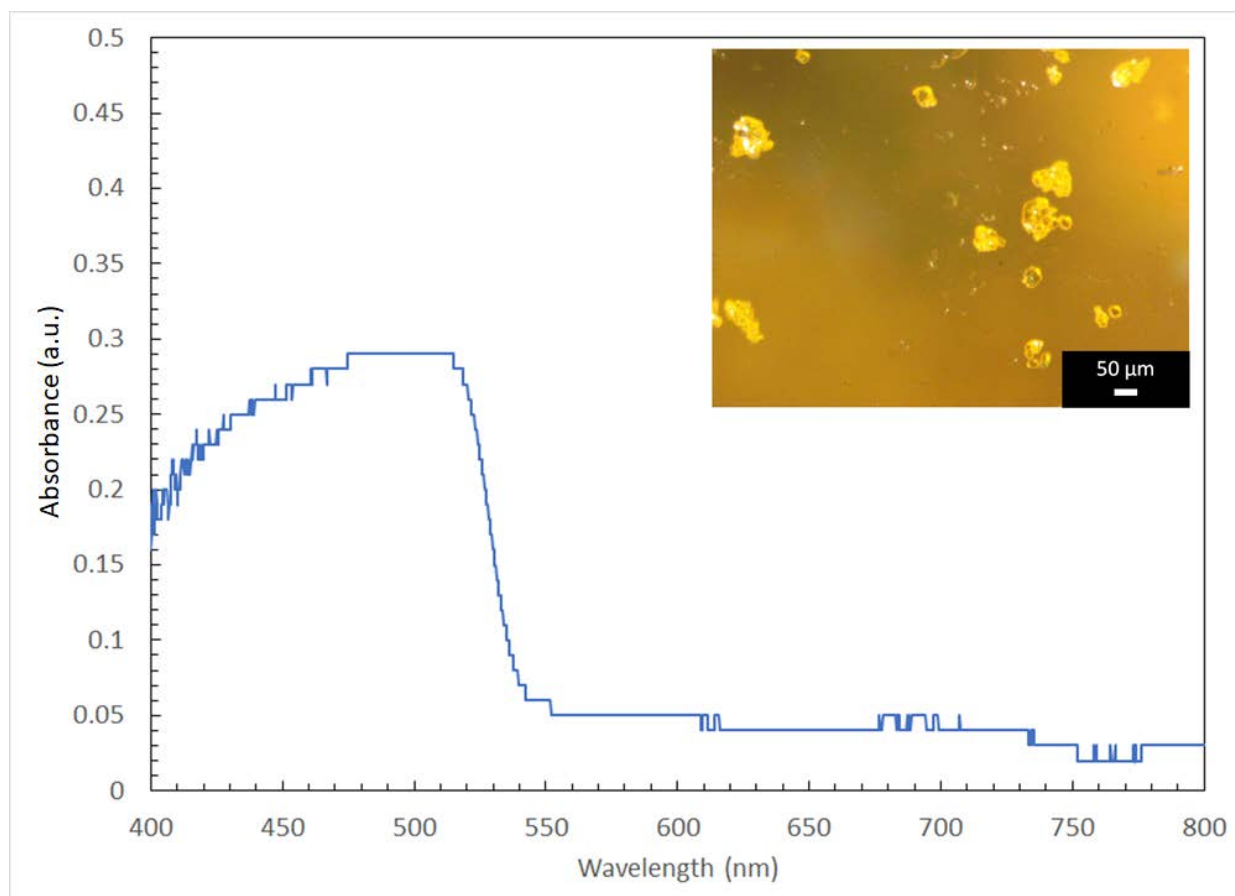


Figure 18. UV-Vis absorption spectrum for PbI₂ in polystyrene. (Inset) Optical micrograph of PbI₂ crystallites embedded in a polystyrene matrix.

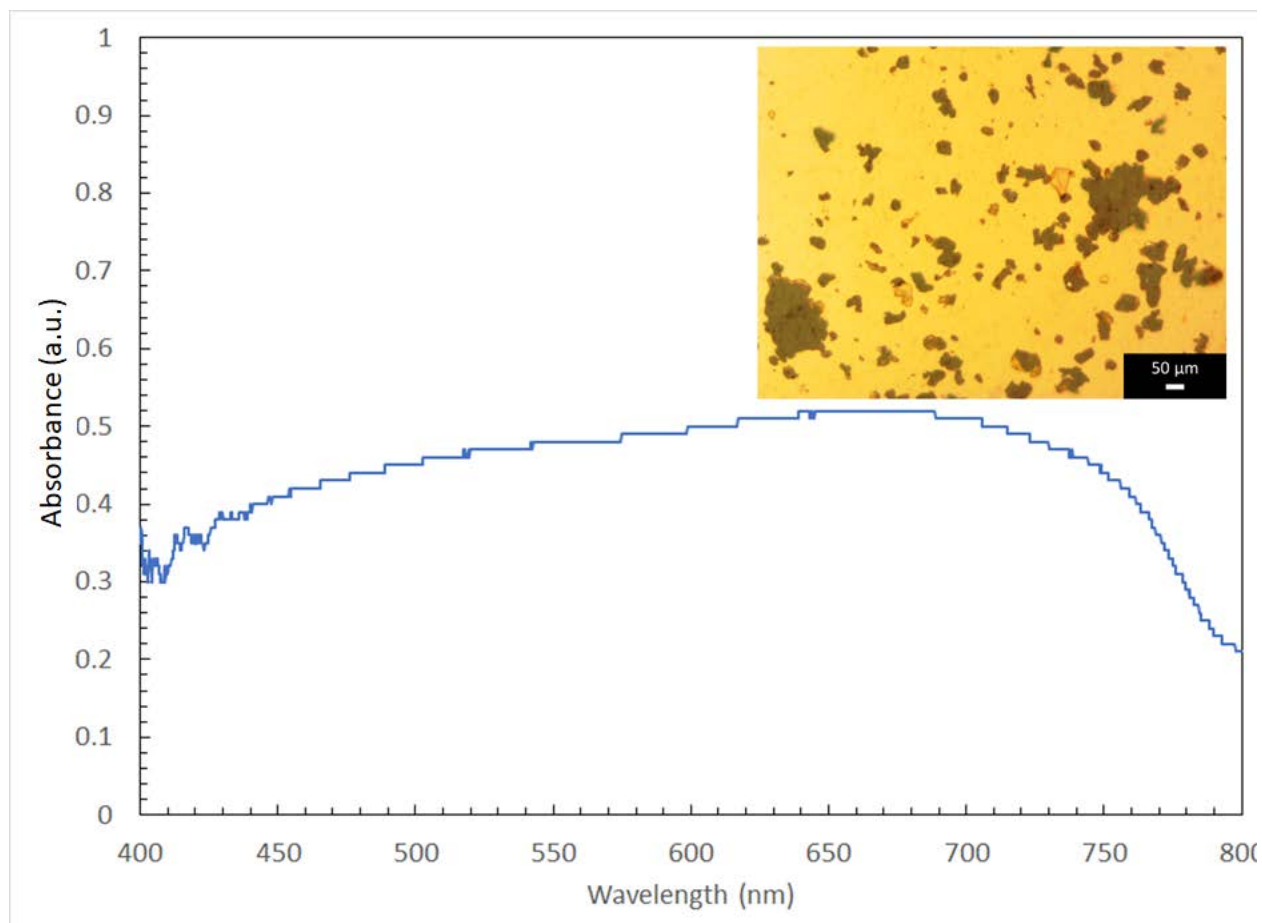


Figure 19. UV-Vis absorption spectrum for $\text{CH}_3\text{NH}_3\text{PbI}_3$ HP thin film dropcast onto a glass slide. (Inset) Optical micrograph of $\text{CH}_3\text{NH}_3\text{PbI}_3$ crystallites embedded in a polystyrene matrix.

However, it is believed by Zhou *et al.* that the lone pair on the nitrogen in the methylamine interact with the PbI_6 octahedra in the HP structure and collapse the crystallite structure resulting in the creation of a liquid, as seen in Figure 18.

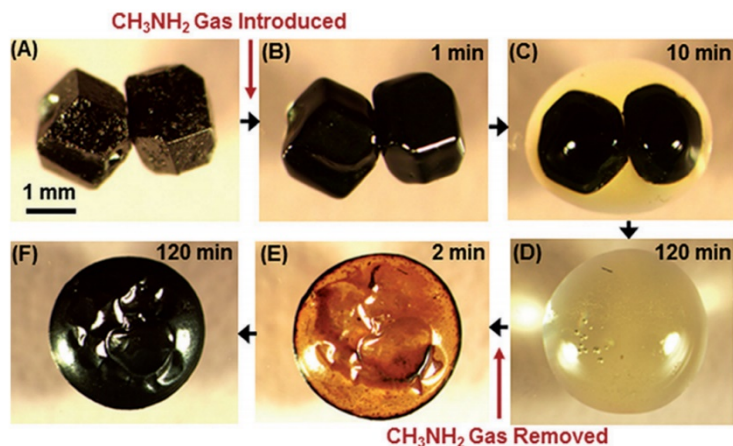


Figure 20. The effect of methylamine gas on the physical state of $\text{CH}_3\text{NH}_3\text{PbI}_3$ HP. Adapted from [64].

Upon removal of the methylamine gas through simple volatilization, the HP reverts to its solid crystalline state without any detriment to the opto-electronic material properties [65], [66]. While no methylamine gas was utilized in the creation of the HP composite through melt compounding, several crystallites in the composite demonstrate amorphous-like morphologies, as shown in Figure 21.

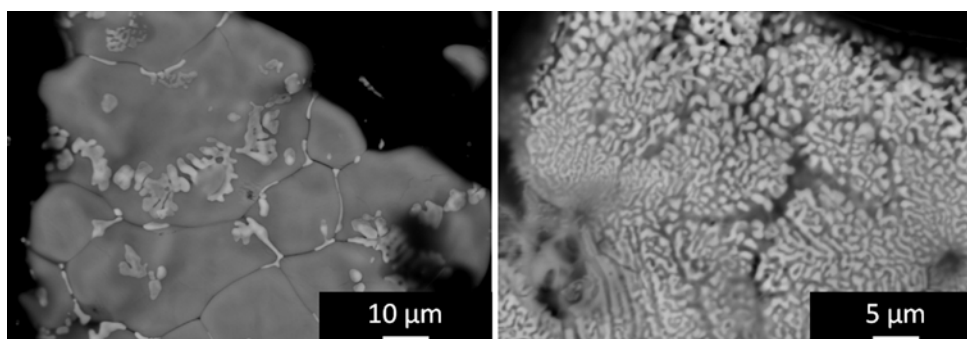
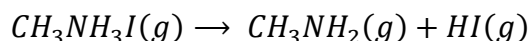


Figure 21. Electron micrographs of crystallites present in the composite media. EDS analysis determined the bright material in both micrographs was HP material. The amorphous-like morphology of the material appears to have formed as a result of the HP material being in a liquid state. Adapted from Murphy *et al.* [60].

The change from a typical crystal habit of $\text{CH}_3\text{NH}_3\text{PbI}_3$ to an amorphous-like shape can be seen in Figure 18. Similar formations are observed in the electron micrographs in Figure 19. It is reasonable to assume that in the closed crucible held at temperatures near the sublimation point of $\text{CH}_3\text{NH}_3\text{I}$ [39] a small amount of the precursor underwent a degradation, as shown in equation 4.



Equation 4. Thermal decomposition reaction for methylammonium iodide into methylamine gas and hydrogen iodide gas.

A small amount of methylamine gas in the crucible would have a small effect on the majority of crystallites present in the melt. Areas near large agglomerations of unreacted $\text{CH}_3\text{NH}_3\text{I}$ precursor would experience the greatest concentration of the methylamine gas and therefore see the largest amount of amorphous-like HP material, which is the case in Figure 19 where the amorphous structures appear to have formed around small clusters of $\text{CH}_3\text{NH}_3\text{I}$ precursor still present in the composite.

3.1.1. Accelerated Ageing Study

The principal reason for the melt compounding of the HP with the PS was to improve the moisture resilience of the HP material. While highly transparent to the visible-light spectrum and of relatively low-cost, PS is also a hydrophobic polymer and potentially super hydrophobic given the necessary surface patterning [67]–[70]. Through compounding it was hypothesized that the hydrophobic properties of the PS would limit the egress of water into the composite bulk and thereby minimize the degradation of the HP material. Furthermore, as mentioned previously, the degradation of the HP material is driven by mass transport phenomena [62], particularly in the dissolution of $\text{CH}_3\text{NH}_3\text{I}$ and its subsequent breakdown into gaseous hydrogen iodide (HI) and

methylamine (CH_3NH_2). However, as is the case with water and PS interacting where a highly polar small molecule (water dipole: 1.85 D) and a non-polar polymer (styrene dipole: 0.13 D) repel each other, the interaction between methylamine (dipole: 1.31 D) and PS is similarly repulsive. The repulsive interaction between the methylamine and the PS would effectively retard mass transport of the gaseous methylamine out of the bulk composite, thereby significantly slowing the degradation of the HP material.

In order to test the improved resistance to moisture-driven degradation, an accelerated ageing study was carried out using a custom-built humidity chamber, as seen in Figure 22. An Omega RH-USB sensor was used to monitor humidity and temperature during the ageing process. Composite samples were stored in the chamber in petri dishes with skewed lids to prevent condensation from dripping directly onto the samples.



Figure 22. Custom humidity ageing chamber which enabled the rapid ageing of HP composites in high humidity conditions. Humidity and temperature ($RH\ 90.3\% \pm 4.9\%$ at $20.24\ ^\circ C \pm 1.26\ ^\circ C$) monitored continuously using an Omega RH-USB sensor. Inset, a schematic of the components of the humidity chamber.

Samples were maintained in the humidity chamber over the course of seven days to achieve the desired rapid degradation brought on by moisture. A graph of the humidity and temperature conditions during the study can be seen in Figure 23.

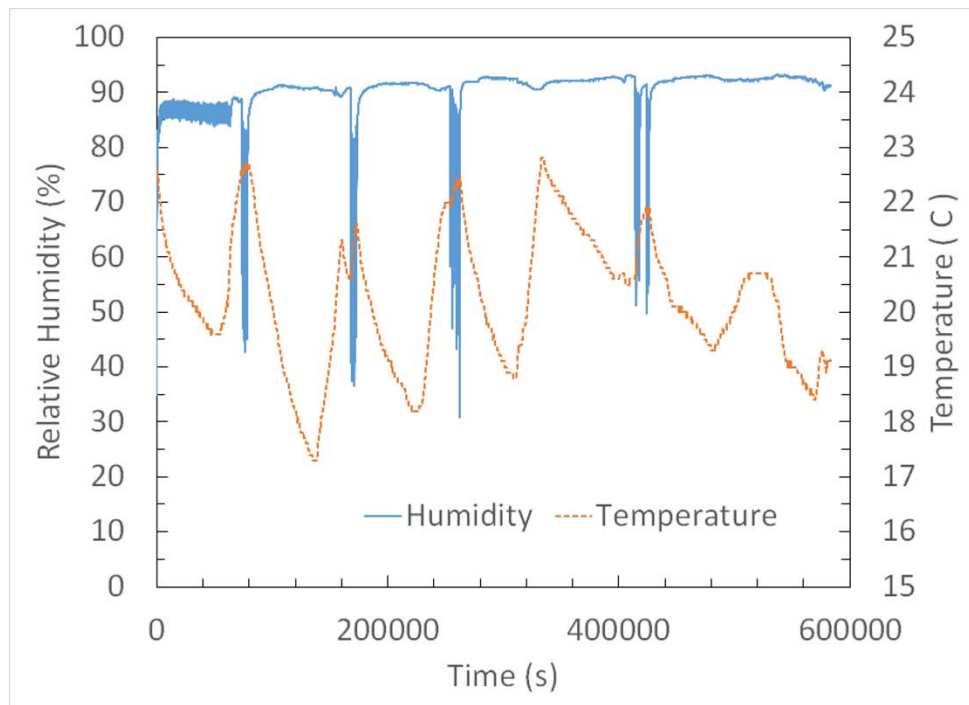


Figure 23. Humidity and temperature conditions in the humidity chamber over the course of the study. The large and rapid drops in the humidity correspond with the chamber being opened to extract samples for characterization. Subsequent increases and decreases in temperature are likely the result of added heat by the experimenter and evaporative cooling to reconstitute the humidity.

The fluctuations in the humidity and temperature seen in Figure 23 were the result of opening the humidity chamber to extract the composite samples for characterization and were then immediately replaced. A far-field probing station was employed in the characterization of the composite samples. The configuration of the probing station can be seen in Figure 24.

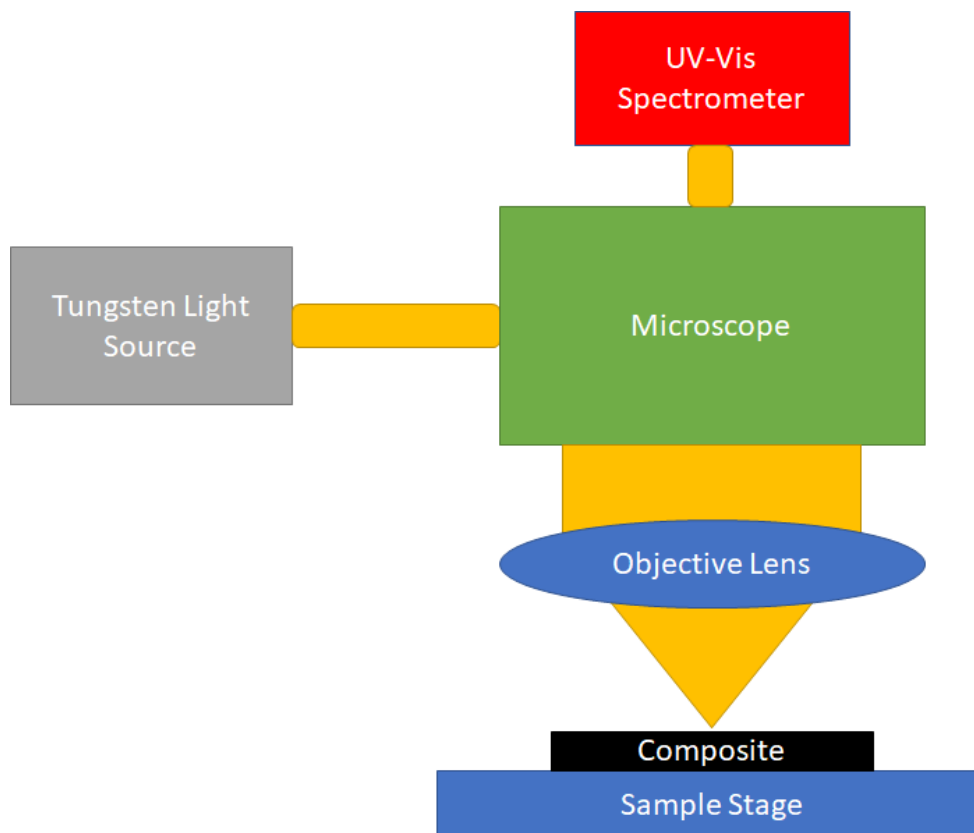


Figure 24. Schematic of the far-field probing station configuration used in the investigation of the composite samples during accelerated ageing. Light from the tungsten source could be focused onto a sample to interrogate a precise location consistently.

Light from the tungsten light source was focused onto similar locations on the composite samples through use of the datum marks scored onto the samples. Penetration of the interrogation light into the sample is crucial in investigating the degradation through the bulk of the composite. Therefore, theoretical absorbance of PS and HP were determined using literature values for the refractive index (n) and the dampening coefficient (k) for PS [71] and

$\text{CH}_3\text{NH}_3\text{PbI}_3$ HP [12]. A graph showing the calculated theoretical values for the absorbance can be seen in Figure 24.

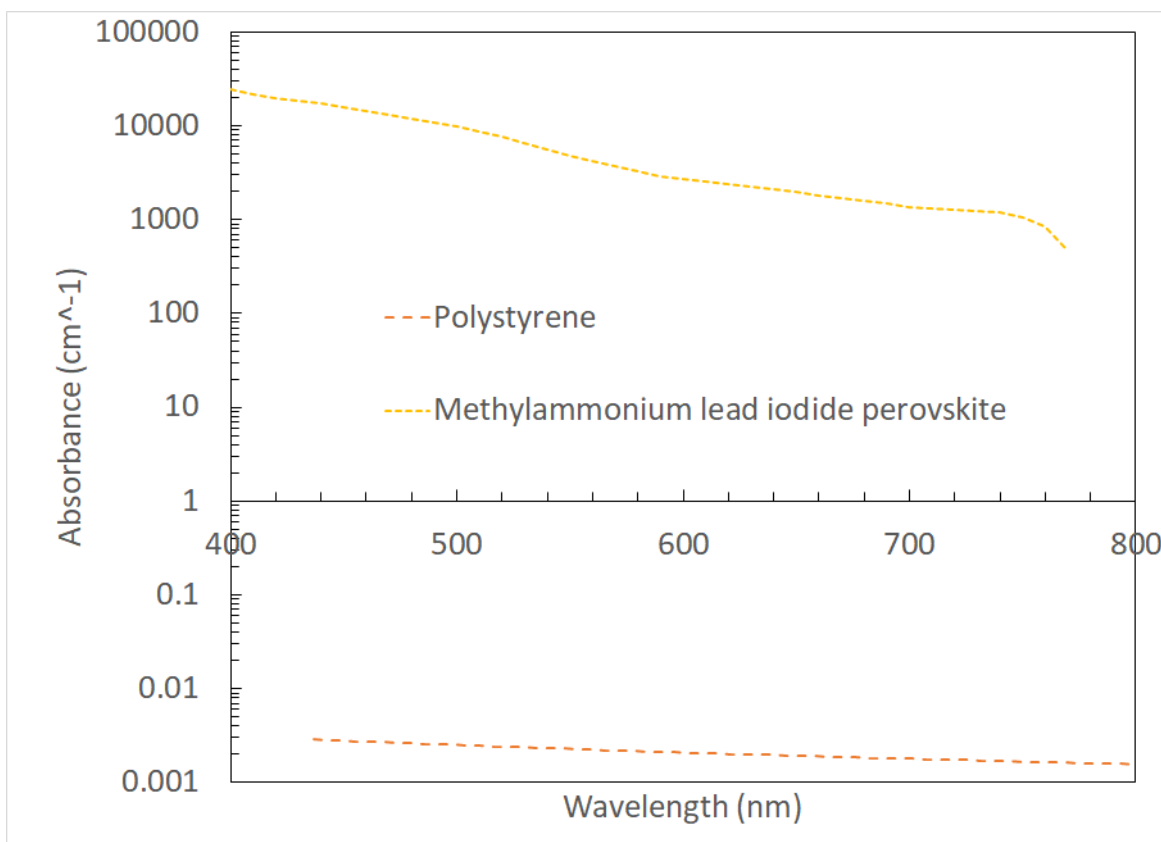


Figure 25. Theoretical absorbance values for polystyrene and $\text{CH}_3\text{NH}_3\text{PbI}_3$ HP. The data shows that while polystyrene is highly transparent through the visible spectrum the case is not the same for the HP that begins to absorb strongly near 760 nm and increases logarithmically into the UV.

The trends in the absorbance seen in Figure 25 demonstrate the viability of the aforementioned interrogation technique. As light passes through the PS matrix phase, it is scattered by the HP crystallites, as seen in Figure 26.

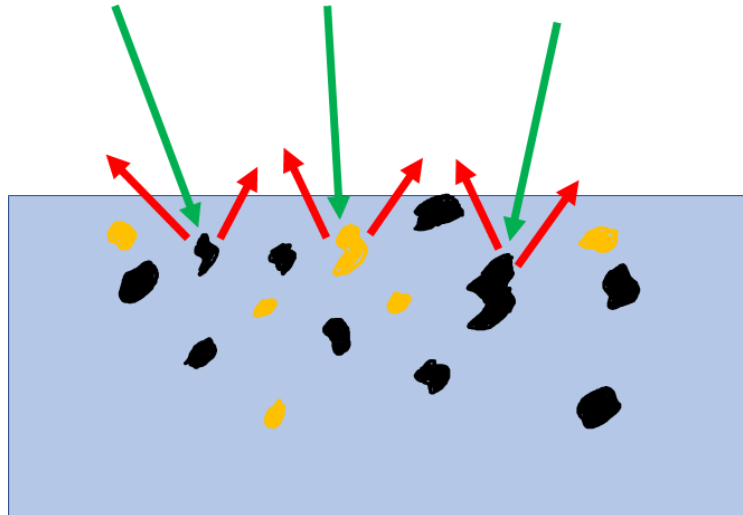


Figure 26. Light rays incident on the composite from various trajectories. The simplified drawing does not show the effect of the higher refractive index of the composite media. Incident light is visualized as a green arrow, where scattered light is depicted as red arrows.

The HP crystallites through the composite bulk can be expected to act as ideal scattering sites, in that they should scatter light with an intensity dependent on the cosine of the difference in angle from the incident light, as described by the Lambertian scattering formula seen in equation 6.

$$I = I_0 \cos\theta$$

Equation 5. Lambertian scattering equation, describing the light scattered off an ideal, flat surface.

Light collection directly above the composite sample results in the largest amount of signal capture by the microscope. An objective lens with a high numerical aperture is utilized; a large numerical aperture ensures the largest amount of light flux is collected by the lens. By capturing

a large amount of light scattered from the surface, with the high numerical aperture lens, it is ensured that the spectra produced as a result will also be representative of that area of the sample. In order to compare improvements in the moisture resilience of the composite to the neat HP films, HP material was dropcast onto glass slides and annealed according to literature [27], [30] to create HP films. An example of two typical samples used in the accelerated ageing study can be seen in Figure 27.

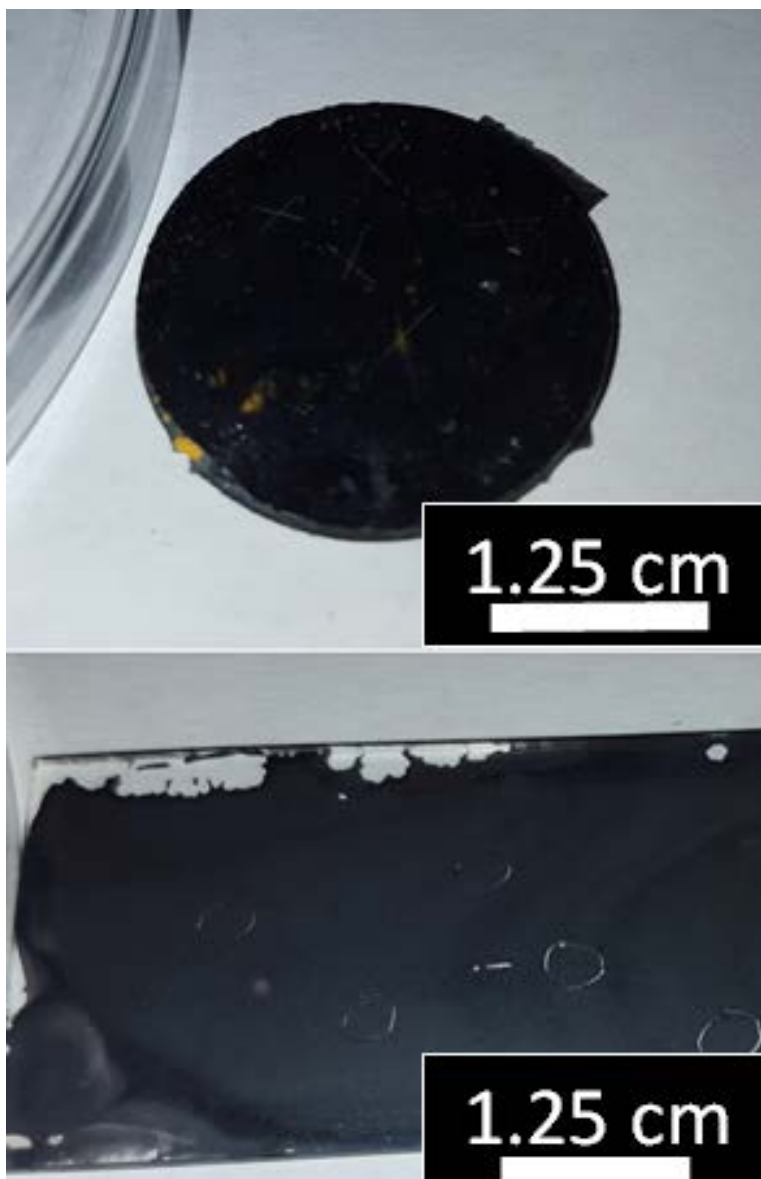


Figure 27. Samples used in the accelerated ageing study. Datum marks can be seen on both samples and were used as locations to collect consistent UV-Vis spectra for a day to day comparison during the study.

The locations were measured once daily over the course of seven days in the accelerated ageing chamber. Results are shown in Figure 28.

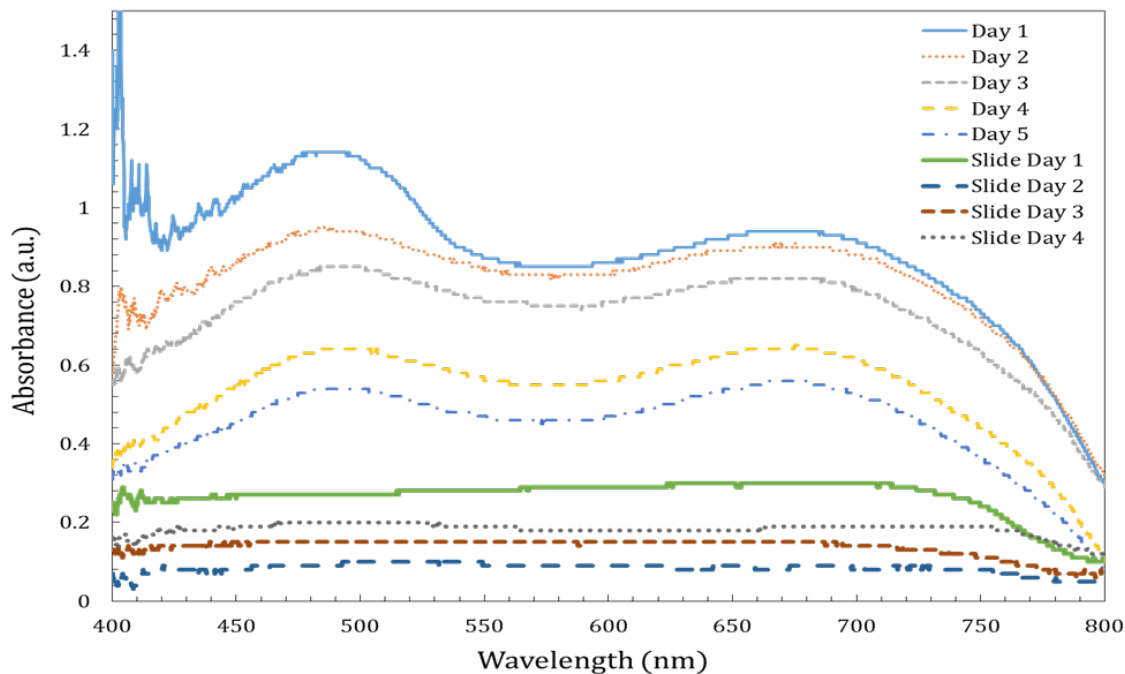


Figure 28. UV-Vis spectra of HP-polystyrene composite material compared to a neat HP film on glass (denoted as ‘slide’). The optical absorption onset can be seen at 760 nm for both the composite and the glass slide. Additionally, the PbI_2 can be seen at 530 nm in the composite spectra. Adapted from Murphy *et al.* [60].

The degradation of the HP film on the glass slide is apparent from the spectra in Figure 28.

However, the degradation of the HP polycrystalline film can also be seen visually in Figure 29.

The same field of view can be seen to degrade from multiple black grains of the $\text{CH}_3\text{NH}_3\text{PbI}_3$ HP to several yellow PbI_2 needle-like structures.

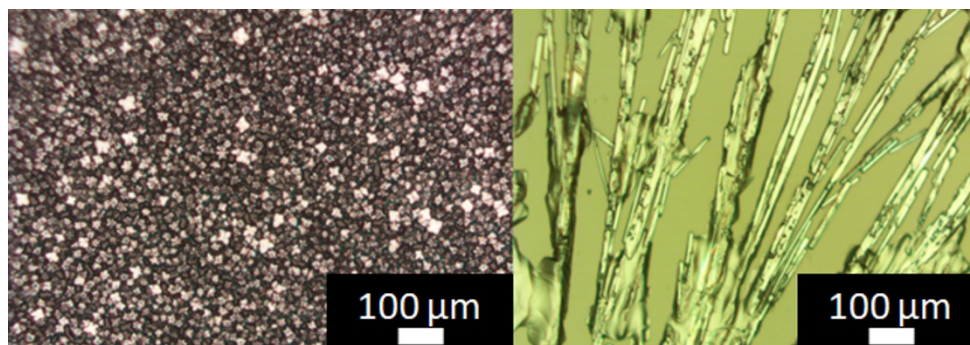


Figure 29. Optical micrographs the same field of view of a HP film deposited on a glass slide immediately after deposition (left) and after 24 hours in the humidity chamber (right). The change in the film morphology is apparent from a polycrystalline HP film to a needle-like PbI_2 film. Adapted from Murphy *et al* [60].

The abrupt degradation of the HP film observed in the accelerated ageing study is typical of HP films in high humidity ($\text{RH} \sim 90\%$) conditions [62] and even in cases where humidity levels are nearly half of the values utilized in the accelerated ageing study [72]. Resistance to moisture-driven degradation in the composite samples was also observed, as seen in Figure 30. The characteristic spectra of the composite material changes very little over the course of the study. However, the intensity of the spectra does change over the course of the study due to changes in the light scattering properties of the surface caused by precipitates. Maintaining the characteristic shape of the spectrum strongly indicates the perovskite material is still present and unchanged in the bulk of the composite material. Changes in the intensity of the absorbance spectra are likely due to changes in the surface roughness from day-to-day over the course of the study. An example of the changes to the surfaces of the samples can be seen in Figure 30.

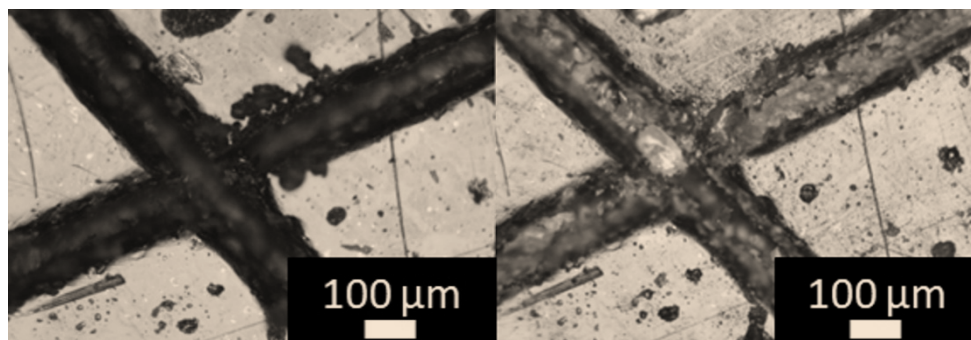


Figure 30. Optical micrograph of HP composite after molding (left) and on the last day of the study (right). White crystalline material has infiltrated the scores in the sample surface used as datum to track location. Adapted from Murphy *et al.* [60].

As the samples aged, perovskite material at the surface underwent degradation, resulting in the formation of aqueous $\text{CH}_3\text{NH}_3\text{I}$ in condensed water on the surface of the sample. Upon removal from the humidity chamber, the water evaporated leaving white crystalline $\text{CH}_3\text{NH}_3\text{I}$ on the surface of the composite sample. The white crystalline precipitate essentially added a scattering layer to the surface of the composite material reducing the overall amount of light penetration into the bulk of the composite and diminishing the intensity of the absorbance spectra over the course of the study. Degradation and re-deposition of the $\text{CH}_3\text{NH}_3\text{I}$ is believed to be a near-surface event, with little of the bulk HP actually being affected, which is supported by Figure 31.

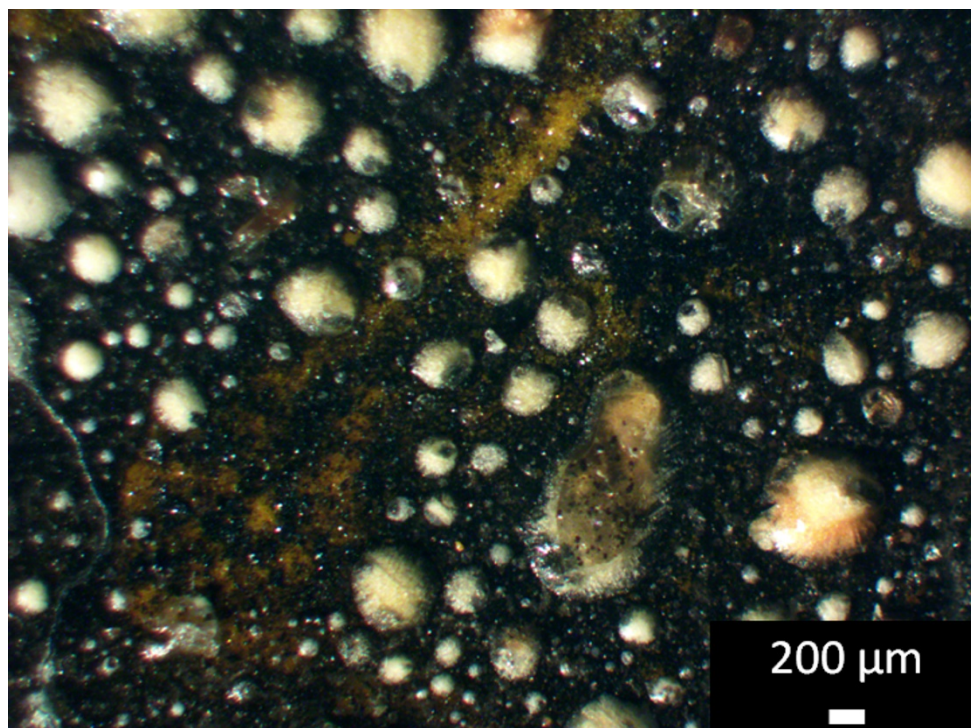


Figure 31. Optical micrograph of the surface of the composite after the completion of the accelerated ageing study. The white $\text{CH}_3\text{NH}_3\text{I}$ spots are located over degrading HP crystallites. Additionally, a large unreacted PbI_2 crystallite can be seen in the bulk of the composite. A large amount of small black crystallites seen above the PbI_2 crystallite strongly indicated that most degradation occurred at the surface of the samples.

The HP crystallites in the bulk of the composite sample are visible in the optical micrograph in Figure 31. While the surface occupying HP crystallites degraded, which is expected as they should behave similarly to the HP film on glass, the bulk of the HP crystallites in the composite survived the accelerated ageing process and remain unchanged and viable for use in optoelectronic processes.

3.2. Solution Compounding

The limitations of melt compounding became apparent through the course of the accelerated ageing study. Precursors did not fully react throughout the composite matrix, resulting in large agglomerations of PbI_2 in the composite material. In solution compounding, unreacted precursors are avoided through generation of the filler phase prior to addition to the polymeric solution, mainly due to incompatibility of solvents used in the synthesis of the HP and the creation of the polymer solutions. Dispersion of the filler phase throughout the matrix phase of the composite material is crucial to producing composites with uniform behavior and with a high degree of reproducibility. The creation of uniform composites through solution compounding is more straightforward than melt compounding as viscosity is not an issue and can be easily overcome through decreasing the concentration of the polymer in the solution. Finally, size control over the filler phase is difficult to achieve in the melt compounding as agglomerations have a tendency to form as a consequence of the heat in the polymer melt. The control over the size of the filler phase in composites allows the percolation threshold to be modulated. Typically, a shift downwards in the critical threshold for percolation is desirable as it requires less expensive filler to be used as compared to the low-cost polymeric material. Size reduction in the filler phase has been shown to decrease the necessary loading to achieve electrical percolation in other polymer systems [73], [74]. Solution compounding offers a much greater degree of control over the size of filler through utilization of ligand/surfactant chemistry during the synthesis of filler crystallites. After verification of the improved moisture resilience of the HP/PS composite through simple melt compounding, it was decided that solution compounding should be utilized in order to produce a higher quality composite material.

3.2.1. Hybrid Perovskite Filler Phase Generation

Several methods were investigated in the creation of the HP crystallite filler for loading into the composite media. Initially, HP films were solution cast onto glass, annealed, and collected by scraping material off with a blade. This technique quickly abandoned as it did not produce sufficient quantities of HP material for loading into composites. Recent developments in the generation of HP material came about during this time in the form of sonochemical synthesis of HP micro/nanocrystals and the inverse temperature crystallization of HP single crystals.

3.2.1.1. Sonochemical Synthesis

Sonochemical synthesis of HP microcrystals is a facile technique for producing large quantities of HP microcrystallites [75]–[78]. A solution of the $\text{CH}_3\text{NH}_3\text{I}$ precursor in 2-propanol and a suspension of PbI_2 in 2-propanol is created; and while the PbI_2 solution is under sonication, the $\text{CH}_3\text{NH}_3\text{I}$ solution is added dropwise. The $\text{CH}_3\text{NH}_3\text{I}$ solution is always added in excess to ensure the complete use of the PbI_2 in the suspension. As the precursors are mixed, the solution darkens, and HP crystallites are formed. Crystallites from the first attempt at synthesis can be seen in Figure 32.

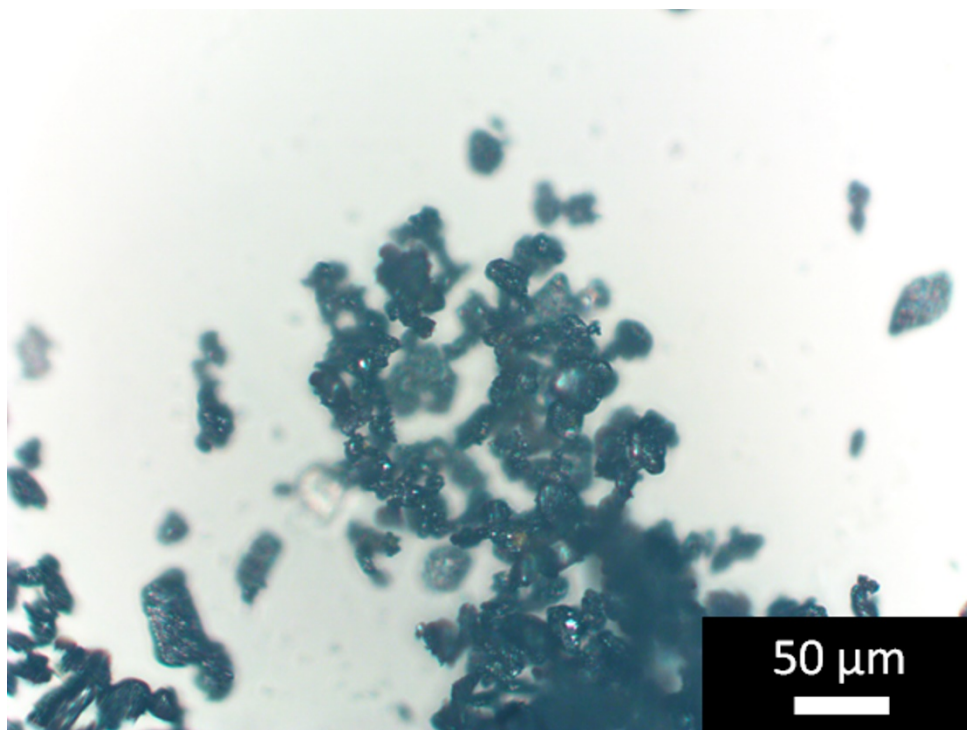


Figure 32. Optical micrograph of HP microcrystallites synthesized via sonochemical methods. The larger, non-uniformly shaped particles seen here were not ideal for the creation of the HP composite, as the shown morphology would shift the electrical conduction percolation threshold to higher concentrations for the composite media.

The HP microcrystallites in Figure 32 demonstrated that the synthesis of HP crystallites via sonochemical methods was possible and could produce quantities necessary for an in-depth study of the electrical properties of the HP composite material. Additional work was done in the characterization of the initial HP microcrystalline powder. The UV-Vis spectrum of the powder in Figure 30 can be seen in Figure 33.

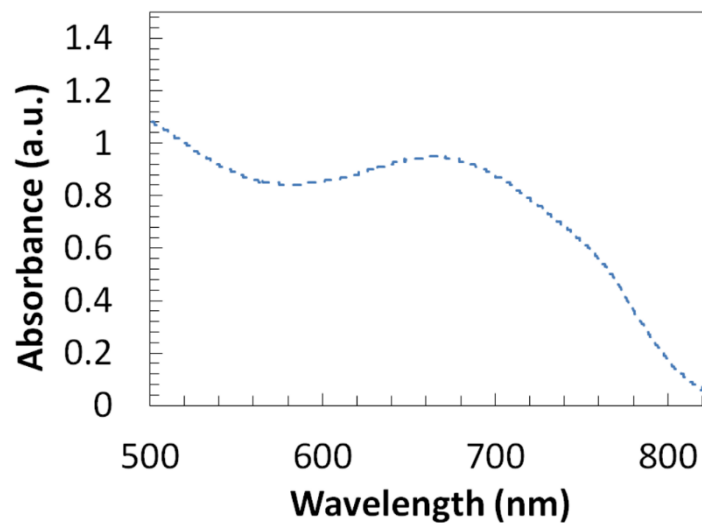


Figure 33. UV-Vis spectrum of the powder seen in Figure 32. The sharp absorption onset near 760 nm strongly indicates that $\text{CH}_3\text{NH}_3\text{PbI}_3$ is present. The increase in absorption near 530 nm also indicates the presence of some PbI_2 .

The strong optical absorption onset located at 760 nm implies that the powder in Figure 32 is indeed $\text{CH}_3\text{NH}_3\text{PbI}_3$ HP. Morphology of the powder was investigated further using SEM to assess the surface structure and minimum crystallite size. An electron micrograph of the powder from Figure 32 can be seen in Figure 34.

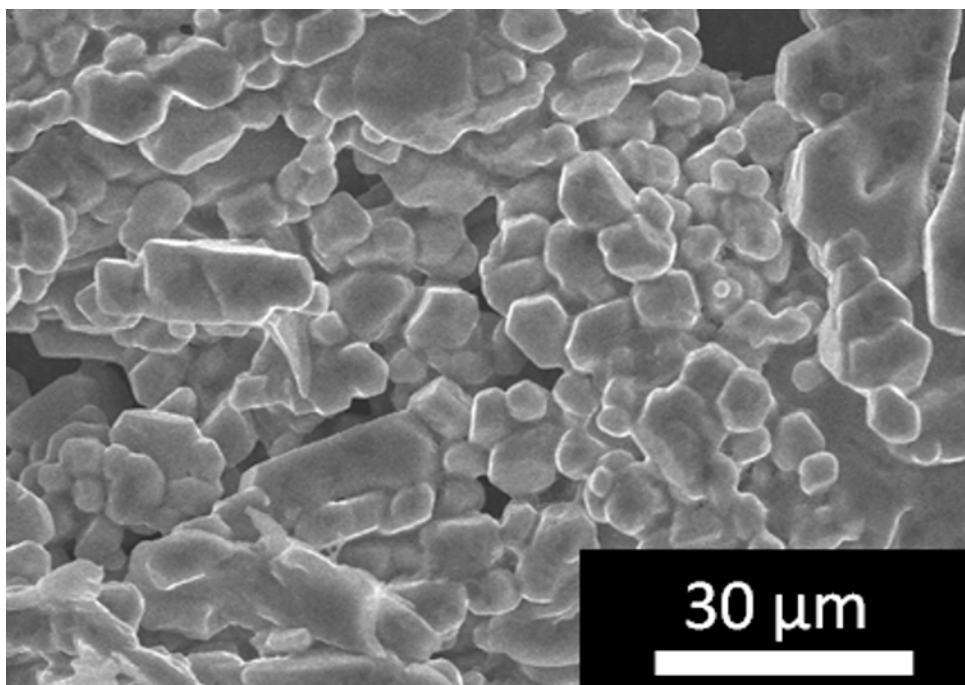


Figure 34. Electron micrograph of the HP powder seen in Figure 30. The tetragonal shape of the crystallites throughout the micrograph is indicative of the tetragonal phase of $\text{CH}_3\text{NH}_3\text{PbI}_3$.

Crystallites formed during the sonochemical synthesis process, while significantly smaller than the crystallites observed in the melt compounded composite, have not yet reached the nanoscopic scale. The UV-Vis spectrum in Figure 33 also reveals a presence of PbI_2 in the powder itself, likely at center of the crystallites. The presence of the PbI_2 in the sonochemically-synthesized HP powder was likely due to the size of the PbI_2 crystallites and due to the fact that the HP reaction is occurring at the surface of the PbI_2 crystallites, similar to the novel method outlined by Kumar *et al.* for the creation of $\text{Li}_7\text{La}_3\text{Zr}_2\text{O}_{12}$ [79] and seen schematically in Figure 35.

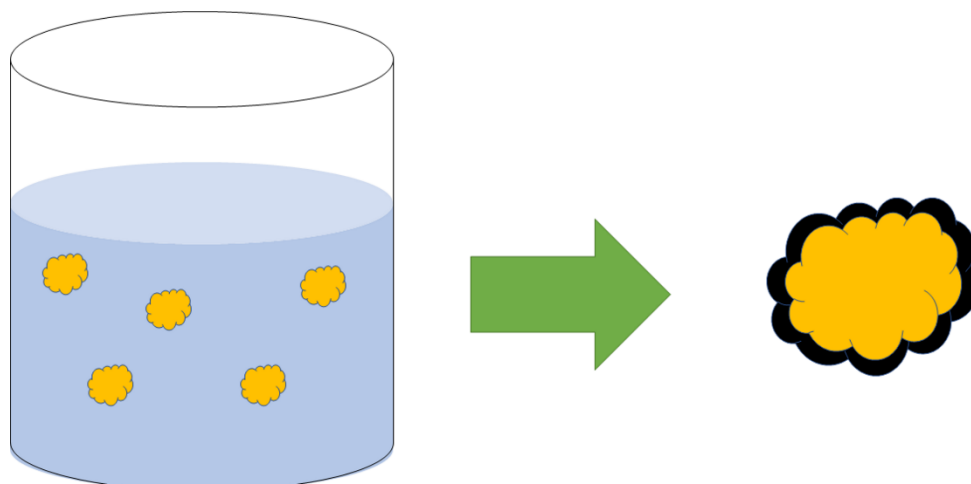


Figure 35. Schematic showing the growth of the HP phase on the surface of the PbI₂ crystallites while the core of the crystallites remains unchanged.

The schematic in Figure 35 shows the creation of the HP surface phase on the sonicated PbI₂ crystallites that was indicated by the UV-Vis spectrum in Figure 33. Further proof is seen in the EDS data collected, as shown in Figure 36.

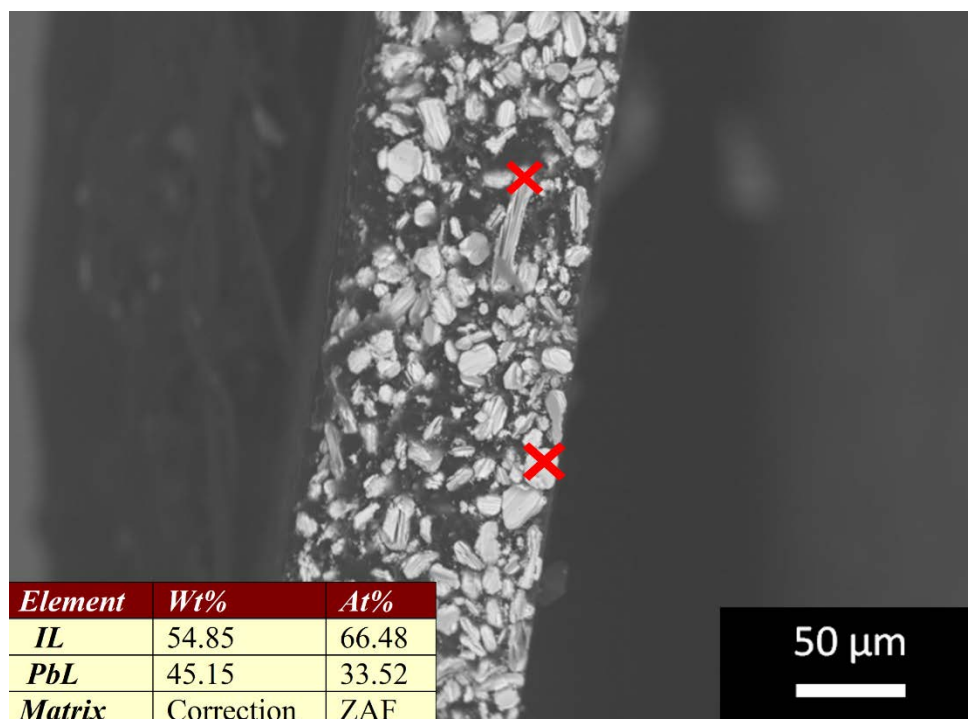


Figure 36. Electron micrograph of a cross section of the HP composite made using sonochemically synthesized HP crystallites. The red crosses indicate areas where EDS analysis was performed. Inset EDS data from the higher red cross.

The electron micrograph and accompanying EDS data in Figure 36 further validates the hypothesis that the HP is formed only on the surface of the PbI_2 crystallites in the sonication vessel. Additionally, two things can be gleaned from the electron micrograph: first, the crystallite size is still in the microscopic scale and the size distribution is fairly wide; and second, the dispersion of the crystallites has been improved upon from the melt compounding method. From the initial studies, it was apparent that the chemical purity and size/size distribution of the HP crystallites was going to be an issue.

In order to address the issue of size, the time in the sonication vessel was increased. The cavitation effects in the rapid localized thermal fluctuations at work in the sonication vessel have been shown to be a viable means of size reduction [80], [81] in several crystallite systems. Residual PbI_2 in the HP filler material was an issue and was addressed in two ways: first, by

increasing the sonication time and reducing particle size, a greater number of the atoms of a material are present at the surface of the material and therefore available to react and form HPs; and second, an additional HP synthesis method, inverse temperature crystallization (ITC), was employed to create chemically pure HP single crystals.

Increasing the sonication time during the sonochemical synthesis method was adjusted first as it was the simplest of the two methods to implement and validate. The procedure for the original sonochemical synthesis was followed after the complete addition of the $\text{CH}_3\text{NH}_3\text{I}$ precursor to the sonication vessel. The mixture was sonicated further to promote size reduction in the crystallites, the effect of which can be seen in Figure 37.

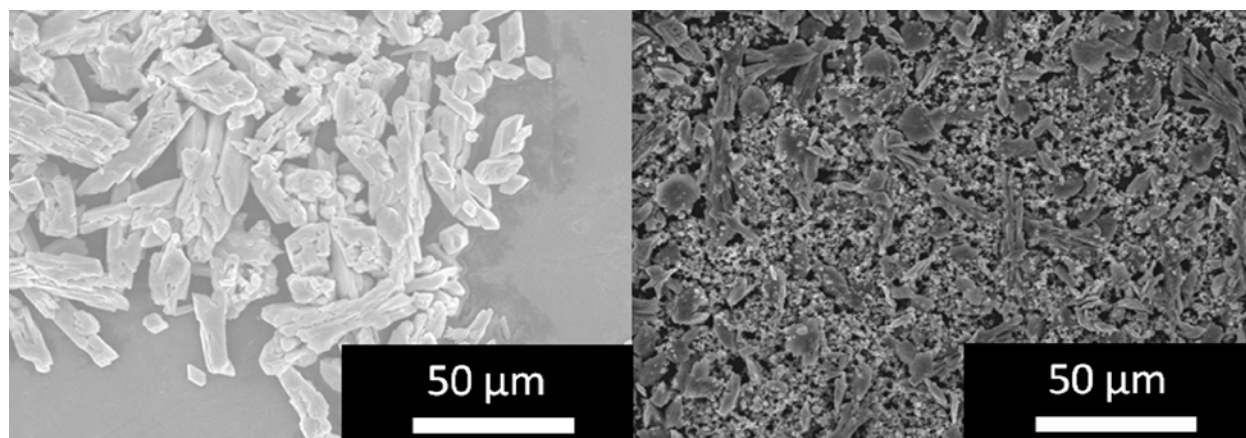


Figure 37. Electron micrographs of sonochemically synthesized HP crystallites. The effect of increased sonication time can be seen in the difference in morphologies from the 5 min sonication time (left) to the 20 min sonication time (right). The larger needle-like crystals are PbI_2 , which take on needle-like habits in IPA due to slow Ostwald ripening effect, from Murphy *et al.* [82].

As seen in Figure 37, the increased sonication time did have an impact on the overall morphology of the HP crystallites. The larger needle-like structures are the result of the IPA and the PbI_2 interacting as the PbI_2 is sparingly soluble in the IPA. The decreased solubility retards

the Ostwald ripening in the system [83] and results in non-ideal needle-like crystals. These needle-like crystals are broken down slowly as a result of the acoustic cavitation processes at work in the sonication vessel exposing the unreacted internal surfaces of the PbI_2 crystallites. The change in crystallite size is apparent in the electron micrographs, as seen in Figure 37, relatively short increases in the sonication time (5 min to 20 min) result in a large change in the particle morphology.

3.2.1.2. Inverse Temperature Crystallization

Concurrently, ITC was utilized to create chemically pure HP material for size reduction using similar sonication/cavitation methods. ITC utilizes the retrograde solubility of HPs in order to grow HP single crystals, as seen in Figure 38.

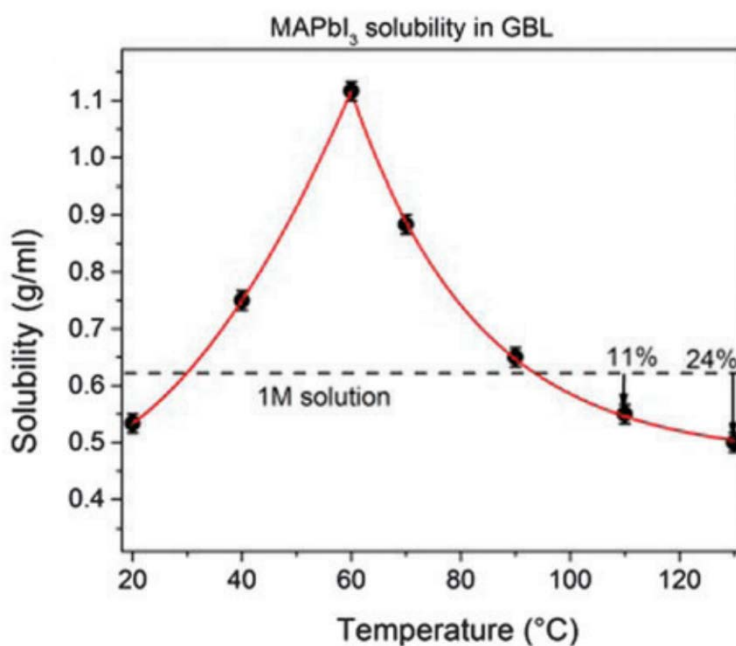


Figure 38. Solubility vs. temperature plot for the $\text{CH}_3\text{NH}_3\text{PbI}_3$ HP (denoted here as MAPbI_3). It can be seen that the 1M solution has a maximum solubility at 60 °C with steep decreases in solubility on either side of the maxima.

The $\text{CH}_3\text{NH}_3\text{PbI}_3$ HP has a maximum solubility in γ -butyrolactone (GBL) at $60\text{ }^\circ\text{C}$, above and below which the solubility drops off considerably. In order to take advantage of the retrograde solubility, the PbI_2 and $\text{CH}_3\text{NH}_3\text{I}$ precursors are added to GBL to 1M concentration and heated to $60\text{ }^\circ\text{C}$ while constantly stirred. The resultant solution was then filtered, as shown in Figure 39A, to remove contaminants and dispensed into a clean glass vial held at $110\text{ }^\circ\text{C}$. Over the course of several hours, small tetragonal-black crystals formed throughout the solution, as shown in Figure 39B and 39C, and were subsequently removed and washed with toluene.

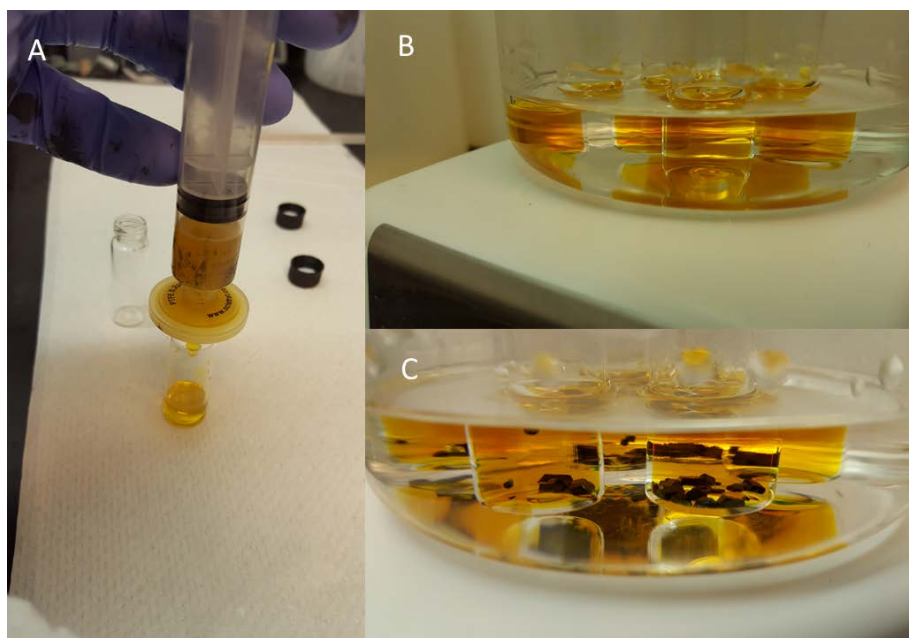


Figure 39. Inverse temperature crystallization process from filtering (A) to the mineral oil bath at $110\text{ }^\circ\text{C}$ (B & C) where HP single crystal growth is seen. The HP single crystals could then be harvested for use in composite media.

The HP single crystals grown via ITC were then pulverized via mortar and pestle, Figure 40, to allow the powder to be more easily suspended and sonicated.



Figure 40. Average quantity of $\text{CH}_3\text{NH}_3\text{PbI}_3$ single crystals produced from a 10 mL batch of solvent (A). The mechanical milling via mortar and pestle of the single crystals into a powder for further processing (B & C).

The HP powder formed as a result of the mechanical milling, Figure 40C, could then be suspended in toluene and sonicated. ITC HP crystallites in suspension were sonicated for 20 min. Pulverization and sonication of the ITC crystallites can be seen in Figure 41.

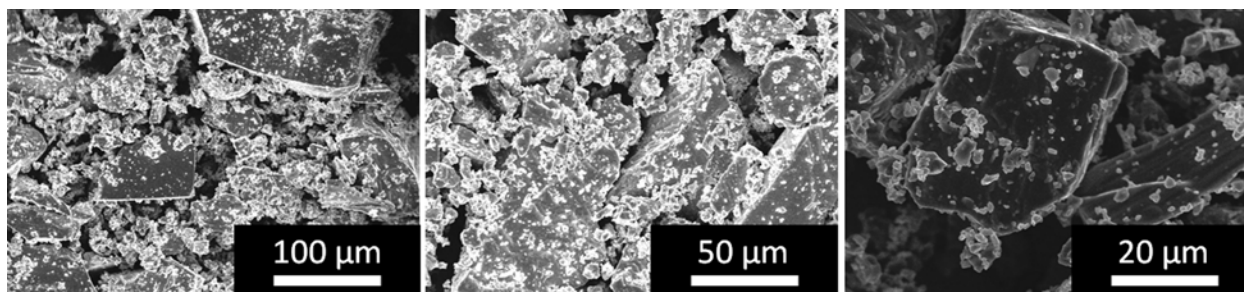


Figure 41. Electron micrographs of ITC HP after pulverization and sonication for 20 min. The smaller particulates are likely the result of cavitation-driven small mass liberation from the ITC microcrystallites, from Murphy *et al.* [82].

Size reduction of the ITC crystallites was successful, as seen in Figure 41, and the chemical purity of the ITC crystallites is as high as is achievable from any solution-based chemical synthesis method. However, two fundamental issues presented themselves when ITC was being considered as the means by which to synthesize the bulk HP filler material: (1) the control over the size of the crystallites is principally and solely achieved through variation in the sonication time and energy and (2) the throughput of the ITC method is very low when considering the time involved in preparation and is therefore not amenable to scale-up.

3.2.1.3. Sonochemical vs. ITC for Filler Phase Generation

A direct comparison of the sonochemical synthesis method and the ITC method can be seen in Figure 42. While the ITC crystallites provide desired chemical purity, they do not demonstrate uniform particle morphology distribution. The sonochemically synthesized particles present exactly the opposite issue, where they are chemically impure but have superior particle morphology distributions.

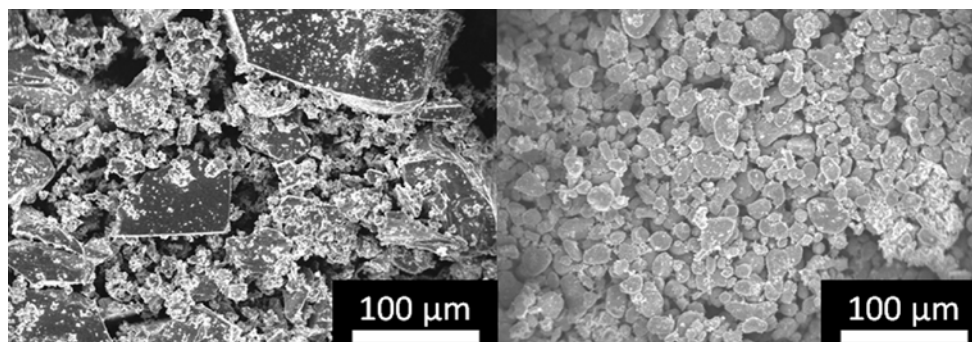


Figure 42. Electron micrographs of ITC grown (left) and sonochemically synthesized (right) HP crystallites. The ITC crystallites, while chemically pure, demonstrate a great deal of variation in morphology, whereas the sonochemical crystallites demonstrate fairly uniform size distribution but lack chemical purity, from Murphy *et al.* [82].

The issues with each filler phase generation method needed to be addressed prior to large batch synthesis for solution compounding. ITC grown crystallites required a greater degree of control over the size and shape of crystallites and suffered from low throughput and use of non-benign solvents (GBL). Addressing the issue of the chemical purity of the sonochemically synthesized particles was a simple matter of altering the physical state of the PbI_2 precursor prior to synthesis. If the size of the PbI_2 precursor crystallites was reduced prior to sonochemical synthesis, a greater amount of the initial material would be involved in the HP reaction; and if sonication time was maintained, size reduction of the final HP filler phase media would be achieved. Therefore, it was decided that a pretreatment of the PbI_2 precursor would provide adequate size reduction to make the sonochemical method viable for large batch production of filler phase media.

3.2.1.4. Solvent/Anti-Solvent Reprecipitation of PbI_2

In order to reduce the size of the PbI_2 precursor crystallites, a simple solvent/anti-solvent reprecipitation method was utilized to modify the size of the as received PbI_2 precursor crystallites. Solvent/anti-solvent precipitation has been utilized across many fields but sees heavy use in the production of micro/nanoscale drug particles [84]–[86] where monodisperse particles with similar morphology are vital in reproducible drug release/dissolution. The solvent/anti-solvent reprecipitation technique is also highly-scalable and is capable of continuous operation [87].

The solvent/antisolvent pretreatment of the PbI_2 precursor was initially carried out by dissolution of PbI_2 in N,N-dimethylformamide (DMF) and dropwise addition of the DMF/ PbI_2 solution into a substantially larger volume (1:10 by volume) of vigorously stirred IPA in an ice bath. A larger volume of the anti-solvent and cold temperatures was necessary to prevent Ostwald ripening in the precipitated PbI_2 crystallites. Upon addition of the DMF solution to the IPA anti-solvent solution, a yellow precipitate was immediately observed. The solvent/anti-solvent mixture was then centrifuged and washed with cold anti-solvent to remove residual DMF. Morphology of the resultant PbI_2 suspensions was then characterized using SEM, as seen in Figure 43. Large needle-like crystals were the result of the first attempt at the reprecipitation of the PbI_2 precursor. Crystals seen in Figure 41 are on the same size scale, or larger, than the crystals that were observed in the initial sonochemical synthesis trial. The likely cause of the large needle-like crystals grown in the solvent/anti-solvent reprecipitation is a result of the coordinating effects of the DMF solvent. When in solution the PbI_2 and DMF interact and form semi-ordered structures.

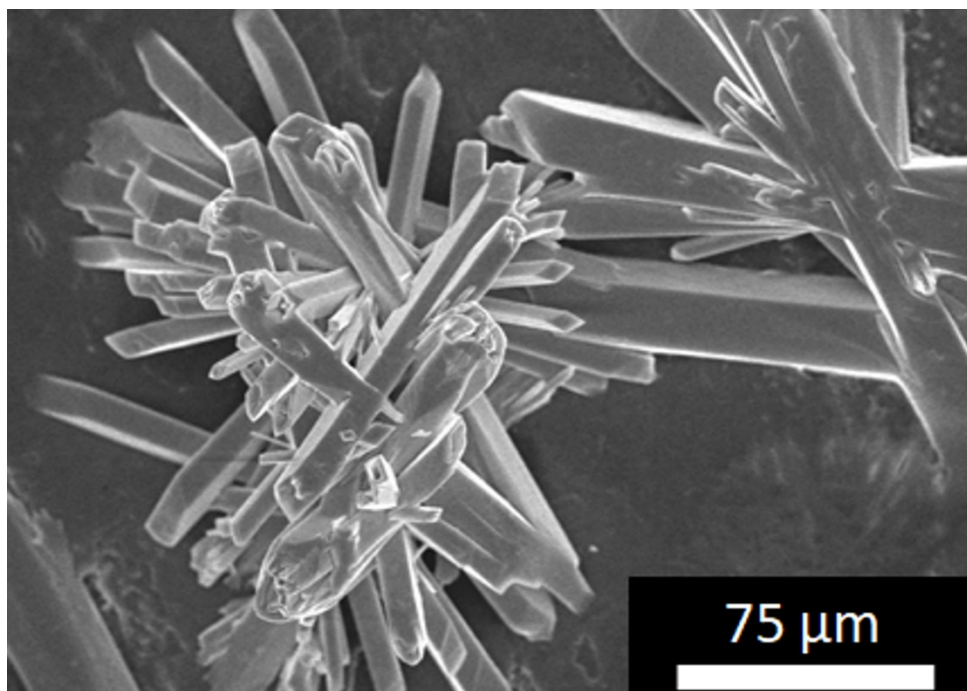


Figure 43. Electron micrograph of PbI_2 crystals produced from the initial solvent/anti-solvent reprecipitation technique. Needle-like crystal habits are observed in the resultant PbI_2 crystals. Crystals produced from simple solvent/anti-solvent methods were too large for the sonochemical synthesis procedure.

The PbI_2 upon dissolution forms octahedra with PbI_6^{4-} composition, as seen in Figure 44. When in solution with DMF, the solvent coordinates to the octahedra in a coordination ratio of 1:1 [88].

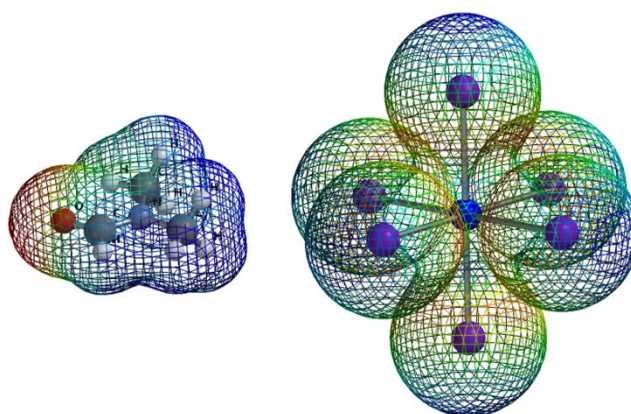


Figure 44. Electropotential maps of DMF (left) and PbI_6^{4-} produced in Spartan Chemistry [89]. The long range of the PbI_6^{4-} octahedra needed to be interrupted to produce precipitates of smaller size.

As the coordinated solution is added dropwise to the anti-solvent solution, the DMF coordinated to the octahedra is replaced slowly by the IPA, resulting in the growth of crystals on the order of tens of microns, as seen in Figure 43. The slow, solvent-coordination-facilitated growth of the PbI_2 is further supported by the electron micrograph in Figure 45.

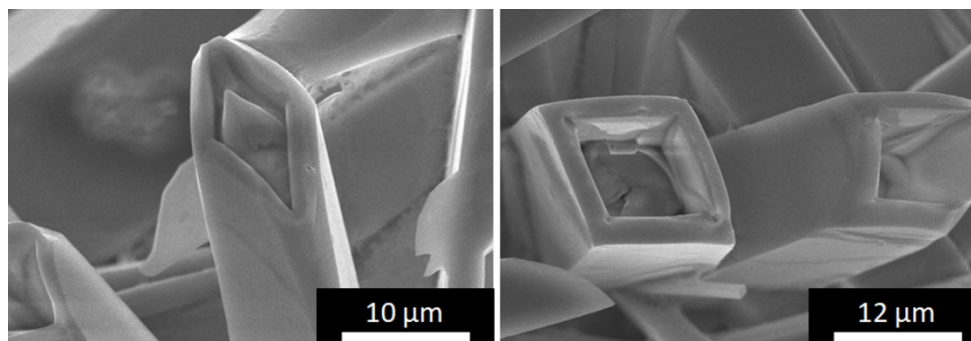


Figure 45. Electron micrographs of the terminal end of the PbI_2 crystal growth in solvent/anti-solvent reprecipitation. The exterior of the PbI_2 acicular crystals grow first, followed by the center. Crystal growth occurs rapidly but was not completed in these micrographs.

Figure 45 shows that PbI_2 crystals had time to grow into typical crystal habits, which is likely due to the coordination effects of the solvent on the PbI_6^{4-} octahedra in the solution prior to precipitation. In order to produce PbI_2 precursor crystallites of sufficiently small size, the coordination effects of the solvent needed to be mitigated or interrupted.

3.2.1.5. Ligand-assisted Solvent/Anti-solvent Reprecipitation of PbI_2

The coordination effects of solvents are a common issue in the wet-chemical synthesis of many nanomaterials [90], [91], often resulting in the undesirable growth of materials beyond the size scale necessary for quantum confinement effects. Commonly, ligands or surfactants are used to arrest the growth of the desired material. In the case of HPs, often long-chain amines are utilized to arrest crystal growth when short-order nanomaterials are being synthesized [91]–[94]. Often octylamine is used as the long-chain amine of choice for two reasons: (1) the cost of

octylamine is fairly low and therefore amendable to scale-up and (2) the carbon chain is long enough to interrupt crystal growth but short enough to allow for energy transfer out of excited nanomaterials.

Octylamine interacts with PbI_6^{4-} octahedra in a manner similar to the interaction methylamine gas has on solid HP materials [64]. The amine terminal end of the carbon chain occupies the corner of the PbI_6^{4-} that in the HP solid forms the interstitial occupied by the methylammonium group. In the DMF solution the octylamine interrupts any long-range order facilitated by the solvent coordination and remains weakly attracted to the PbI_2 precipitates in the anti-solvent. A relatively small quantity of octylamine is all that was necessary to interrupt the growth of the PbI_2 crystals, as seen in Figure 46.

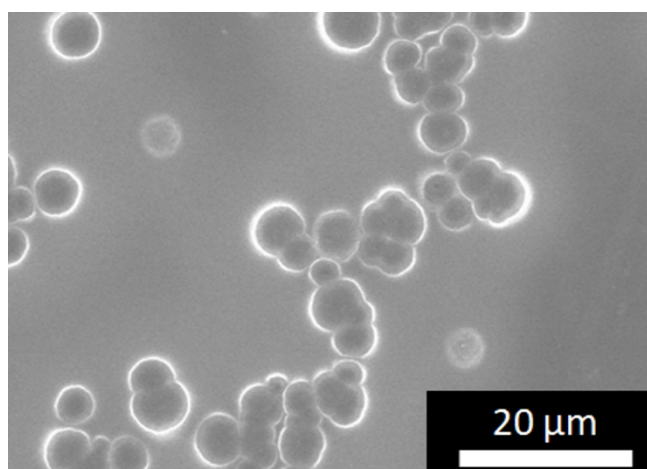


Figure 46. Electron micrograph of PbI_2 precipitants formed after the addition of octylamine to the DMF/ PbI_2 solution prior to reprecipitation. The octylamine interrupted the coordination of the PbI_6^{4-} octahedra resulting smaller precipitates.

The electron micrograph shows that the addition of octylamine to the DMF/ PbI_2 solution resulted in the creation of small spherical PbI_2 precursor crystallites and successfully interrupted the crystal growth seen in previous solvent/anti-solvent reprecipitation attempts.

3.2.2. Composite Generation

After the PbI_2 was successfully pretreated to reduce the precursor crystallite size, a large batch of HP filler phase media was generated. A 10 mL solution of 1M PbI_2 in DMF with octylamine (20 $\mu\text{L}/\text{mL}$) was added to 100 mL of vigorously stirred IPA in an ice bath. The resultant solution was centrifuged at 4000 rpm for 10 min, and the supernatant was poured off and the solids washed with IPA. This procedure was repeated twice. After the last centrifuge/wash cycle, a solid mass of PbI_2 crystallites was obtained and dried overnight in a vacuum oven for long term storage. For the synthesis of HP crystallite filler phase media, the PbI_2 powder was resuspended in IPA, and 10 mL of 1.5M $\text{CH}_3\text{NH}_3\text{I}$ in IPA was added to the suspension under sonication. Sonication of the $\text{PbI}_2/\text{CH}_3\text{NH}_3\text{I}$ slurry was allowed to proceed for 1 hour to ensure complete reaction conversion of the precursors and to minimize crystallite size. An electron micrograph of the resultant HP crystallite filler phase can be seen in Figure 45. The size of the HP filler phase was decreased considerably from the initial attempt at sonochemical synthesis, and filler phase was ready for incorporation into the composite media.

In order to create the composite, a polymeric solution of 30 wt% PS in toluene was created. Toluene was selected as the solvent in the creation of the composite as it is an orthogonal solvent for the HP/PS system. Toluene completely solvated the PS but had no effect on the HP crystallites and therefore allowed a lengthy dispersion process to ensure homogeneity in the composite precursor solution. HP filler phase was loaded into a sonication vessel and sonicated in toluene until it appeared well-dispersed to the unaided eye.

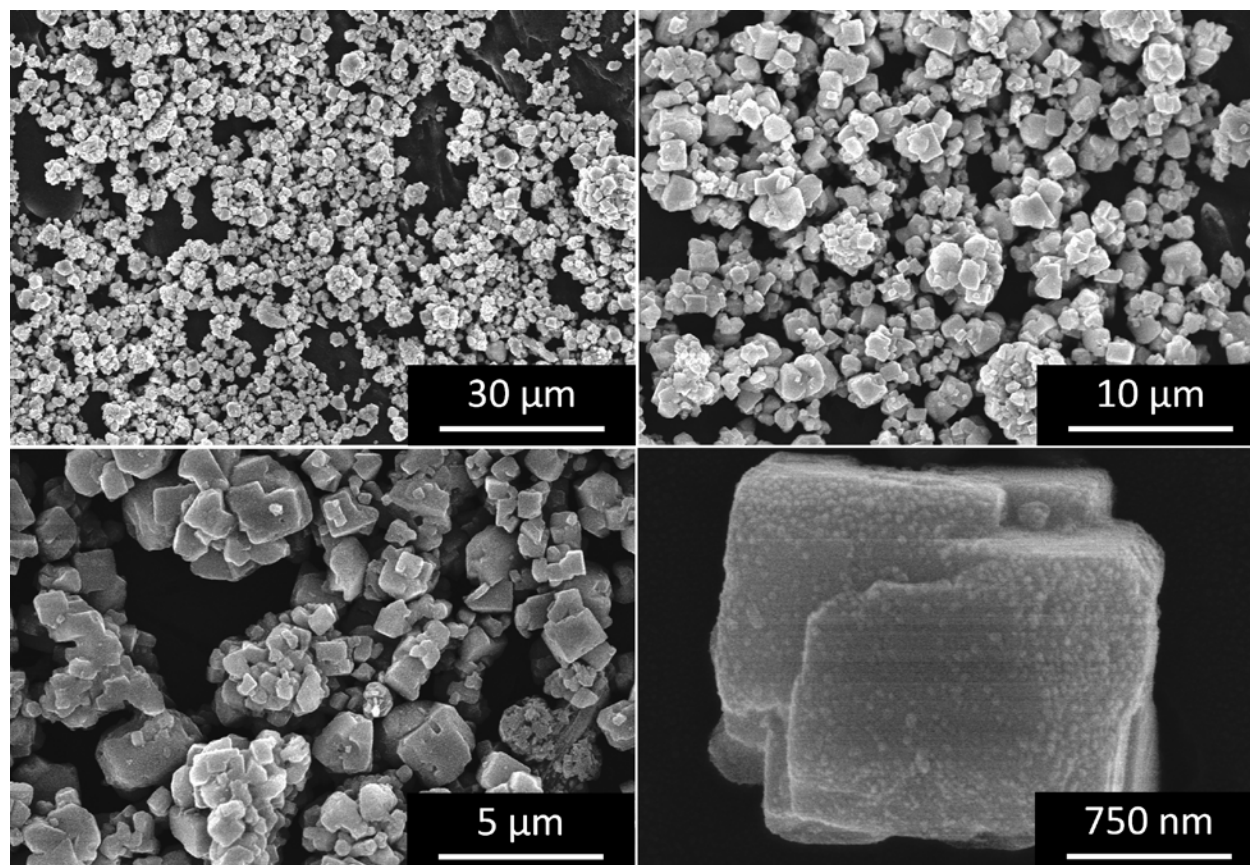


Figure 47. Electron micrographs of the HP crystalline filler phase material synthesized using the ligand-assisted solvent/anti-solvent reprecipitation method. Particle size has been considerably reduced, and the size and shape of particles are fairly uniform throughout the large batch synthesis.

The suspension of HP microcrystals were then added to the PS solution under vigorous stirring. After the addition of the HP microcrystals to the PS solution the mixture was sonicated to ensure consistent dispersion. Composite precursor solution could then be dropcast onto target substrates for electrical testing.

3.2.3. Composite Characterization

The HP composite media was first developed to mitigate the issue of moisture-driven degradation. However, while the compounding demonstrated success as a means to improve the moisture resistance of the HP filler phase media, the potential of the composite as a solar energy harvester is negligible if charge carriers cannot be extracted from the HP filler with a reasonable degree of efficiency. Various weight loadings of HP filler phase were incorporated into the composite precursor solution and dropcast onto glass slides for electrical testing, as seen in Figure 48.



Figure 48. Typical dropcast HP/polystyrene composite samples of various loadings (60-75wt%). Samples were dried, removed and their dimensions measured for electrical characterization.

The black color of the composite is consistent with that observed in previous melt compounded composite samples. Composite samples were interrogated using UV-Vis spectroscopy to assess the quality of the filler phase material present compared to that of both the initial sonochemically

synthesized crystallites and crystallites from the same source as found in the composite, as seen in Figure 47.

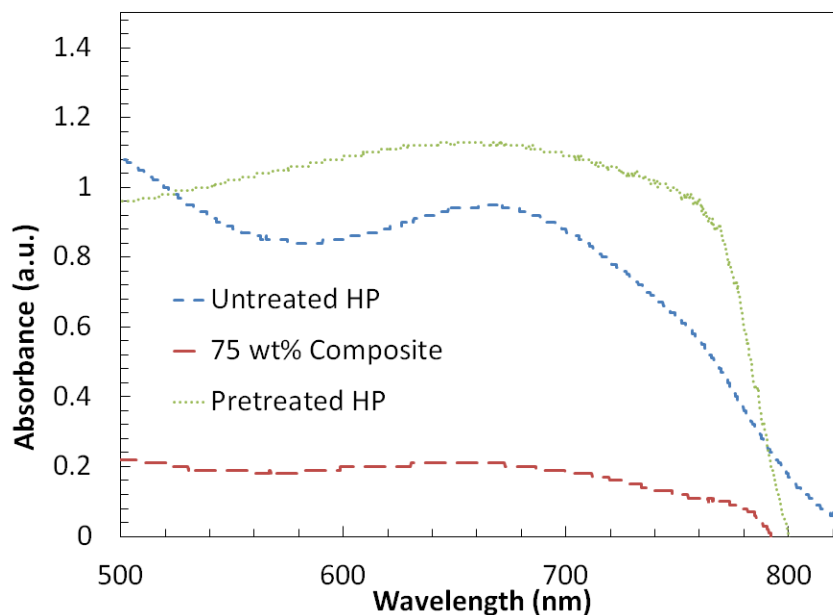


Figure 49. UV-Vis spectra of the initial sonochemically synthesized HP filler phase (Untreated HP), HP filler sonochemically synthesized from octylamine treated PbI_2 precursor (Pretreated HP), and a composite created from the pretreated HP filler phase material (75 wt% Composite). The spectrum of the composite matches the characteristic shape of the pretreated material and lacks the increase in the 530 nm range indicating very little PbI_2 is present.

The spectra in Figure 49 show that the filler media present in the composite demonstrates the same chemical purity as the HP filler phase media prior to addition to the PS solution and has little to no unreacted PbI_2 precursor. In order to further verify the purity of the HP filler phase in the composite, X-ray diffraction (XRD) was used to compare the chemical purity of the HP in the composite to that of an ITC grown single crystal, as seen in Figure 50.

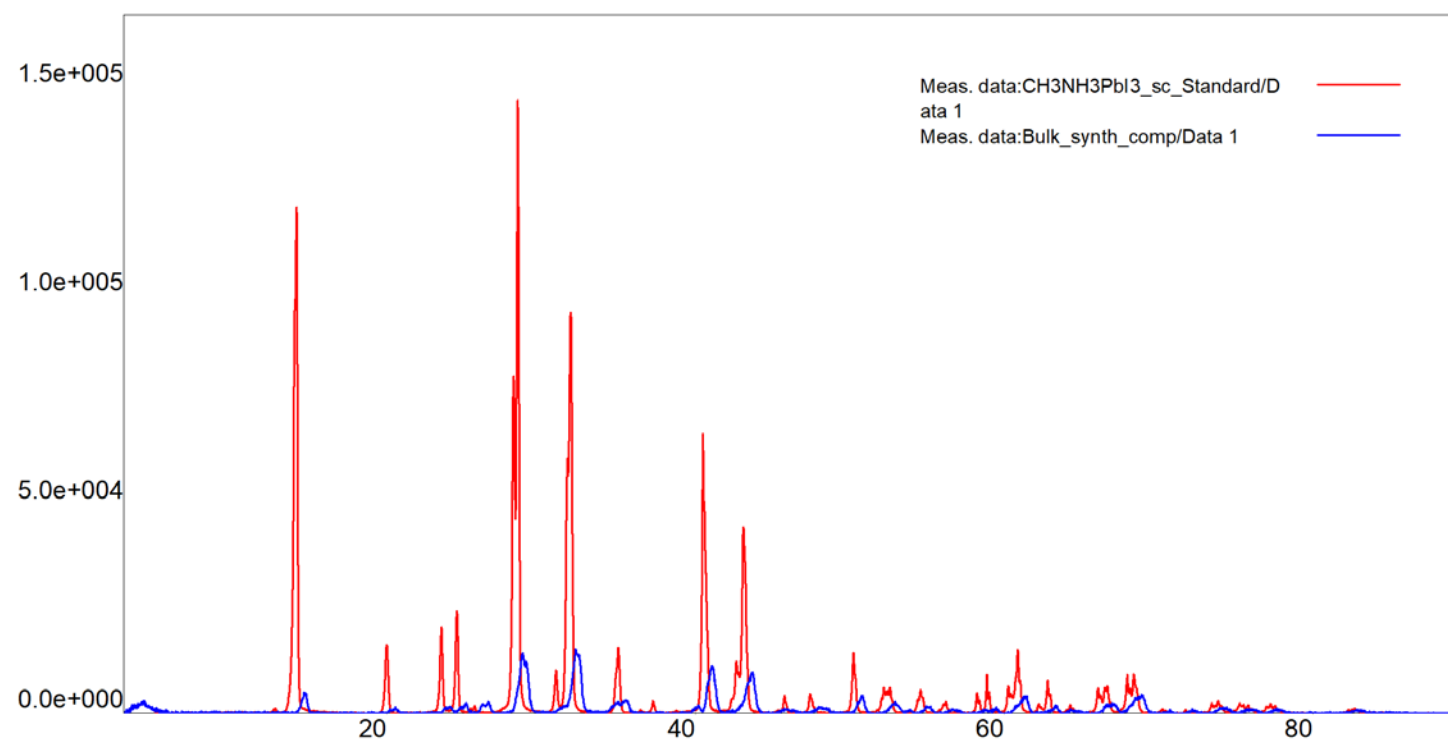


Figure 50. X-Ray diffractogram of a HP composite sample (Bulk_synth_comp) as compared to that of a chemically pure ITC grown single crystal. The broadening and magnitude reduction are a consequence of the small particle size and dispersion [95] and right-shifted peaks are typical of composite materials, from Murphy *et al.* [82].

The diffractogram in Figure 50 shows the chemical purity of the HP filler phase media present in the composite is on par with the purity of a single crystal grown using the ITC method previously described.

Composite samples were then cross-sectioned and imaged using SEM to assess the morphology and dispersion of the HP filler phase crystallites, as shown in Figure 51.

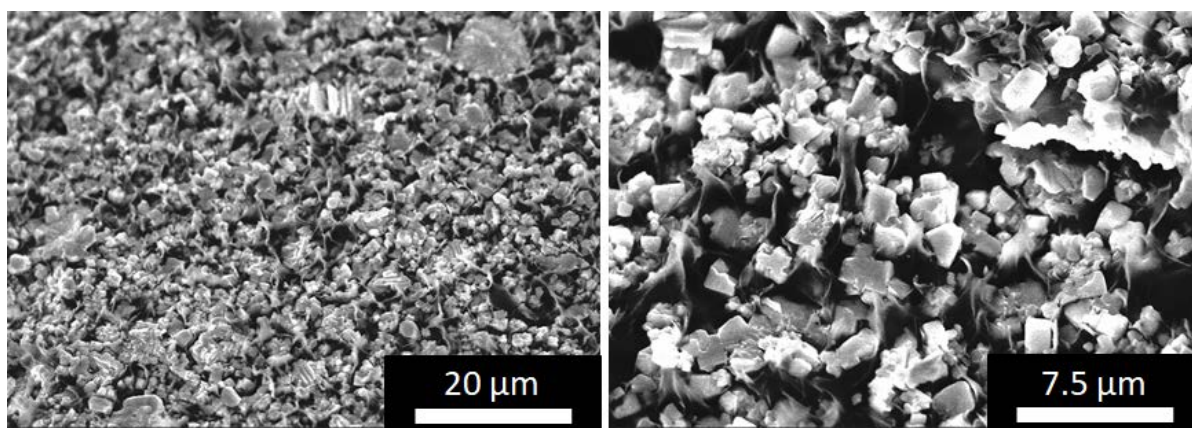


Figure 51. Electron micrograph cross-section of a 75 wt% HP composite sample. Cubic HP crystallites are visible throughout the composite sample, demonstrating a high degree of dispersion in the dropcast composite sample. From Murphy *et al.* [82]

A well dispersed filler phase is crucial to lowering the percolation threshold for electrical conduction in composites [96]–[98]. The higher degree of dispersion can be seen in the electron micrographs in Figure 51 with no large clustering of HP crystallites throughout the composite cross-sections. Dispersion of a filler phase in a matrix phase can be predicted through the surface energy at the interface between the filler phase and the matrix phase. In the case of the HP/PS composite, uniform dispersion of the HP filler phase in the PS solution was verified through contact angle measurements between a flattened pile of the HP filler phase powder and a droplet of the 30 wt% PS in toluene solution, as seen in Figure 52.

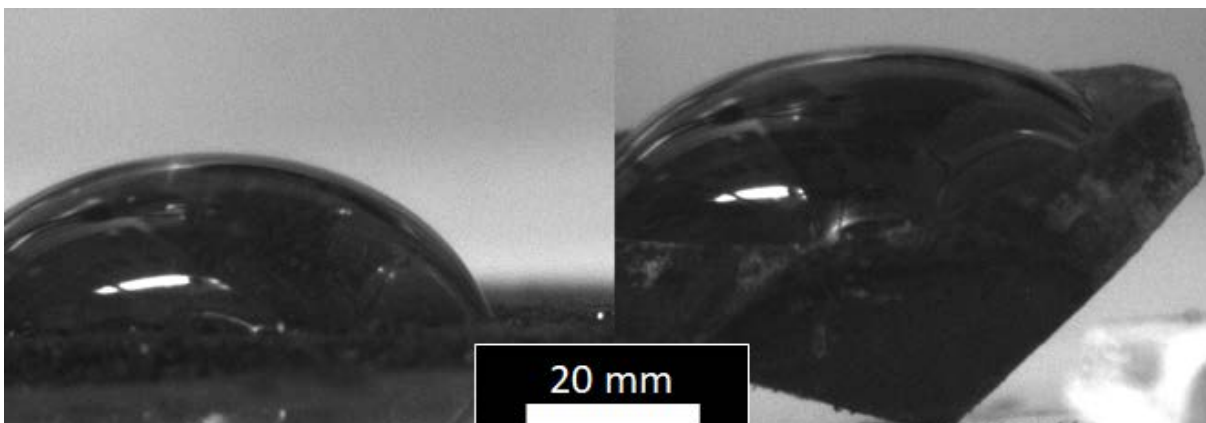


Figure 52. Optical micrographs of the interaction between a droplet of 30 wt% polystyrene in toluene and a film of HP powder (left) and a HP single crystal (right). The average contact angle of droplets with the powder film was 60° , indicating a relatively low interfacial energy between the HP and the polymeric solution.

The average contact angle measured between PS solution was 60° , which indicated that the interface between the powder and the polymer solution is relatively low energy. A low energy interface implies that very little agglomeration of the filler phase is occurring in the composite precursor solution and therefore the composite itself, as shown in Figure 51.

3.2.3.1. Determining the Percolation Threshold for Electrical Conduction

The percolation for electrical conduction in the HP/PS composite was determined empirically through collection of current-voltage (IV) sweeps of the composite material. Composite samples of various weight loadings were dropcast and allowed to dry on glass slides. After drying, the circular composite disks, as seen in Figure 48, were measured to determine the area and thickness of the composite samples. The samples were then affixed into an electrical testing configuration. A schematic of the testing configuration can be seen in Figure 53.

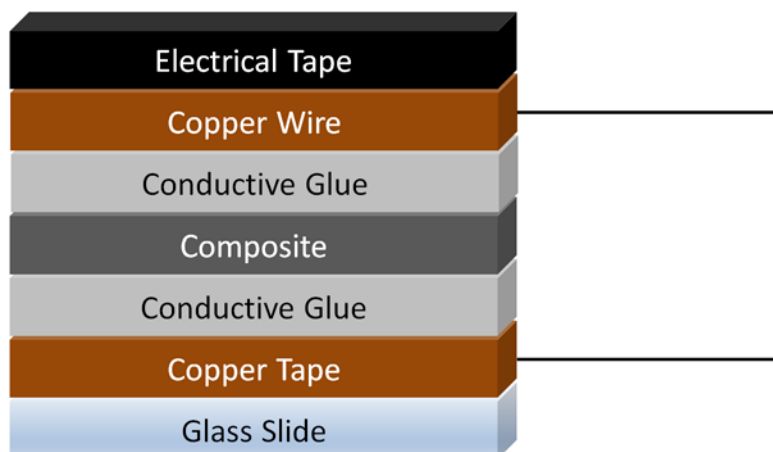


Figure 53. Schematic of the testing configuration for the composite disks. A two-wire configuration was used as the contact resistance was negligible given the high resistance of the composite.

Samples were affixed to conductive copper tape and a coil of copper wire on either side with conductive silver paste, and the entire stack was held in place with a large piece of electrical tape. The tape acted to both applied downward pressure while the silver paste dried and to block light from hitting the composite, thereby increasing/decreasing the conductivity of the photoactive semiconducting HP.

After the samples were fully dried in the testing stacks, IV sweeps were performed using a Keithley 2450 source-measure meter. For each weight loading, four composite samples were dropcast and dried for electrical characterization. Each individual composite sample was scanned four times, and the resultant 16 IV profiles were averaged to produce IV data for each weight loading. The processed IV sweep data can be seen in Figure 54 on the next page. Composite samples below the critical threshold for electrical conduction demonstrated a capacitive-like behavior. Observed as charging on the sample after a IV sweep was complete, which would result in the next IV sweep initiating at a higher starting voltage. It was necessary in the cases of the 10 wt% - 70 wt% composites to discharge the composite sample prior to additional IV

sweeps due to the ability of the material to hold charge. However, after loading the composite to 75 wt%, the percolation threshold for electrical conduction was reached, and the composite began to demonstrate resistive-like ohmic behavior. The linear portions of the IV sweeps for the lower weight loadings (10 wt% - 70 wt%) were used to calculate the respective resistance values for those loadings for resistivity calculations. Resistivity of the composite samples was calculated using equation 7.

$$\rho = \frac{A}{t} R$$

Equation 6. Resistivity is calculated from the area (A) and thickness (t) measured from the composite samples, and the resistance (R) was determined from the IV sweeps.

The conductivity value was then easily calculated as the inverse of the resistivity and plotted against the weight loading in Figure 55. Conductivity of the 75 wt% composite material was calculated to be $9.23 \cdot 10^{-12}$ S/cm compared to the literature value for polycrystalline $\text{CH}_3\text{NH}_3\text{PbI}_3$ of $2.63 \cdot 10^{-8}$ S/cm [99]. A four order of magnitude decrease in the conductivity of the filler phase is expected as the properties of the neat filler material are never observed in the composite. The lack of ability of the composite to achieve similar conductive behavior as the filler on its own is due to the polymer material forming a nanometer thick barrier on the external surfaces of the filler phase material.

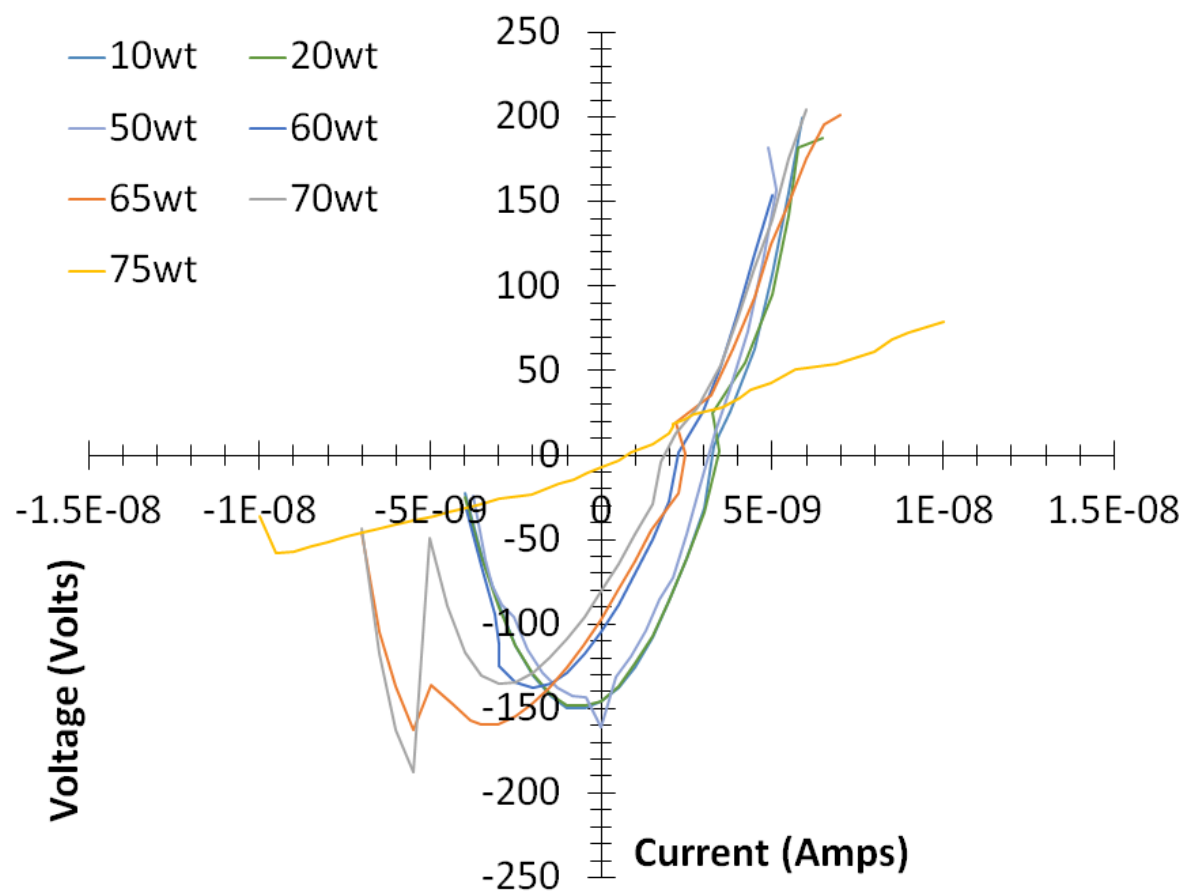


Figure 54. Averaged IV sweeps for HP loaded into polystyrene. Averages were generated from multiple sweeps across five samples to give a representative curve. Weight loadings lower than 75 wt% demonstrated a capacitive behavior and had to be discharged prior to carrying out new sweeps. Ohmic behavior was not observed until the loading of the composites had reached 75 wt%. From Murphy *et al.* [82].

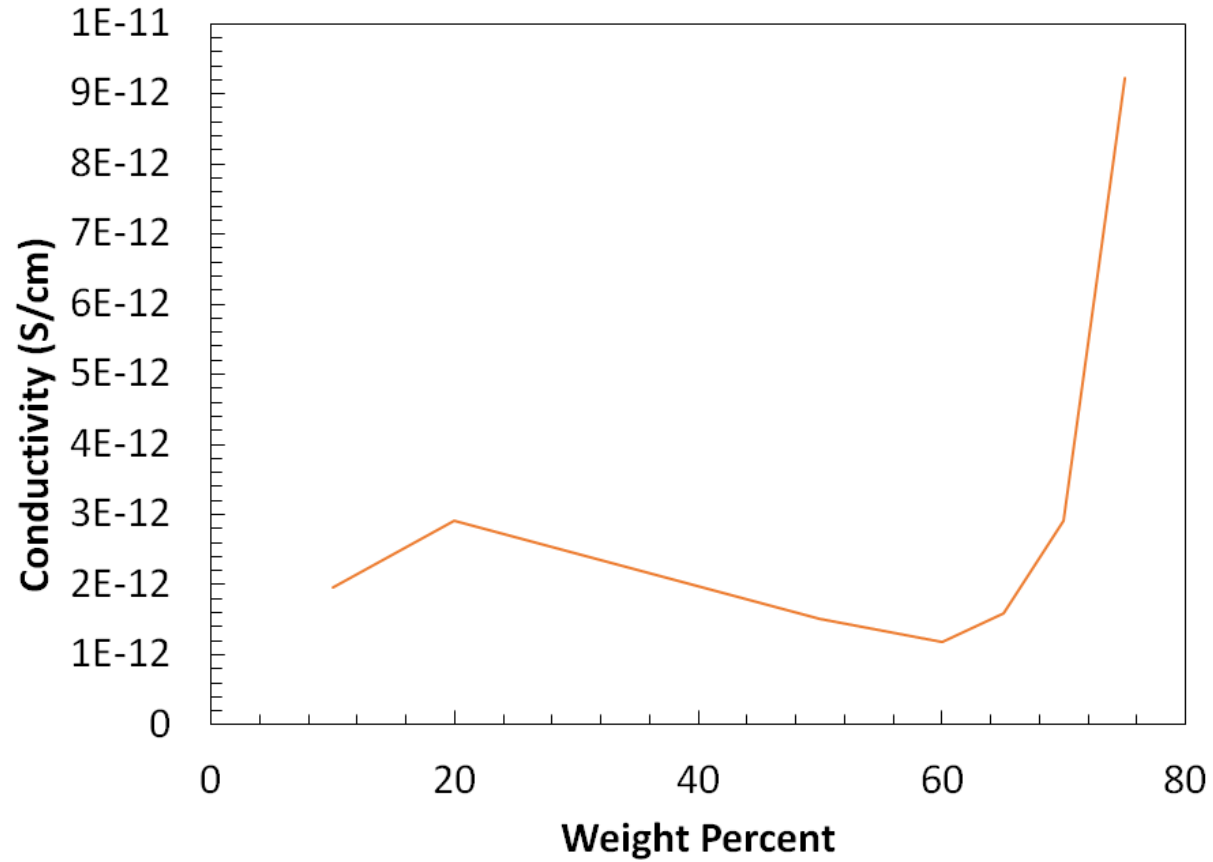


Figure 55. Plot of conductivity vs. weight % loading to illustrate the percolation threshold was reached at 75 wt%. Resistance of the composites with non-ohmic behavior were extracted from the linear portions of the IV sweeps. The rapid increase in the conduction of the composite is typical of reaching the percolation threshold in composite materials. From Murphy *et al.* [82].

4. Electrospinning Hybrid Perovskite-Polymer Micro/Nano Fibers

Compounding HP material with polymers as described previously encompasses ideal methods for the generation of feedstock material for various fabrication processes. The dropcasting of polymer melts and solutions was suitable for the characterization of the materials; however, in order to incorporate the functionalized composite material into useful devices, the composite melt/precursor solution must form functional structures. ES provides the means to fabricate micro/nanoscale fiber structures to act as functional surfaces or for incorporation into device architectures. Both melt and solution compounding were utilized in the creation of HP/PS composites and encapsulated HP.

4.1. Melt Electrospinning Composite Fibers

The previous section on melt compounding of the HP/PS composite through combination and heating of the polymer feedstock and HP precursors demonstrated both the feasibility and simplicity of creating HP/PS composites through polymer melt processing. Previous melt compounding involved the creation of a polymer melt followed by the subsequent addition of HP precursors under vigorous stirring to create the HP/PS composite media. However, the ability to stir the polymer melt is non-existent in the custom melt ES system utilized at the Montana Tech Nanotechnology Laboratory. The melt ES system consists of a heated metallic cylinder terminated at one end by a needle (spinneret), while the other end is open allowing material to be loaded and extruded through the needle by a pneumatically actuated piston when the system is at temperature.

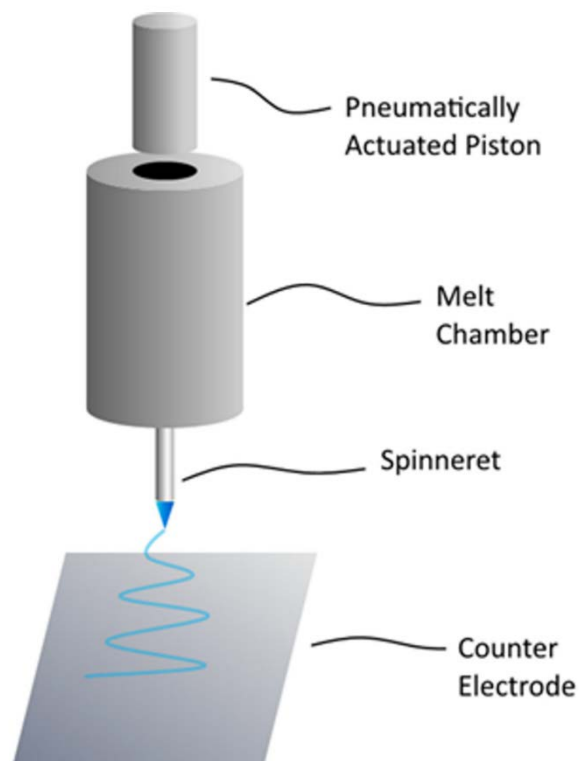


Figure 56. Schematic of the custom melt electrospinner used for the creation of HP/PS composite microfibers. The melt chamber holds the polymer melt which is extruded into the high strength electric field through actuation of the piston.

However, while the ability to stir the polymer melt was non-existent, it was hypothesized that adequate mixing of the polymer feedstock and HP precursors prior to loading into the melt chamber would allow the creation of a HP/PS composite. Mixtures of the PS and HP precursors can be seen in Figure 57. A simple mixing of the HP precursors into the polymer feedstock was sufficient to provide feedstock material to load into the melt ES system.



Figure 57. HP precursors (top), polystyrene feedstock (bottom, left), and the simple mixture (bottom, right) of all three into the melt ES feedstock material. From Murphy *et al.* [100]

In order to determine the behavior of the components of the melt ES feedstock in the melt chamber, thermogravimetric analysis (TGA) was conducted to determine when each component would decompose/sublimate. TGA analysis of the components can be seen in Figure 58. The methylammonium iodide component of the composite feedstock was expected to undergo sublimation at the lowest temperature as predicted by literature [39].

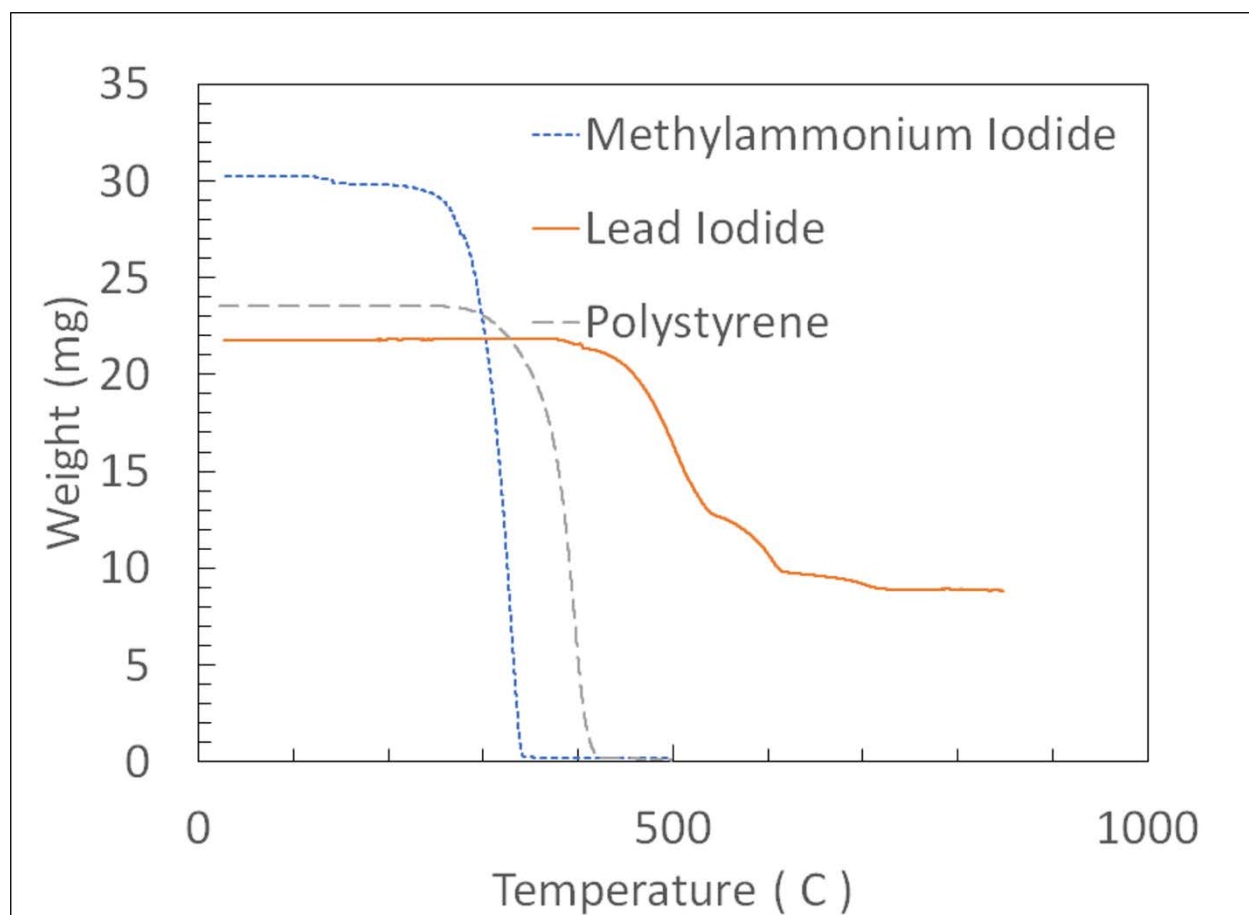


Figure 58. Thermogravimetric analysis of the components of the melt ES feedstock. The methylammonium iodide components begins to undergo mass loss at the lowest temperature of the three components at approximately 230 °C.

While the methylammonium iodide component may sublime, reaction with PbI_2 precursor crystallites is not precluded, as the melt chamber is sealed at both ends when at temperature. The needle is sealed with the melted polymer, and the feed port is sealed by the piston.

Microfibers were produced by heating the melt chamber to approximately $200\text{ }^\circ\text{C}$. The temperature is approximate as the readings are collected from the external surfaces of the heating tape used as the heat source in the melt electrospinner. It is entirely possible that temperatures in the melt chamber itself were in excess of the $200\text{ }^\circ\text{C}$ during the fabrication of microfibers.

Typical electric field strength used to electrostatic draw down the polymer melt was 4.5 kV/cm .

A fiber mat produced during the melt ES process can be seen in the optical micrograph in Figure 59.

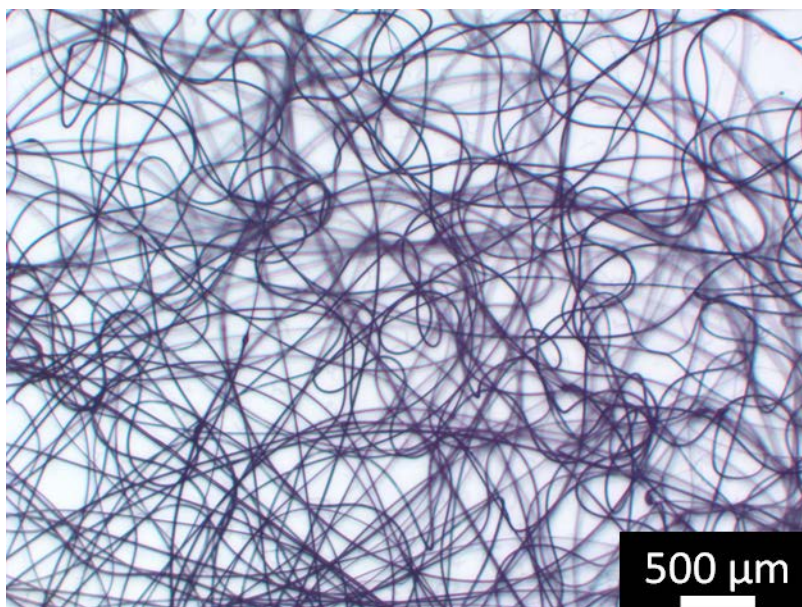


Figure 59. Optical micrograph of microfibers produced during the melt ES process. Fibers are uniform in diameter with minimal breaks or beading indicating a successful melt ES process.

Fibers collected from melt ES were investigated to determine if HP was successfully synthesized *in situ* in the melt electrospinner. In addition to the HP melt compounded fibers, two separate sets of fibers were melt ES to determine the effect, if any, the precursors have on the morphology of fibers. SEM and EDS analysis were done on these fibers, as shown in Figure 60.

<i>Element</i>	<i>Wt%</i>	<i>At%</i>	<i>Element</i>	<i>Wt%</i>	<i>At%</i>	<i>Element</i>	<i>Wt%</i>	<i>At%</i>
<i>IL</i>	99.05	99.42	<i>IL</i>	56.86	68.27	<i>IL</i>	65.76	75.82
<i>PbL</i>	00.95	00.58	<i>PbL</i>	43.14	31.73	<i>PbL</i>	34.24	24.18

Figure 60. Electron micrographs of melt electrospun fibers with accompanying elemental analysis data. The methylammonium iodide (left) fibers demonstrated irregular morphologies and the precursor phase separated from the polystyrene. The PbI_2 embedded in the fibers (center) and typically produced larger fibers with somewhat regular morphology. The HP material found in the fibers (right) demonstrated circular/spherical morphologies and were typically found in smaller diameter fibers. Adapted from Murphy *et al.* [100].

The success of the synthesis technique was further verified through XRD analysis to determine qualitatively the relative amounts of precursor chemicals and HP crystallites, as seen in Figure 61. Peaks in the PS-OHP sample in the diffractogram data verify the presence of the tetragonal phase of $\text{CH}_3\text{NH}_3\text{PbI}_3$ HP [101].

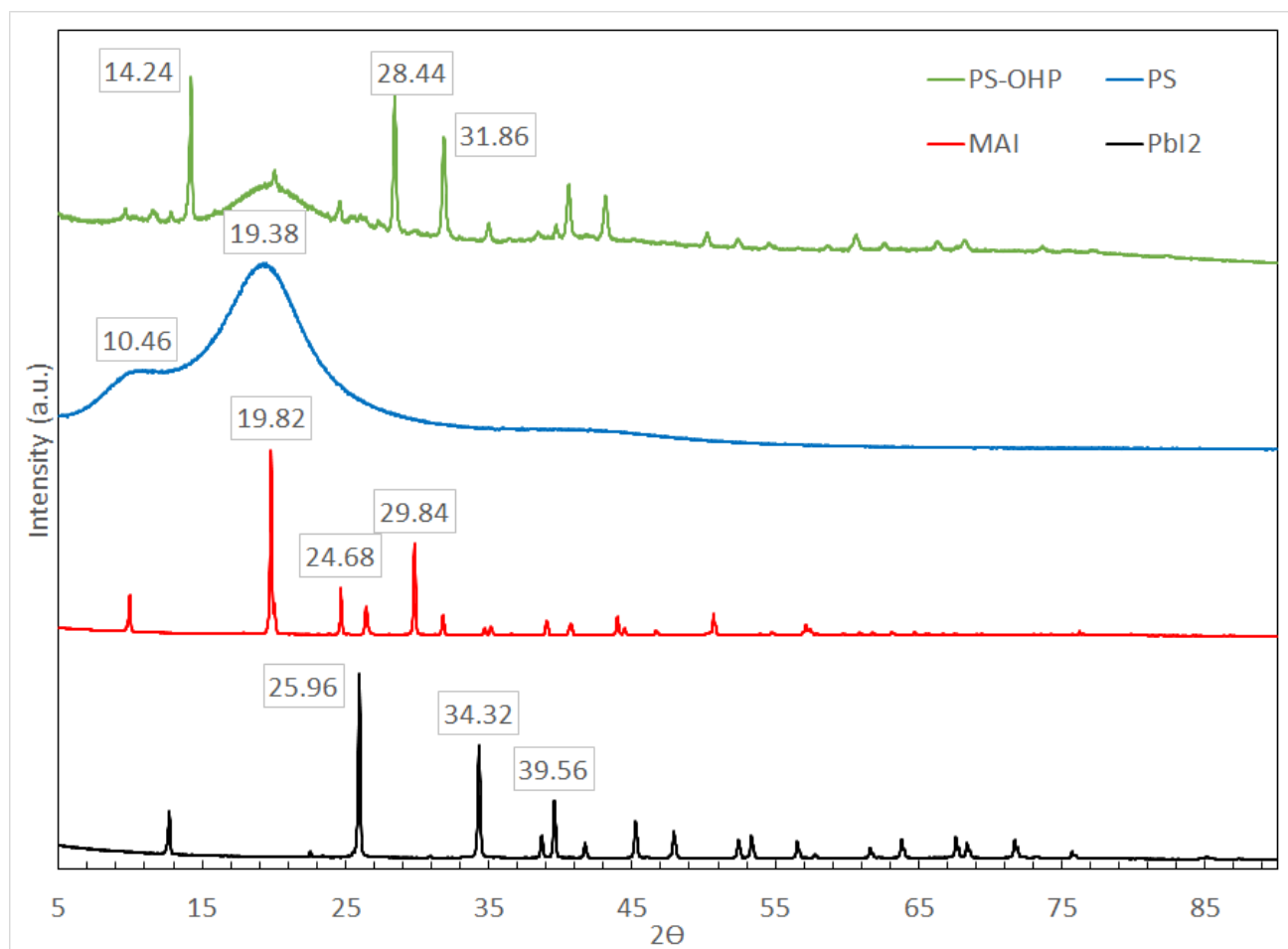


Figure 61. X-ray diffractograms of the three components of the melt ES feedstock (PS, MAI, PbI₂) and the melt electrospun fiber sample (PS-OHP). Peaks in the composite fibers demonstrate that HP material was successfully synthesized. From Murphy *et al.* [100].

Elemental and crystalline phase analysis demonstrated that the synthesis of HP/PS composite microfibers was successful. However, as with the melt compounding, issues existed with the agglomeration of PbI_2 crystallites, not only in fully reaction of the PbI_2 as was the issue in the melt compounding process but also in interrupting the ES process. In the melt ES process, the polymer melt is extruded from the melt chamber through a small needle known as the spinneret. The extruded polymer forms a small bead at the head of the spinneret. When exposed to the high strength electric field, the bead deforms, and a small jet of polymer melt is emitted from the bead. The jet is emitted in order to increase the surface area and thereby decrease the surface charge density on the polymer melt. Emission of the polymer jet from the bead is a continuous process once established, provided the flow rate of polymer melt to the bead is equal to the flow out due to the polymer jet. However, large particles extruded into the bead move towards the jet and interrupt the electrostatic elongation process as they cannot easily increase surface area to decrease the surface charge density. The charged particle is then drawn directly to the counter electrode interrupting the ES process. In the best case the particle is trapped in the fiber and only effects the localized diameter of the fiber, as seen in Figure 62.

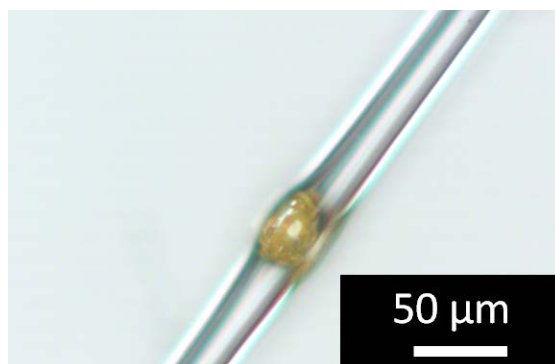


Figure 62. PbI_2 embedded in a melt electrospun polystyrene fiber. The crystallite has a localized effect on the fiber diameter but was not large enough to interrupt the melt ES process. From Murphy *et al.* [100].

The issue of the PbI_2 crystallite size in the melt ES set-up is not as easily mitigated as it was in the case of the solution compounding. When the melt chamber is brought up to temperature, the PbI_2 agglomerates regardless of the pretreatment of the PbI_2 precursor prior to loading.

Interestingly, the conversion of the PbI_2 to HP material in the melt electrospinner was more efficient at producing HP crystallites with little PbI_2 impurities, as seen in Figures 60 and 61. It was hypothesized that greater diffusion efficiency was due to the sublimation and degradation of the methylammonium iodide precursor material in the melt chamber. One of the degradation products was methylamine, which acts as a flux to convert solid HP materials into liquid HP. Liquid HP would have greater mobility in the polymer melt and would result in the creation of spherical particles when emitted from the polymer bead on the spinneret. Spherical particles were observed throughout the melt ES fiber as EDS analysis was being conducted. Two examples can be seen in Figure 63.

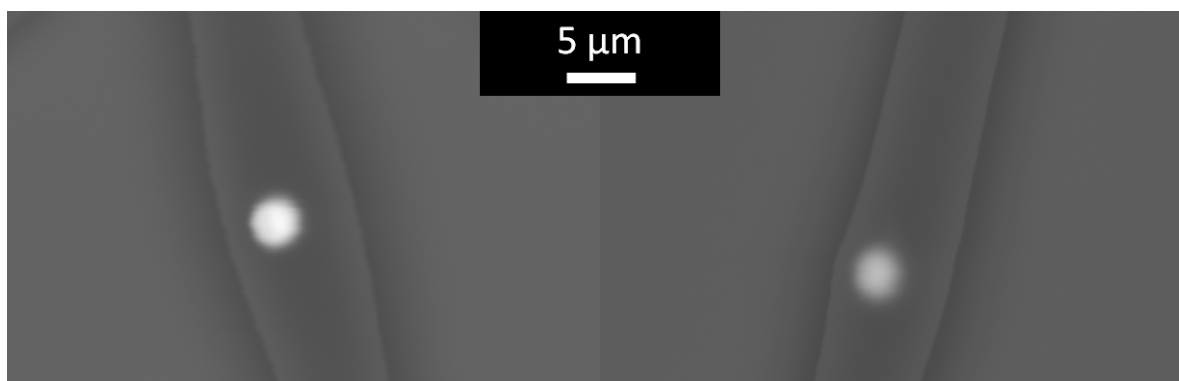


Figure 63. Spherical HP particles observed throughout electrospun fibers. The spherical shape is explained by the liquid HP material being emitted from the spinneret and solidifying *in situ*. From Murphy *et al.* [100].

The spherical HP material seen in Figure 63 is explained by the liquid HP material assuming the lowest energy shape in the polymer melt prior to removal of the methylamine gas and

solidification. There was a possibility of the spherical particles being an imaging artifact of the SEMs as a consequence of the backscattered electrons dispersing in the polymer matrix material prior to collection at the detector. In order to verify the presence of the spherical HP particles, the electrospun fiber mat was dissolved in toluene, which should solvate only the polymer and leave any remaining solids in the fiber intact. The solution was then centrifuged and washed three times with toluene to remove the PS from the solution. Solids collected were then characterized using SEM, as seen in Figure 64.

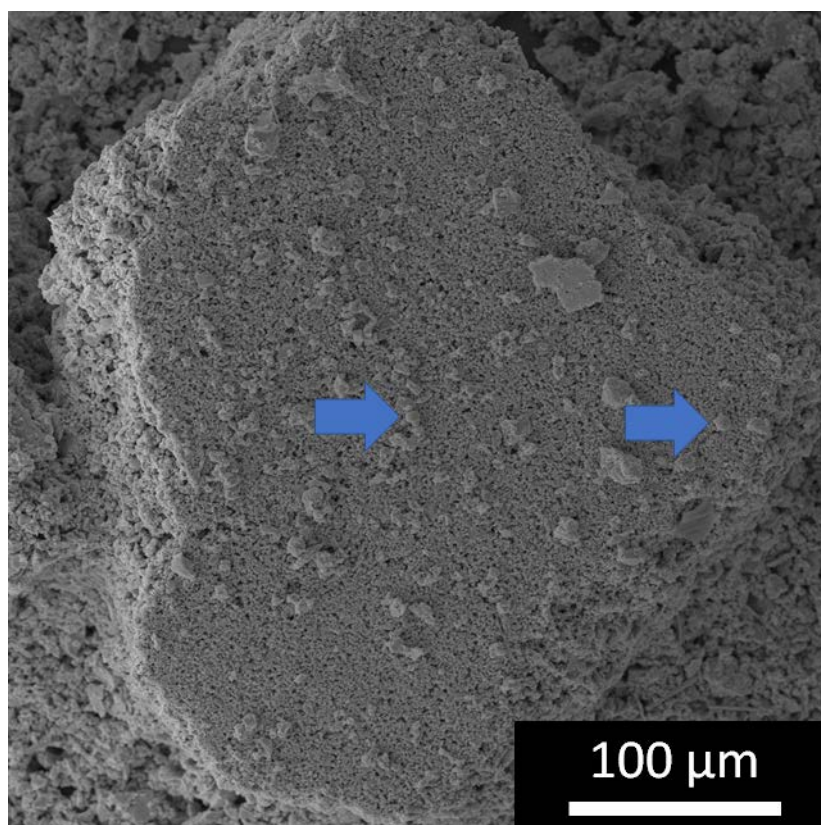


Figure 64. Electron micrograph of the solids from melt electrospun HP/polystyrene composite fibers. Arrows indicate locations of spherical HP particles.

Unfortunately, the fiber mats also contained portions of material that was not electrospun and instead simply extruded onto the collection electrode. For example, the large particle the

spherical particles are resting on was most likely extruded and not electrospun. Further verification was performed using backscattered electrons to provide elemental contrast to the electron micrographs, seen in Figure 65.

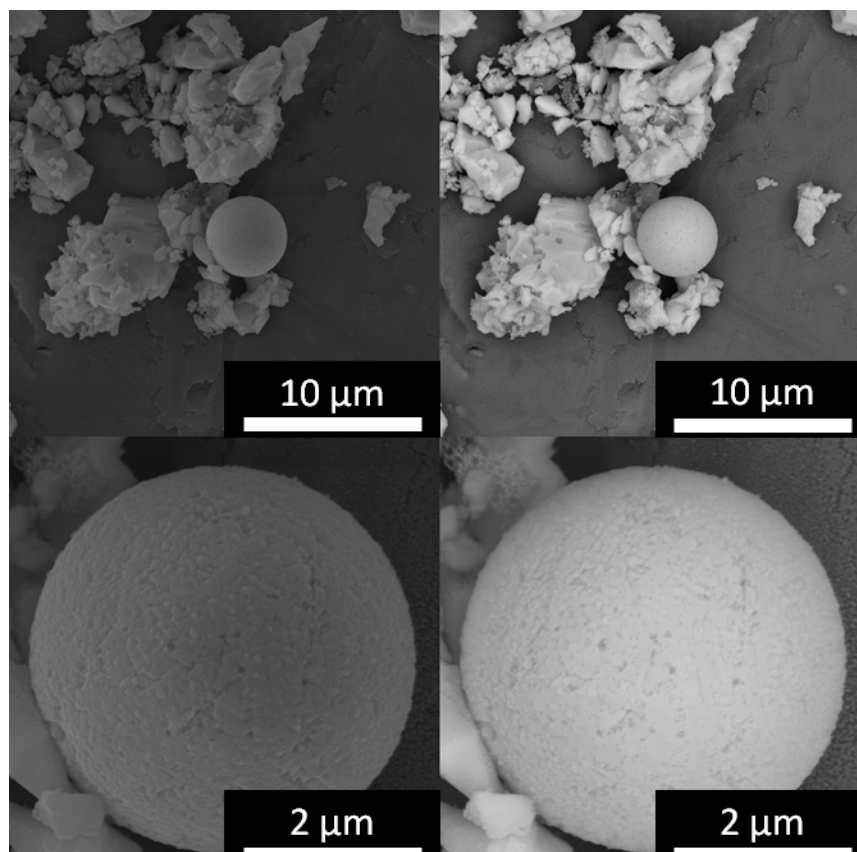


Figure 65. Electron micrographs (secondary electron on left, backscatter electron on right) show the spherical particles are composed of the same material as the other solids as verified by the elemental contrast that shows the spheres and other solids are higher Z-value elements than the aluminum substrate in the background.

Elemental contrast provided by the backscattered electron imaging elucidated the chemical character of the spherical particles, suggesting they are of the same chemical make-up as the HP solids present throughout the electron micrographs.

Melt ES of the HP/PS polymer melt was demonstrated to be successful in the creation of composite microfibers, which can be utilized to add degrees optical functionality to surfaces. Additionally, the mechanisms at work in the melt chamber were investigated and it was determined that a liquid phase of the HP material is present in the melt chamber of the electrospinner resulting in spherical particle formation. The viscosity of the polymer melt at weight loadings necessary to elicit electrical conduction prohibited the fabrication of fibers with weight loadings in excess of the percolation threshold as established previously.

4.2. Coaxial Electrospinning Encapsulated Hybrid Perovskite

Melt ES of the HP composite fibers produced unique fiber structures that were optically active and elucidated information as to the mechanisms at work in a polymer melt containing the HP precursors. However, the polymer melt could not be loaded sufficiently high to elicit electrical conduction in the microfibers due to the high viscosity of the polymer melt. In order to create fibers useful in optoelectronic devices while still providing a high degree of moisture resilience, it was decided to pursue solution coaxially electrospun fibers with a HP core and a PS sheath. The encapsulation of the HP material would occur during the electrostatic draw down process as the shell solvent evaporated, and the formation of the HP material would occur *in situ* as well due to the low thermodynamic requirements to drive the $\text{CH}_3\text{NH}_3\text{PbI}_3$ HP reaction [37].

In order to produce the coaxial fibers, it was necessary to identify solvents that were appropriate for the materials system at work in the ES process. The solution for the core needed to be a good solvent for PS and miscible with the toluene so it could mix and move through the shell for evaporation. Additionally, the solvent in the core would need to have a similar vapor pressure to that of the solvent in the shell to avoid the complete collapse of the coaxial structure of the fiber [102]. Furthermore, the solvent for the shell needed to be orthogonal, in that it was a

good solvent for the PS material but a poor solvent for the HP precursors and the HP itself. After simple mixing tests and consulting the work by Kurban *et al.*[102], it was decided that DMF would be used in the core solution to create the HP precursor solution, and toluene would be used as the solvent in the PS shell solution. After several attempts the coaxial solution ES produced fiber mats. Immediately after ES the fiber mats demonstrated a pale-yellow dun coloration; but after 5 min sitting in ambient conditions, the mats underwent a color change from the pale-yellow dun to a light brown, as seen in Figure 66.



Figure 66. An electrospun fiber mat immediately after ES (left) and after 5 min in ambient condition (right). The color change of the fiber mat is indicative of the HP reaction occurring as residual solvent evaporates in the fibers, from Murphy *et al.* [103].

The color change of the fiber mats was suggestive of the HP reaction occurring in ambient conditions shortly after fabrication of the fiber mats. The fiber mat was then subjected to UV-Vis spectroscopy to identify the presence of $\text{CH}_3\text{NH}_3\text{PbI}_3$ HP, as seen in Figure 67.

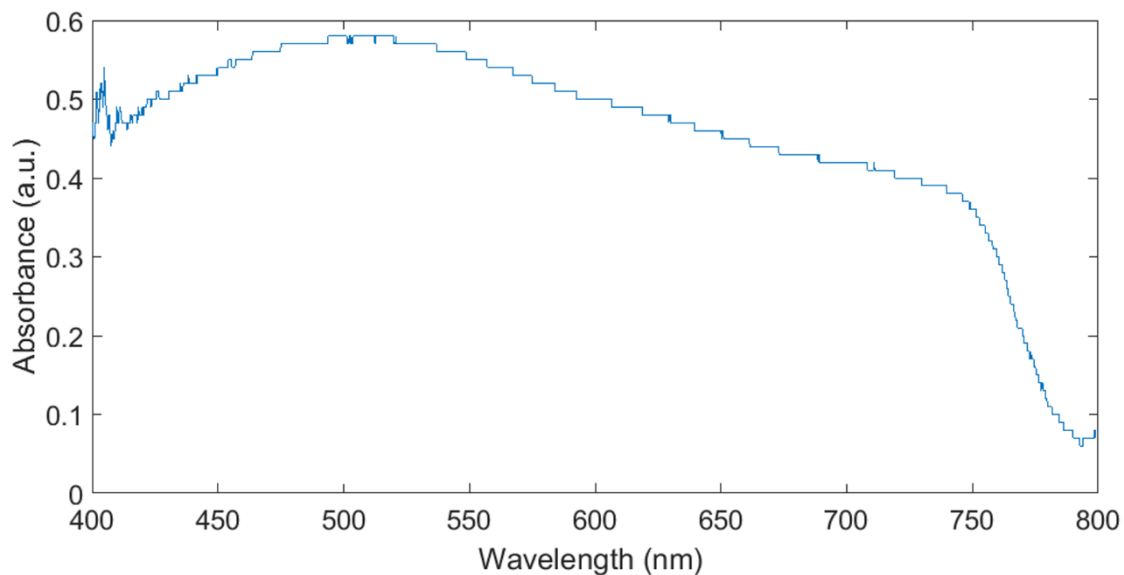


Figure 67. UV-Vis spectrum of the electrospun fiber mat seen in Figure 66. The optical absorption onset of the $\text{CH}_3\text{NH}_3\text{PbI}_3$ is visible at 760 nm as expected with very little inflection at 530 nm, indicating little to no PbI_2 is present.

The UV-Vis spectrum of the fiber mat in Figure 68 strongly indicated the presence of the $\text{CH}_3\text{NH}_3\text{PbI}_3$ HP and very little PbI_2 precursor material. To further verify the chemical fidelity of the coaxial fibers, XRD was carried out on the fiber mat, as displayed in the Figure 68. The diffractogram data demonstrated that the synthesis of the HP material *in situ* was successful in the coaxial ES process.

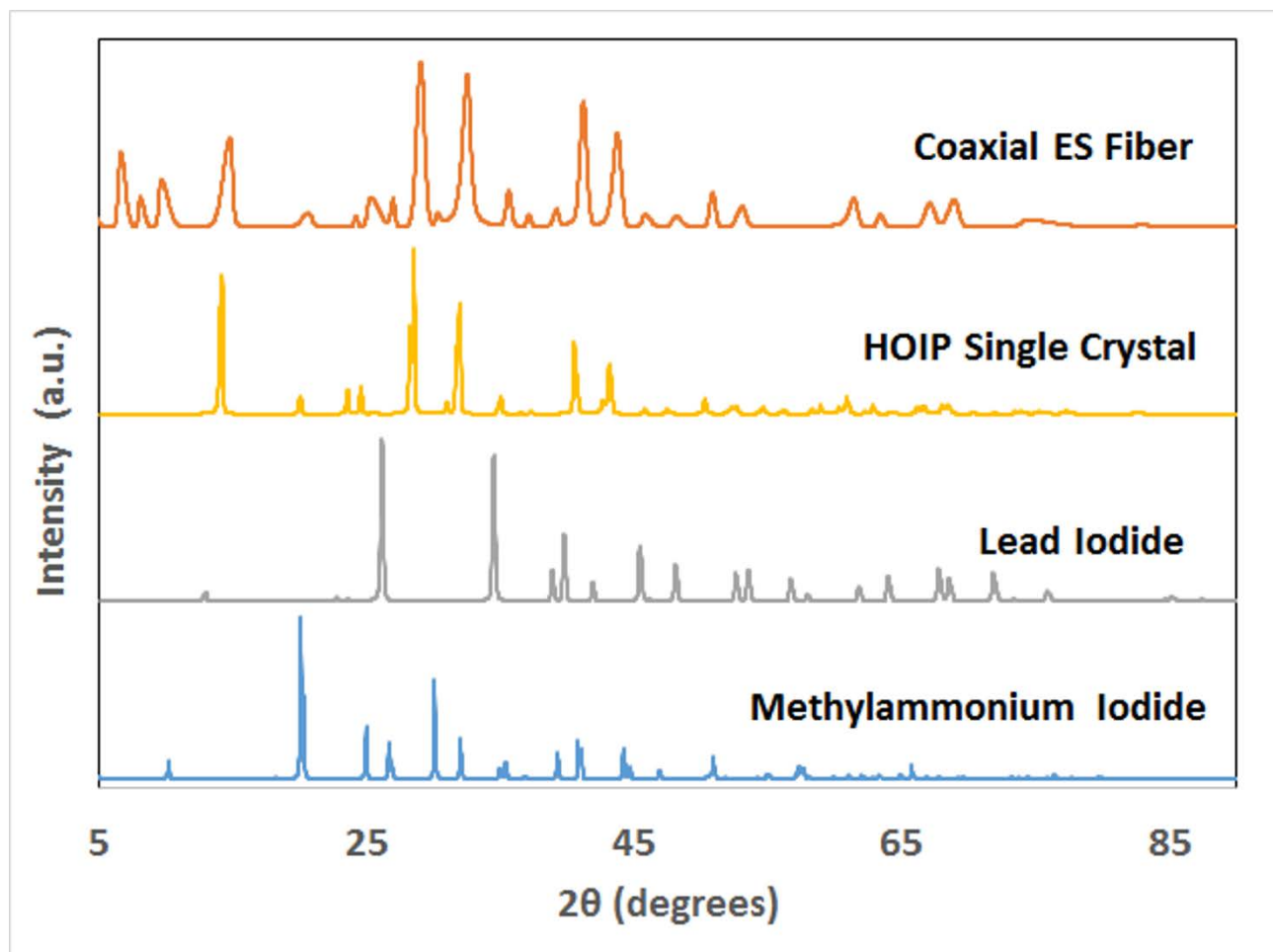


Figure 68. X-Ray diffractograms of the coaxial electrospun fibers compared to an ITC grown single crystal and the HP precursors, from Murphy *et al.* [103].

Qualitatively, very little PbI_2 was present in the coaxial fibers when comparing the peak positions.

To determine if the fiber mats were viable, optically active structures the core solution of the mat was changed to produce $\text{CH}_3\text{NH}_3\text{PbBr}_3$ HP material, which has a strong photoluminescent character and can be excited to emit light in the visible spectrum [104] for direct visualization. The $\text{CH}_3\text{NH}_3\text{PbBr}_3$ HP was also utilized to assess the continuity of the core material through the fiber mat in the same assessment using fluorescence microscopy. An optical micrograph and fluorescent optical micrograph of the same field of view can be seen in Figure 69.

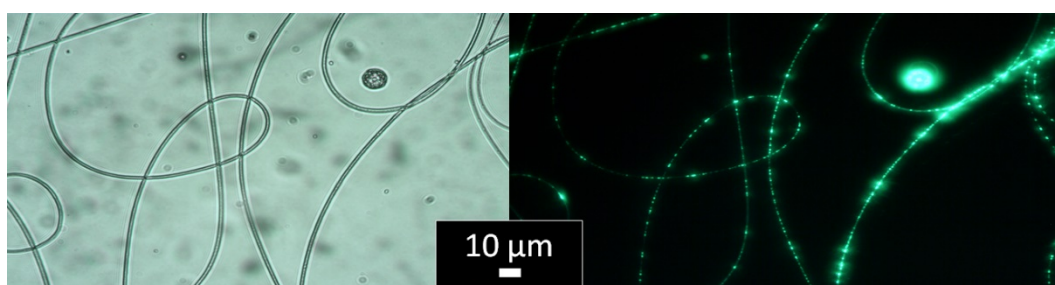


Figure 69. Optical micrograph (left) and fluorescent optical micrograph (right) of coaxial electrospun fibers with $\text{CH}_3\text{NH}_3\text{PbBr}_3$ HP material in the core of PS sheaths. The fluorescent image shows that some fibers with continuous cores were created, but most fibers demonstrate a discontinuous core, as seen in most of the fibers in the fluorescent micrograph.

The optical micrographs in Figure 69 show that the coaxial fibers produced were indeed optically active structures with a large degree in variation as to the continuity of the HP core in the fibers themselves. Fibers were then freeze fractured using liquid nitrogen to produce cross-sectional samples for interrogation using SEM. The morphology of fibers can be seen in Figure 70.

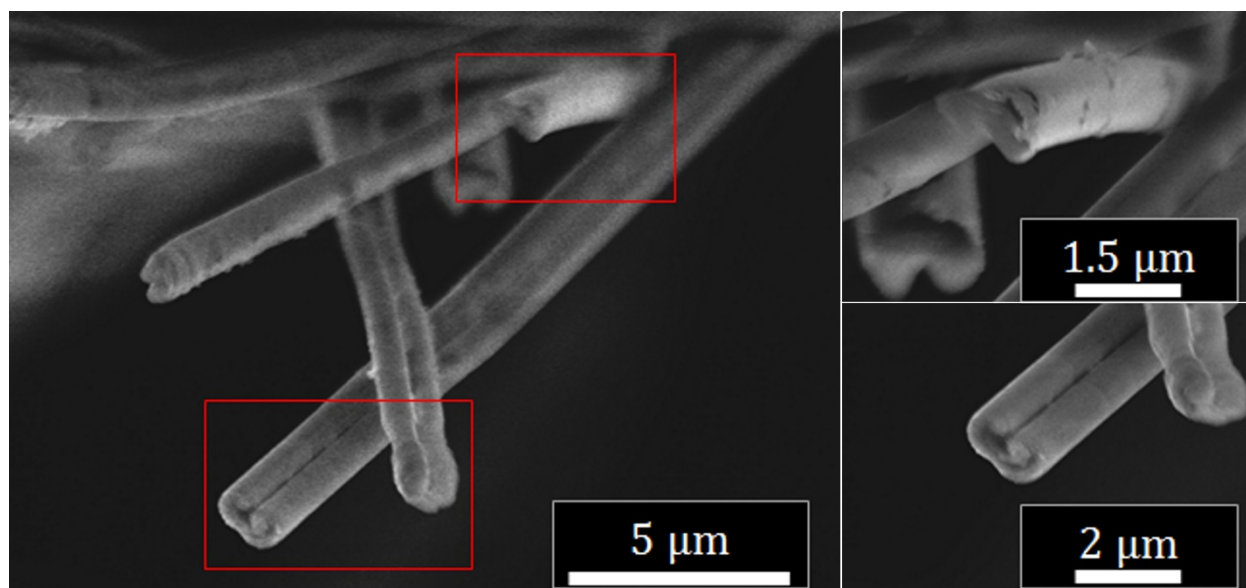


Figure 70. Electron micrographs of fiber cross-sections. Coaxial fibers demonstrated a cardioid morphology, likely the result of the shell solution evaporating at a slightly higher rate resulting in semi-solidification and collapse of the shell structure into the still liquid core, from Murphy *et al.* [103].

Electron micrographs of ES fiber cross sections reveal that instead of a purely coaxial fiber morphology the fibers demonstrate a cardioid structure. The cardioid structure is likely the result of the toluene in the shell solution evaporating at a greater rate, which would result in a semi-solidified shell structure. As the core solution continues to evaporate, the semi-solid shell would be drawn inward resulting in the collapse of the shell into the core.

Finally, the coaxial fiber mats were subjected to several tests to determine the overall resilience of the HP in the core of the cardioids. The $\text{CH}_3\text{NH}_3\text{PbBr}_3$ HP was utilized as the degradation could be directly visualized as the loss in the ability to photoluminesce as the precursor materials do not produce the characteristic green luminescence under UV excitation. Fiber mats were annealed at $80\text{ }^\circ\text{C}$ for 30 min, which is typical in most planar HP synthesis protocols. The fiber mats were also completely submerged in water for 30 min, which is normally more

than adequate to completely degrade HP materials. Result of the resilience study can be seen in Figure 71.

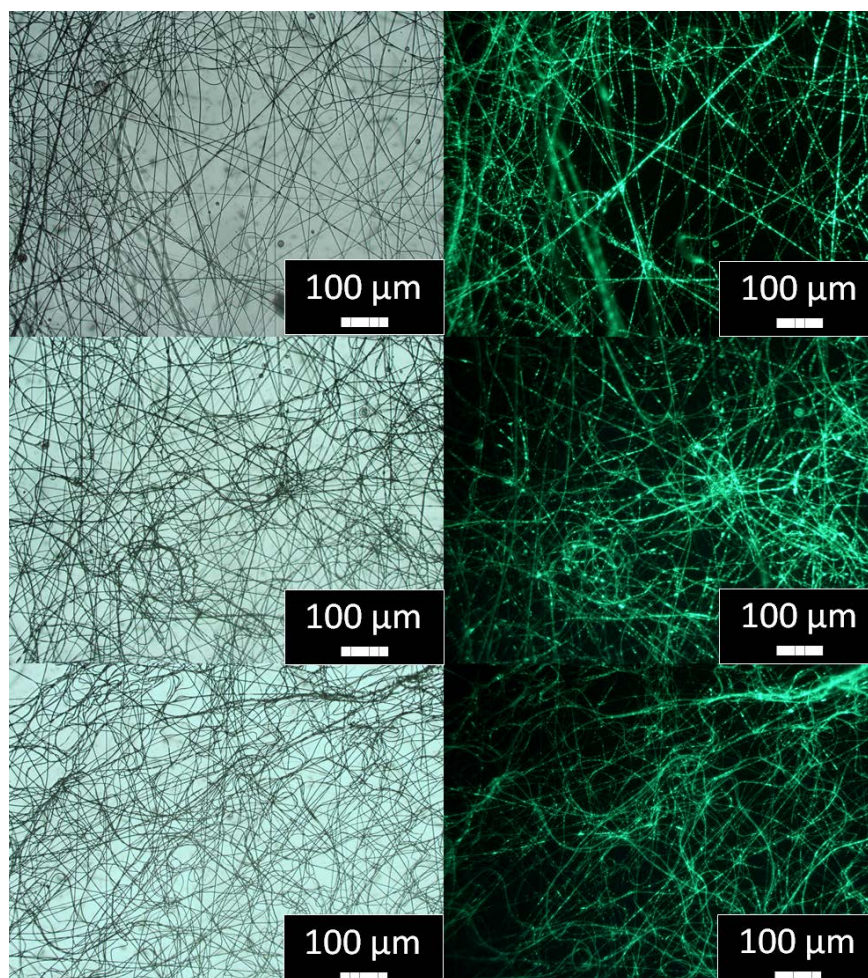


Figure 71. Optical and fluorescence micrographs of the coaxial fibers, immediately after ES (top), after a 30 min anneal at 80 °C (middle), and after 30 min of complete immersion in water (bottom). Visually no decrease in the photoluminescence was observed in any of the fiber mats. From Murphy *et al.* [103].

The most impressive result of the resilience study was the ability of the coaxial fiber mats to withstand complete immersion in water for 30 min with no visual degradation to the HP in the fibers. It was determined the reason for the ability to withstand total immersion was a hydrophobicity demonstrated by the shell of the coaxial fibers. PS fiber mats have been shown to

demonstrate a high degree of hydrophobicity, bordering on super-hydrophobicity [67]. PS itself is naturally hydrophobic and when ES PS fibers take on unique surface structuring which further enhances the hydrophobic nature of the PS fibers. A comparison of pure PS electrospun fibers and the coaxial electrospun fibers can be seen in Figure 72.

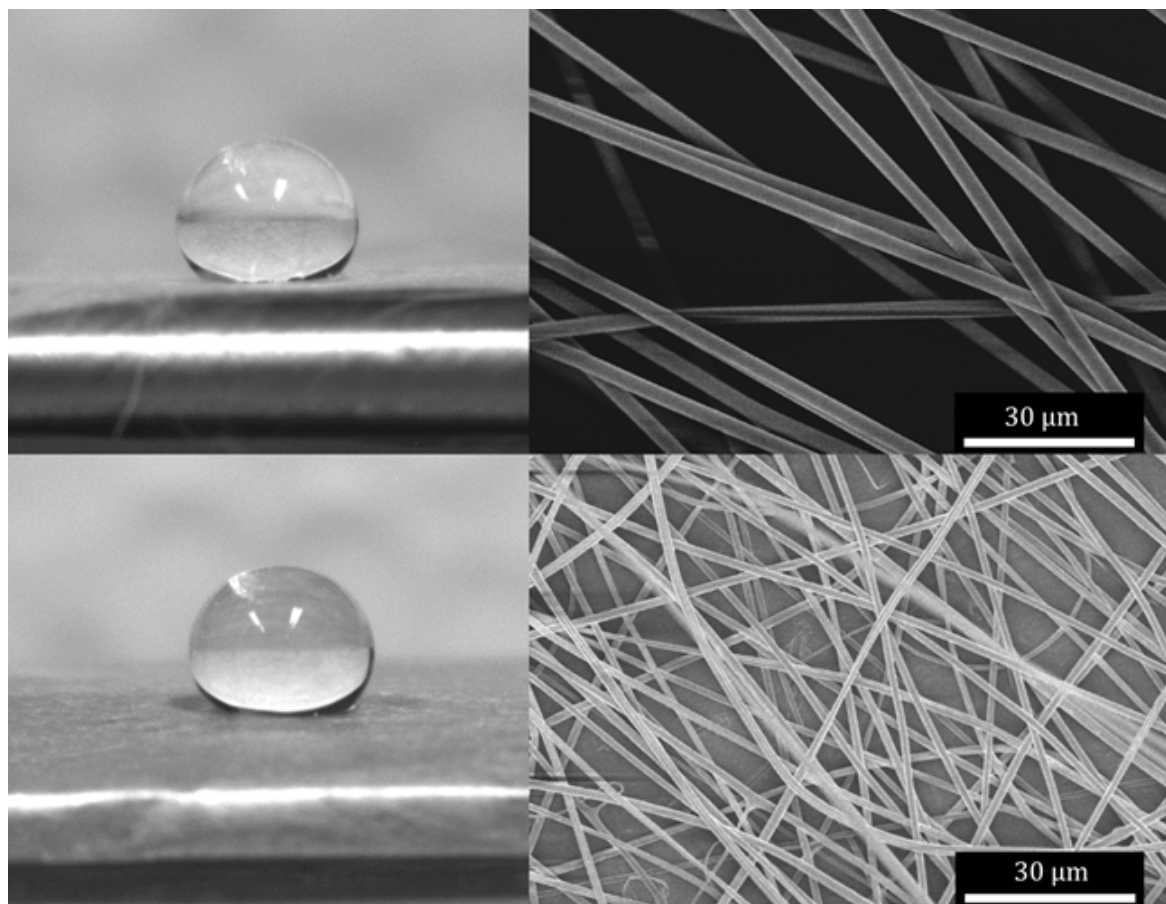


Figure 72. Optical micrographs of water droplets resting on the surface of fiber mats of neat polystyrene (top) and the coaxial fiber mats (bottom). Electron micrographs of the fiber mats show very little difference in the morphology other than fiber diameter. From Murphy *et al.* [103].

The water droplets on the surface of both the neat PS mats and the coaxial mats show that both mats demonstrate high hydrophobic behavior. Average contact angles of the water droplets for the neat PS and coaxial fiber mats were $124^{\circ} \pm 13^{\circ}$ and $117^{\circ} \pm 10^{\circ}$, respectively.

Coaxially electrospun HP core/PS shell fibers demonstrate desirable optical properties are easily applied to surfaces for optical functionalization and hold promise of incorporation into devices with a facile nature. Fibers demonstrate an unprecedented level of moisture resilience, able to withstand complete immersion in water and remain optically functional.

5. Conclusions

5.1. General Summary

In the course of the research outlined in this dissertation, a first thrust was made into the creation of an optically and electrically functional HP composite material. The resultant material demonstrated an improved moisture stability and could be loaded sufficiently to elicit electrical conduction via percolation. Composite microfibers were fabricated from the polymer melt used to create the composite material and demonstrated that HP material in the liquid state could be created from HP material formed in the polymer melt caused by the creation of degradation products also created in the polymer melt. In addition to composite fibers, coaxial fibers were also demonstrated for the first time which demonstrated remarkable moisture resistance and could potentially be utilized as localized light emitting structures.

5.2. Melt Compounding

The creation of a moisture resistant HP composite was demonstrated through a simple melt compounding process. While the method for producing the composite media was simplistic in nature, the growth mechanisms at work in the polymer melt demonstrated a unique solid-state chemistry and vapor-liquid-solid interactions. Composites created using low-cost optical polymer and without the use of solvents help to maintain a low-cost of manufacturing desirable in a next-generation photovoltaic material. The composite in this study demonstrated a high tolerance for moisture exposure experienced in an accelerated ageing study. HP/polystyrene composites generated represent the first of their kind and promoted the further study of the composite media.

5.3. Solution Compounding

Issues presented in the melt compounding of HP/polystyrene composites were thoroughly addressed in the creation of the composite via solution compounding. Extensive work was done in the pretreatment of the lead iodide precursor material in order to produce HP crystallites with a high degree of uniformity in particle size and shape. After tuning the solution chemistry involved in the creation of desirable HP filler media, the electrical properties of the composite were investigated, and the percolation threshold of HP/polystyrene composite was determined empirically to be 75 wt%. Determination of the percolation behavior of the composite was vital for the material to be eventually in a device.

5.4. Melt ES

Melt ES HP/polystyrene composite media provided a case study in driving solid-state chemical reaction in a melt electrospinner. Melt ES itself is a fairly under-utilized fabrication method, with most work focused on the generation of purely polymeric fibers with recent work focusing on the placement of fibers through direct-write fabrication techniques. The synthesis of a photoactive material as the result of a thermodynamically driven-chemical reaction *in situ* was novel enough to warrant patenting the technology. Similar to the mechanisms used in melt compounding, the mechanisms involved in the formation of HP material, as well as the reactions that take place after the formation resulting in liquid HP, elucidate unique, exploitable behavior for use in other similar systems.

5.5. Coaxial Solution ES

The coaxial ES of encapsulated HP material resulted in the creation of the optically active microfibers. Coaxial fibers demonstrated an unprecedented level of moisture resilience and a nearly continuous core. Fabrication of the coaxial fibers was shown to be amenable to other HPs,

which when paired with the tunable absorption and emission properties of the HP provide a means to generate emission layers with highly tunable chromaticity.

5.6. Recommendations for Future Work

Future work on the composite should be approached using solution compounding methods as they provide the greatest control over the filler media and result in the best dispersion in composites. If possible, the creation of a 'hybrid' filler phase where the HP material is mixed or fixed to a conductive material with a high surface area and large aspect ratio would significantly reduce the percolation threshold for conduction. Utilization of quantum confined HP nanomaterials such as quantum dots would allow composites to be heavily loaded and potential acts as optical gain media or gamma scintillation material.

In order to improve the melt ES of the composite media, the lead iodide precursor should be pretreated and loaded into the polymer feedstock prior to melt ES. The creation of a lead iodide polymer composite prior to melt ES would minimize the interruption of the melt ES process while maximizing the conversion of the precursors into HPs.

The coaxial electrospun fibers while useful in back-lit unit type optical devices must first be electrically contacted to allow for use in solar cells and electroluminescent type devices. Electrical contact of the fiber cores could be achieved through chemical means but may result in diminishing the moisture-resilience of the HP. Work must be done to develop methods to expose the core of small areas of the coaxial fibers in order to deposit charge extraction materials onto the HP material itself. However, the method is purely academic at this point and would likely require a significant amount of study to prove useful.

In order to scale up the production of the composite material, an industrial twin-screw extrusion system could be purchased and configured to output onto a roll-to-roll conductive

polymer sheet. Optimizing the concentration of the precursor materials in addition to the incorporation of a secondary filler in the composite would reduce the percolation threshold and reduce the viscosity of the polymer composite making the polymer melt more processable. To scale up the production of nanofibers produced using solution based ES a 'shower-head' type spinneret can be utilized to produce electrospun fiber mats in commercial quantities.

6. Materials Safety

6.1. Handling Organic Solvents

All organic solvents were handled while wearing gloves and safety goggles in a well-ventilated area or fume hood to prevent unnecessary exposure to fumes and/or liquid solvents.

6.2. Polymer Melt Safety

While utilizing polymer melts in the melt compounding process, several safety protocols were followed to minimize injury. Heat-resistance gloves or hot-pads were used in the direct handling of the hot crucibles or heated metal plates. Additionally, when working with the polymer melts, it is important to note that the high temperatures can often sublime or thermally degrade/off-gas from any material added to the polymer melt itself. Because of the risk of off-gassing or sublimation, it is important to work in a fume hood with adequate extraction when melt compounding.

6.3. Electrospinning Safety

The largest risk in the ES process is from the high voltages applied to components in the ES chamber. Care must be taken not to contact electrified surfaces in order to avoid electric shock. Additionally, when ES if the voltage is increased sufficiently high to cause Townsend avalanche breakdown of the air in the chamber, an arc can be created. While not directly dangerous in the equipment used, the arc has the potential to ignite flammable solvents used in the ES process; and therefore, care must be taken when ES with flammable/volatile solvents. Additionally, care must be taken when ES with potentially toxic or noxious solvents as they evaporate during the ES process into the immediate environment. Therefore, it is most often appropriate to electrospin in a well-ventilated area or in a fume-hood to prevent unnecessary exposure to potentially harmful solvents.

7. References

- [1] NREL, “Best Research-Cell Efficiencies.” [Online]. Available: <https://www.nrel.gov/pv/assets/images/efficiency-chart.png>.
- [2] U. S. E. I. Administration, “2016 Solar Photovoltaic Cell/Module Shipments Report,” Washington, D.C., 2016.
- [3] A. Kojima, K. Teshima, Y. Shirai, and T. Miyasaka, “Organometal halide perovskites as visible-light sensitizers for photovoltaic cells,” *J. Am. Chem. Soc.*, 2009.
- [4] C. Kittel, *Introduction to Solid State Physics*, 8th ed. Hoboken: John Wiley and Sons Inc, 2005.
- [5] V. Bulovic, “Excitons - Types, Energy Transfer,” 2003. [Online]. Available: <https://ocw.mit.edu/courses/electrical-engineering-and-computer-science/6-973-organic-optoelectronics-spring-2003/lecture-notes/7.pdf>. [Accessed: 15-Mar-2018].
- [6] Y. Tamai, H. Ohkita, H. Benten, and S. Ito, “Exciton diffusion in conjugated polymers: from fundamental understanding to improvement in photovoltaic conversion efficiency,” *J. Phys. Chem. Lett.*, vol. 6, no. 17, pp. 3417–3428, 2015.
- [7] H. L. Wells, “Über die Cäsium- und Kalium- Bleihalogenide,” *Zeitschrift für Anorg. und Allg. Chemie*, vol. 3, no. 1, pp. 195–210, 1893.
- [8] D. Weber, “CH₃NH₃PbX₃, ein Pb(II)-System mit kubischer Perowskitstruktur CH₃NH₃PbX₃, a Pb(II)-System with Cubic Perovskite Structure,” vol. 33, pp. 1443–1445, 1978.
- [9] H. S. Kim *et al.*, “Lead iodide perovskite sensitized all-solid-state submicron thin film mesoscopic solar cell with efficiency exceeding 9%,” *Sci. Rep.*, vol. 2, pp. 1–7, 2012.
- [10] M. M. Lee, J. Teuscher, T. Miyasaka, T. N. Murakami, and H. J. Snaith, “Efficient hybrid solar cells based on meso-superstructured organometal halide perovskites,” *Science*, vol. 338, no. 6107, pp. 643–647, 2012.
- [11] Rolf E. Hummel, “Characteristic Penetration Depth, W, and Absorbance, a,” in *Electronic Properties of Materials*, 4th ed., New York: Springer Science, 2012, p. 222.
- [12] X. Ziang *et al.*, “Refractive index and extinction coefficient of CH₃NH₃PbI₃ studied by

- spectroscopic ellipsometry,” *Opt. Mater. Express*, 2015.
- [13] P. Löper *et al.*, “Complex Refractive Index Spectra of CH₃NH₃PbI₃ Perovskite Thin Films Determined by Spectroscopic Ellipsometry and Spectrophotometry,” *J. Phys. Chem. Lett.*, vol. 6, no. 1, pp. 66–71, 2015.
- [14] M. McGehee, “Emerging High-Efficiency Low-Cost Solar Cell Technologies.” Center for Advanced Molecular Photovoltaics, Stanford, 2014.
- [15] X. Ziang *et al.*, “Refractive index and extinction coefficient of CH₃NH₃PbI₃ studied by spectroscopic ellipsometry,” *Opt. Mater. Express*, vol. 5, no. 1, p. 29, 2015.
- [16] Rolf E. Hummel, *Electronic Properties of Materials*, 4th ed. New York: Springer Science, 2012.
- [17] Q. Dong *et al.*, “Solar cells. Electron-hole diffusion lengths > 175 μm in solution-grown CH₃NH₃PbI₃ single crystals,” *Science*, vol. 347, no. 6225, pp. 967–70, 2015.
- [18] M. B. Johnston and L. M. Herz, “HPs for Photovoltaics: Charge-Carrier Recombination, Diffusion, and Radiative Efficiencies,” *Acc. Chem. Res.*, vol. 49, no. 1, pp. 146–154, 2016.
- [19] Q. Chen *et al.*, “Under the spotlight: The organic-inorganic hybrid halide perovskite for optoelectronic applications,” *Nano Today*. 2015.
- [20] W. Shockley and H. J. Queisser, “Detailed balance limit of efficiency of p-n junction solar cells,” *J. Appl. Phys.*, vol. 32, no. 3, pp. 510–519, 1961.
- [21] S. Rühle, “Tabulated values of the Shockley-Queisser limit for single junction solar cells,” *Sol. Energy*, vol. 130, pp. 139–147, 2016.
- [22] M. Quirk and J. Serda, *Semiconductor Manufacturing Technology*, 1st ed. Upper Saddle River: Prentice-Hall, 2001.
- [23] J. H. Noh, S. H. Im, J. H. Heo, T. N. Mandal, and S. Il Seok, “Chemical management for colorful, efficient, and stable inorganic-organic hybrid nanostructured solar cells,” *Nano Lett.*, 2013.
- [24] N. K. Kumawat, A. Dey, A. Kumar, S. P. Gopinathan, K. L. Narasimhan, and D. Kabra, “Band Gap Tuning of CH₃NH₃Pb(Br_{1-x}Cl_x)₃ HP for Blue Electroluminescence,” *ACS Appl. Mater.*

- Interfaces*, vol. 7, no. 24, pp. 13119–13124, 2015.
- [25] D. Zhao *et al.*, “Low-bandgap mixed tin-lead iodide perovskite absorbers with long carrier lifetimes for all-perovskite tandem solar cells,” *Nat. Energy*, vol. 2, no. 4, pp. 1–7, 2017.
- [26] M. Liu, M. B. Johnston, and H. J. Snaith, “Efficient planar heterojunction perovskite solar cells by vapour deposition,” *Nature*, 2013.
- [27] J. H. Heo *et al.*, “Efficient inorganic-organic hybrid heterojunction solar cells containing perovskite compound and polymeric hole conductors,” *Nat. Photonics*, 2013.
- [28] N. J. Jeon, J. H. Noh, Y. C. Kim, W. S. Yang, S. Ryu, and S. Il Seok, “Solvent engineering for high-performance inorganic-organic HP solar cells,” *Nat. Mater.*, 2014.
- [29] W. Nie *et al.*, “High-Efficiency Solution-Processed Perovskite Solar Cells with Millimeter-Scale Grains,” *Sci. (80-.)*, vol. 347, no. 6221, pp. 522–525, 2015.
- [30] L. Dou *et al.*, “Solution-processed HP photodetectors with high detectivity,” *Nat. Commun.*, vol. 5, pp. 1–6, 2014.
- [31] F. Li *et al.*, “Ambipolar solution-processed HP phototransistors,” *Nat. Commun.*, vol. 6, pp. 1–8, 2015.
- [32] Y. Lee *et al.*, “High-performance perovskite-graphene hybrid photodetector,” *Adv. Mater.*, vol. 27, no. 1, pp. 41–46, 2015.
- [33] Z.-K. Tan *et al.*, “Bright light-emitting diodes based on organometal halide perovskite,” *Nat. Nanotechnol.*, vol. 9, no. 9, pp. 687–692, 2014.
- [34] Y. H. Kim *et al.*, “Multicolored organic/inorganic HP light-emitting diodes,” *Adv. Mater.*, vol. 27, no. 7, pp. 1248–1254, 2015.
- [35] X. Y. Chin, D. Cortecchia, J. Yin, A. Bruno, and C. Soci, “Lead iodide perovskite light-emitting field-effect transistor,” *Nat. Commun.*, vol. 6, no. May, pp. 1–9, 2015.
- [36] Z. Yang, A. Rajagopal, and A. K. Y. Jen, “Ideal Bandgap Organic–Inorganic HP Solar Cells,” *Adv. Mater.*, vol. 29, no. 47, pp. 1–7, 2017.
- [37] Y.-Y. Zhang *et al.*, “Intrinsic Instability of the Hybrid Halide Perovskite Semiconductor CH₃NH

3 PbI₃.”

- [38] T. Leijtens, G. E. Eperon, S. Pathak, A. Abate, M. M. Lee, and H. J. Snaith, “Overcoming ultraviolet light instability of sensitized TiO₂ with meso-superstructured organometal tri-halide perovskite solar cells,” *Nat. Commun.*, vol. 4, pp. 1–8, 2013.
- [39] A. Dualeh, P. Gao, S. Il Seok, M. K. Nazeeruddin, and M. Grätzel, “Thermal behavior of methylammonium lead-trihalide perovskite photovoltaic light harvesters,” *Chem. Mater.*, 2014.
- [40] A. M. A. Leguy *et al.*, “Reversible hydration of CH₃NH₃PbI₃ in films, single crystals, and solar cells,” *Chem. Mater.*, vol. 27, no. 9, pp. 3397–3407, 2015.
- [41] E. Mosconi, J. M. Azpiroz, and F. De Angelis, “Ab Initio Molecular Dynamics Simulations of Methylammonium Lead Iodide Perovskite Degradation by Water,” *Chem. Mater.*, vol. 27, no. 13, pp. 4885–4892, 2015.
- [42] W. Ahmad, J. Khan, G. Niu, and J. Tang, “Inorganic CsPbI₃ Perovskite-Based Solar Cells: A Choice for a Tandem Device,” *Sol. RRL*, vol. 1, no. 7, p. 1700048, 2017.
- [43] S. N. Habisreutinger, T. Leijtens, G. E. Eperon, S. D. Stranks, R. J. Nicholas, and H. J. Snaith, “Enhanced hole extraction in perovskite solar cells through carbon nanotubes,” *J. Phys. Chem. Lett.*, 2014.
- [44] J. M. Deitzel, J. Kleinmeyer, D. Harris, and N. B. Tan, “The effect of processing variables on the morphology of electrospun nanofibers and textiles,” *Polymer (Guildf.)*, vol. 42, pp. 261–272, 2001.
- [45] W. K. Son, J. H. Youk, T. S. Lee, and W. H. Park, “Effect of pH on electrospinning of poly (vinyl alcohol),” *Mater. Lett.*, vol. 59, pp. 1571–1575, 2005.
- [46] J. Tao and S. Shivkumar, “Molecular weight dependent structural regimes during the electrospinning of PVA,” *Mater. Lett.*, vol. 61, pp. 2325–2328, 2007.
- [47] T. Uyar and F. Besenbacher, “Electrospinning of uniform polystyrene fibers: The effect of solvent conductivity,” *Polymer (Guildf.)*, vol. 49, pp. 5336–5343, 2008.
- [48] J. L. Skinner, J. M. Andriolo, J. P. Murphy, and B. M. Ross, “Electrospinning for nano-to

- mesoscale photonic structures,” *Nanophotonics*, vol. 6, no. 5, 2017.
- [49] MAR-BAL Inc, “History of Composite Materials,” 2018. [Online]. Available: <http://www.mar-bal.com/language/en/applications/history-of-composites/>. [Accessed: 10-Mar-2018].
- [50] L. S. Schadler, L. C. Brinson, and W. G. Sawyer, “Polymer nanocomposites: A small part of the story,” *Jom*, vol. 59, no. 3, pp. 53–60, 2007.
- [51] A. Belashi, “Percolation modeling in polymer nanocomposites,” University of Toledo, 2011.
- [52] “Percolation Threshold.” .
- [53] Alamusi, N. Hu, H. Fukunaga, S. Atobe, Y. Liu, and J. Li, “Piezoresistive strain sensors made from carbon nanotubes based polymer nanocomposites,” *Sensors*, vol. 11, no. 11, pp. 10691–10723, 2011.
- [54] Y. Wang *et al.*, “Ultrastable, Highly Luminescent Organic–Inorganic Perovskite–Polymer Composite Films,” *Adv. Mater.*, vol. 28, no. 48, pp. 10710–10717, 2016.
- [55] H. Wang, Y. Rahaq, and V. Kumar, “A composite light-harvesting layer from photoactive polymer and halide perovskite for planar heterojunction solar cells,” *Sci. Rep.*, vol. 6, no. April, pp. 1–9, 2016.
- [56] S. Chen, C. Teng, M. Zhang, Y. Li, D. Xie, and G. Shi, “A Flexible UV–Vis–NIR Photodetector based on a Perovskite/Conjugated-Polymer Composite,” *Adv. Mater.*, pp. 5969–5974, 2016.
- [57] J. Lu, L. Zhang, C. Peng, L. Rao, and M. Wan, “Preparation and Characterization of $\text{CH}_3\text{NH}_3\text{PbI}_3$ Perovskite Deposited onto Polyacrylonitrile (PAN) Nanofiber Substrates,” *Chem. Lett.*, vol. 45, no. 3, pp. 312–314, 2016.
- [58] D. Chen and Y. Zhu, “Electrospun Perovskite Nanofibers,” *Nanoscale Res. Lett.*, vol. 12, no. 1, pp. 12–16, 2017.
- [59] J. E. Mark, *Polymer Data Handbook*, 1st ed. Oxford University Press, 1999.
- [60] J. P. Murphy, J. M. Andriolo, B. M. Ross, G. F. Wyss, N. E. Zander, and J. L. Skinner, “Organometallic Halide Perovskite Synthesis in Polymer Melt for Improved Stability in High Humidity,” in *MRS Advances*, 2016, vol. 1, no. 47.

- [61] A. P. Wilkinson, "Solid State Synthesis Methods," 2001.
- [62] J. Yang, B. D. Siempelkamp, D. Liu, and T. L. Kelly, "Investigation of CH₃NH₃PbI₃ degradation rates and mechanisms in controlled humidity environments using in situ techniques," *ACS Nano*, 2015.
- [63] D. S. AHLAWAT, "STUDY OF BAND GAP ENERGY AND THERMAL PROPERTIES OF PbI_2 BY PHOTOACOUSTIC SPECTROSCOPY," *Mod. Phys. Lett. B*, vol. 26, no. 16, p. 1250098, 2012.
- [64] Z. Zhou *et al.*, "Methylamine-Gas-Induced Defect-Healing Behavior of CH₃NH₃PbI₃ Thin Films for Perovskite Solar Cells," *Angew. Chemie Int. Ed.*, vol. 54, no. 33, pp. 9705–9709, 2015.
- [65] B. Conings *et al.*, "Structure-Property Relations of Methylamine Vapor Treated HP CH₃NH₃PbI₃ Films and Solar Cells," *ACS Appl. Mater. Interfaces*, vol. 9, no. 9, pp. 8092–8099, 2017.
- [66] T. Zhao *et al.*, "Design rules for the broad application of fast ($\leq 1\text{ s}$) methylamine vapor based, HP post deposition treatments," *RSC Adv.*, vol. 6, no. 33, pp. 27475–27484, 2016.
- [67] M. Kang, R. Jung, H. S. Kim, and H. J. Jin, "Preparation of superhydrophobic polystyrene membranes by electrospinning," *Colloids Surfaces A Physicochem. Eng. Asp.*, vol. 313–314, pp. 411–414, 2008.
- [68] R. K. Wang, H. R. Liu, and F. W. Wang, "Facile preparation of raspberry-like superhydrophobic polystyrene particles via seeded dispersion polymerization," *Langmuir*, vol. 29, no. 36, pp. 11440–11448, 2013.
- [69] R. Patiño-Herrera, R. Catarino-Centeno, G. González-Alatorre, A. Gama Goicochea, and E. Pérez, "Enhancement of the hydrophobicity of recycled polystyrene films using a spin coating unit," *J. Appl. Polym. Sci.*, vol. 134, no. 40, pp. 1–14, 2017.
- [70] S. Yang, S. Chen, Y. Tian, C. Feng, and L. Chen, "Facile Transformation of a Native Polystyrene (PS) Film into a Stable Superhydrophobic Surface via Sol – Gel Process Wettability of surfaces with liquids is a very important property of materials that is governed by both the chemical

- composition and the,” no. 18, pp. 1233–1235, 2008.
- [71] N. Sultanova, S. Kasarova, and I. Nikolov, “Dispersion properties of optical polymers,” *Acta Phys. Pol. A*, vol. 116, no. 4, pp. 585–587, 2009.
- [72] J. H. Noh, S. H. Im, J. H. Heo, T. N. Mandal, and S. Il Seok, “Chemical Management for Colorful, Efficient, and Stable Inorganic – Organic Hybrid Nanostructured Solar Cells,” *Nano Lett.*, vol. 13, pp. 1764–1769, 2013.
- [73] X. Jing, W. Zhao, and L. Lan, “The effect of particle size on electric conducting percolation threshold in polymer/conducting particle composites,” *J. Mater. Sci. Lett.*, vol. 19, pp. 377–379, 2000.
- [74] D. He and N. N. Ekere, “Effect of particle size ratio on the conducting percolation threshold of granular conductive-insulating composites,” *J. Phys. D. Appl. Phys.*, vol. 37, no. 13, pp. 1848–1852, 2004.
- [75] Y. Kesari and A. Athawale, “Ultrasound assisted bulk synthesis of CH₃NH₃PbI₃ perovskite at room temperature,” *Mater. Lett.*, 2015.
- [76] Y. Tong *et al.*, “Highly Luminescent Cesium Lead Halide Perovskite Nanocrystals with Tunable Composition and Thickness by Ultrasonication,” *Angew. Chemie - Int. Ed.*, vol. 55, no. 44, pp. 13887–13892, 2016.
- [77] V. Bhooshan Kumar, L. Gouda, Z. Porat, and A. Gedanken, “Sonochemical synthesis of CH₃NH₃PbI₃ perovskite ultrafine nanocrystal sensitizers for solar energy applications,” *Ultrason. Sonochem.*, vol. 32, pp. 54–59, 2016.
- [78] M. B. Johansson *et al.*, “From Quantum Dots to Micro Crystals: Organolead Triiodide Perovskite Crystal Growth from Isopropanol Solution,” *ECS J. Solid State Sci. Technol.*, vol. 5, no. 10, pp. P614–P620, 2016.
- [79] P. J. Kumar *et al.*, “A novel low-temperature solid-state route for nanostructured cubic garnet Li₇La₃Zr₂O₁₂ and its application to Li-ion battery,” *RSC Adv.*, vol. 6, no. 67, pp. 62656–62667, 2016.

- [80] hielscher, "Ultrasonic Wet-Milling and Micro-Grinding," 2018. .
- [81] R. Ge, Z. Liu, H. Chen, D. Zhang, and T. Zhao, "Wet-milling effect on the properties of ultrafine yttria-stabilized zirconia powders," *Ceram. Int.*, vol. 22, no. 2, pp. 123–130, 1996.
- [82] J. P. Murphy, J. M. Andriolo, N. J. Sutton, G. Wyss, and J. L. Skinner, "Loading Dependent Electrical Properties of HP Composite Media," 2017.
- [83] T. Sugimoto, "General kinetics of Ostwald ripening of precipitates," *J. Colloid Interface Sci.*, vol. 63, no. 1, pp. 16–26, 1978.
- [84] †,‡ Hong Zhao, †,‡ Jie-Xin Wang, ‡ Qi-An Wang, *,†,‡ and Jian-Feng Chen, and J. Yun§, "Controlled Liquid Antisolvent Precipitation of Hydrophobic Pharmaceutical Nanoparticles in a Microchannel Reactor," pp. 8229–8235, 2007.
- [85] M. E. Matteucci, M. A. Hotze, K. P. Johnston, and R. O. Williams, "Drug nanoparticles by antisolvent precipitation: Mixing energy versus surfactant stabilization," *Langmuir*, vol. 22, no. 21, pp. 8951–8959, 2006.
- [86] A. A. Lonare and S. R. Patel, "Antisolvent Crystallization of Poorly Water Soluble Drugs," *Int. J. Chem. Eng. Appl.*, vol. 4, no. 5, pp. 337–341, 2013.
- [87] W. Genck, "Make the most of antisolvent crystallization," *Chemical Processing*, 2010. [Online]. Available: <https://www.chemicalprocessing.com/articles/2010/210/>. [Accessed: 10-Mar-2018].
- [88] Y. Wu *et al.*, "Retarding the crystallization of PbI_2 for highly reproducible planar-structured perovskite solar cells via sequential deposition," *Energy Environ. Sci.*, vol. 7, no. 9, pp. 2934–2938, 2014.
- [89] Wavefunction Inc, "Spartan." Wavefunction Inc. & Q-Chem, 1991.
- [90] N. Al-Salim, A. G. Young, R. D. Tilley, A. J. McQuillan, and J. Xia, "Synthesis of CdSeS nanocrystals in coordinating and noncoordinating solvents: Solvent's role in evolution of the optical and structural properties," *Chem. Mater.*, vol. 19, no. 21, pp. 5185–5193, 2007.
- [91] F. Zhang *et al.*, "Colloidal Synthesis of Air-Stable $\text{CH}_3\text{NH}_3\text{PbI}_3$ Quantum Dots by Gaining Chemical Insight into the Solvent Effects," *Chem. Mater.*, vol. 29, no. 8, pp. 3793–3799, 2017.

- [92] S. T. Ha, X. Liu, Q. Zhang, D. Giovanni, T. C. Sum, and Q. Xiong, "Synthesis of Organic-Inorganic Lead Halide Perovskite Nanoplatelets: Towards High-Performance Perovskite Solar Cells and Optoelectronic Devices," *Adv. Opt. Mater.*, 2014.
- [93] S.-T. Ha, R. Su, J. Xing, Q. Zhang, and Q. Xiong, "Metal halide perovskite nanomaterials: synthesis and applications," *Chem. Sci.*, vol. 8, no. 4, pp. 2522–2536, 2017.
- [94] R. Naphade, S. Nagane, U. Bansode, M. Tathavadekar, A. Sadhanala, and S. Ogale, "Synthetic Manipulation of HP Systems in Search of New and Enhanced Functionalities," *ChemSusChem*, vol. 10, no. 19, pp. 3722–3739, 2017.
- [95] S. A. Speakman, "Estimating Crystallite Size Using XRD," Boston.
- [96] P. H. Coelho and A. R. Morales, "Electrical conductivity, percolation threshold and dispersion properties of PMMA nanocomposites of hybrid conducting fillers," *14th IEEE Int. Conf. Nanotechnology, IEEE-NANO 2014*, pp. 706–710, 2014.
- [97] J. Li, P. C. Ma, W. S. Chow, C. K. To, B. Z. Tang, and J. K. Kim, "Correlations between percolation threshold, dispersion state, and aspect ratio of carbon nanotubes," *Adv. Funct. Mater.*, vol. 17, no. 16, pp. 3207–3215, 2007.
- [98] M. Zulkarnain, A. B. Muhamad Husaini, M. Mariatti, and I. A. Azid, "Particle Dispersion Model for Predicting the Percolation Threshold of Nano-Silver Composite," *Arab. J. Sci. Eng.*, pp. 1–14, 2015.
- [99] A. Pisoni *et al.*, "Ultra-low thermal conductivity in organic-inorganic HP CH₃NH₃PbI₃," *J. Phys. Chem. Lett.*, 2014.
- [100] J. P. Murphy, B. M. Ross, J. M. Andriolo, and J. L. Skinner, "Hybrid organic–inorganic perovskite composite fibers produced via melt electrospinning," *J. Vac. Sci. Technol. B, Nanotechnol. Microelectron. Mater. Process. Meas. Phenom.*, 2016.
- [101] T. Oku, *Solar Cells-New Approaches and Reviews*. Rijeka: Intech, 2015.

- [102] Z. Kurban *et al.*, “A solution selection model for coaxial electrospinning and its application to nanostructured hydrogen storage materials,” *J. Phys. Chem. C*, vol. 114, no. 49, pp. 21201–21213, 2010.
- [103] J. P. Murphy, J. M. Andriolo, N. J. Sutton, M. C. Brockway, and J. L. Skinner, “Coaxial HP fibers: Synthesis and encapsulation *in situ* via electrospinning,” *J. Vac. Sci. Technol. B, Nanotechnol. Microelectron. Mater. Process. Meas. Phenom.*, 2017.
- [104] M. S. Alias *et al.*, “Optical constants of CH₃NH₃PbBr₃ perovskite thin films measured by spectroscopic ellipsometry,” *Opt. Express*, vol. 24, no. 15, p. 16586, 2016.